

**Reactive control of velocity fluctuations using an active deformable surface and  
real-time PIV**

by

Findlay Stuart McCormick

A thesis submitted in partial fulfillment of the requirements for the degree of

Master of Science

Department of Mechanical Engineering  
University of Alberta

©Findlay Stuart McCormick, 2023

# Abstract

This work investigated the use of an active deformable surface and real-time particle image velocimetry (RT-PIV) for reactive control of periodic vortex shedding from a wall-mounted spherical cap immersed in a laminar boundary layer. The reactive control strategies involved locally targeting wall-normal ( $v$ ) or streamwise ( $u$ ) velocity fluctuations with velocity fluctuations induced by wall-normal surface deformations that comply with or oppose the measured velocity fluctuations. These strategies were inspired by similar ones that were numerically investigated by Choi et al. (1994). Our investigation found that the reactive control strategies generally inhibited the penetration of sweep motions towards the wall. Among the investigated strategies, those employing opposing  $v$ -control and compliant  $u$ -control demonstrated the greatest inhibition of sweep motions. As well, the reactive control strategies caused significant disruption of the periodic vortex shedding process with the extent of disruption being related to the amplitude of actuations. The greatest disruption was achieved by  $v$ -control applying opposing actuations. The opposing  $v$ -control cases applying the strongest actuations reduced the energy of two POD modes associated with vortex shedding by up to 69% relative to the unforced flow. For many of the cases that showed the greatest disruption of the periodic flow, the turbulent kinetic energy (TKE) of the flow was also increased relative to the unforced flow. Opposing actuation cases of  $v$ -control and compliant actuation cases of  $u$ -control exhibited the lowest TKE values on average. Consequently, these cases of reactive control proved to be the most effective at decreasing the energy of the vortex shedding process with minimal additional energy introduced in the form of other flow motions.

# Preface

This thesis is an original work by Findlay McCormick completed with guidance from Dr. Sina Ghaemi and Dr. Bradley Gibeau.

The results from chapter 4 of this thesis are currently in preparation for submission as a journal article.

*Dedicated to my parents.*

# Acknowledgements

First I would like to express my gratitude to Dr. Sina Ghaemi for the numerous hours he committed to mentoring and supporting me throughout my program. Your guidance has been exceptional and was vital to overcoming many of the challenges I encountered.

Second, thank you to Rick Conrad and the staff of the mechanical engineering machine shop. My research could not have been conducted without your expertise and help in realizing the physical apparatuses I utilized in my experiments.

Third, thank you to my friends and family for your celebration of my successes and support through challenging times. This contributed immensely to my motivation and enjoyment of this program.

Lastly, I would like to thank the Natural Science and Engineering Research Council of Canada (NSERC) for the Alexander Graham Bell Graduate Scholarship. This funding allowed more of my focus and effort to be applied purely toward my research.

# Contents

<b>Abstract</b>	<b>ii</b>
<b>Preface</b>	<b>iii</b>
<b>Dedication</b>	<b>iv</b>
<b>Acknowledgements</b>	<b>v</b>
<b>Contents</b>	<b>vi</b>
<b>List of Figures</b>	<b>viii</b>
<b>1 Introduction</b>	<b>1</b>
1.1 Motivation . . . . .	1
1.2 Objectives . . . . .	2
1.3 Thesis overview . . . . .	3
<b>2 Background</b>	<b>4</b>
2.1 Turbulent boundary layer flows . . . . .	4
2.1.1 Coherent structures . . . . .	6
2.2 Active control of turbulent wall-bounded flows . . . . .	10
2.2.1 Reactive control . . . . .	11
2.2.2 Actuation using motion and deformation of the wall . . . . .	15
2.3 Particle image velocimetry . . . . .	16
2.3.1 Principles of PIV . . . . .	17
2.3.2 RT-PIV . . . . .	20
2.3.2.1 Latency . . . . .	21
2.3.2.2 Algorithm optimization . . . . .	23
2.3.2.3 Hardware optimization . . . . .	25

<b>3</b>	<b>Experimental Methodology</b>	<b>27</b>
3.1	Flow setup . . . . .	27
3.2	Active deformable surface . . . . .	30
3.3	Offline PIV . . . . .	33
3.4	RT-PIV . . . . .	35
3.5	Reactive control . . . . .	40
3.5.1	Control based on wall-normal velocity ( $v$ -control) . . . . .	41
3.5.2	Control based on streamwise velocity ( $u$ -control) . . . . .	43
<b>4</b>	<b>Results</b>	<b>45</b>
4.1	Actuation and flow energy . . . . .	45
4.2	Instantaneous flow fields . . . . .	48
4.2.1	Unforced flow . . . . .	49
4.2.2	Impacts of reactive control . . . . .	50
4.3	Time-averaged flow fields . . . . .	52
4.3.1	Unforced flow . . . . .	52
4.3.2	Impacts of reactive control and varied gain . . . . .	54
4.3.3	Impacts of sensor location . . . . .	63
4.4	Suppression of vortex shedding . . . . .	67
<b>5</b>	<b>Conclusions</b>	<b>72</b>
5.1	Summary of results . . . . .	72
5.2	Future work . . . . .	76
	<b>Bibliography</b>	<b>78</b>
	<b>Appendices</b>	<b>82</b>
A	Technical drawings of experimental apparatuses . . . . .	82
B	Simulink Real-time models . . . . .	106

# List of Figures

2.1	Schematic of coherent structures in a turbulent boundary layer . . . . .	8
2.2	Schematic of a planar PIV imaging system . . . . .	18
2.3	PIV timing diagram . . . . .	19
2.4	PIV algorithm visualization . . . . .	19
2.5	RT-PIV timing diagram . . . . .	22
3.1	Schematic of flat plate apparatus for reactive control experimentation . . . . .	29
3.2	Boundary layer profile of the flat plate apparatus in the absence of the spherical cap	29
3.3	Schematic and photograph of active surface assembly . . . . .	31
3.4	Schematic illustrating relation of servo arm rotation to actuator foot displacement .	32
3.5	Schematic and photograph of the active surface approximating a sine wave . . . . .	32
3.6	Timeseries comparison of a single actuator's tracking of a sample control signal . . .	33
3.7	Photograph of the offline PIV system . . . . .	34
3.8	Photograph of RT-PIV and offline PIV cameras on either side of water flume . . . .	36
3.9	PIV algorithm implemented in RT-PIV system . . . . .	37
3.10	Spatial comparison of velocity fields measured by RT-PIV and offline PIV systems .	38
3.11	Timeseries of velocity measurements from the offline PIV and RT-PIV systems . . .	38
3.12	Schematic of the active surface relative to RT-PIV FOV . . . . .	40
3.13	Block diagram summarizing steps of the $v$ -control algorithm . . . . .	41
3.14	Sample timeseries demonstrating steps involved in $v$ -control algorithm . . . . .	42
3.15	Block diagram summarizing steps of the $u$ -control algorithm . . . . .	43
3.16	Sample timeseries demonstrating steps involved in $u$ -control algorithm . . . . .	44
4.1	Active surface standard deviation displacement during reactive control . . . . .	46
4.2	Turbulent kinetic energy of flow during reactive control . . . . .	48
4.3	Instantaneous streamwise and wall-normal velocity contours of the unforced flow . .	50
4.4	Instantaneous streamwise and wall-normal velocity contours during $v$ -control . . . .	51
4.5	Instantaneous streamwise and wall-normal velocity contours during $u$ -control . . . .	52
4.6	Average streamwise velocity, wall-normal velocity, and Reynolds shear stress con- tours of the unforced flow . . . . .	54

4.7	Relative average streamwise velocity contours for reactive control at all tested gain values . . . . .	55
4.8	Relative average wall-normal velocity contours for reactive control at all tested gain values . . . . .	59
4.9	Relative Reynolds shear stress contours for reactive control cases at all tested gain values . . . . .	62
4.10	Relative average streamwise velocity contours for reactive control cases with a gain of $-1$ and at the six tested sensor locations. . . . .	65
4.11	Relative average streamwise velocity contours for reactive control cases with a gain of $1$ and at the six tested sensor locations. . . . .	66
4.12	Energies of first six POD modes for $v$ -control and $u$ -control with $(\Delta x_s, y_s)/h = (-0.9, 1.1)$ . . . . .	69
4.13	Sum of energy of first two POD modes for $v$ -control and $u$ -control cases . . . . .	70

# Chapter 1

## Introduction

### 1.1 Motivation

The control of fluid flows is fundamental to innumerable industrial and technological systems. It is noted by Gad-el Hak (2000) that examples of flow control date back to extremely early in human history in technologies such as aerodynamic spears, fin stabilized arrows, and complex irrigation systems. These ancient examples and, in fact, many modern examples of flow control might best be described as passive control as they rely on fixed geometries to achieve the desired flow control function. Passive flow control has enabled the development of a variety of incredible and effective technologies; however, it has the significant downside of not being able to adapt to changing flow conditions. As such, passive control strategies may perform sub-optimally and even inhibit proper function in flow conditions outside of some designed range. Over the past several decades, there has been growing recognition of the potential for active flow control (AFC) strategies to address this shortcoming of passive flow control and to generally outperform passive strategies in a variety of scenarios (Gad-el Hak, 2000; Brunton and Noack, 2015; Duriez et al., 2017). AFC refers to the use of actuators and sensors to actively force flows in a desirable manner based on real-time knowledge of flow conditions. Much of the growing interest in AFC in recent decades has been driven by the rapidly improving function and decreasing expense of actuators, sensors, and computing technologies. This has made experimental investigation of AFC an increasingly viable pursuit for researchers.

Among the numerous potential applications of AFC, this thesis is particularly concerned with

the active control of turbulent boundary layers. This topic is of significant interest due to the prevalence of turbulent boundary layers in technologies related to transportation, energy, and various other industries. A major detrimental effect of turbulent boundary layers in many technologies where they occur is the large amount of skin friction drag that they cause (Schlichting and Gersten, 2017). As such, much of the work on active control of turbulent boundary layers is concerned with reducing drag. Successfully developing effective AFC strategies for reducing the drag induced by turbulent boundary layers could allow for efficiency improvements for a great number of existing technologies.

## 1.2 Objectives

Despite its great potential, the development of AFC strategies for turbulent boundary layers is still in its early stages. This is especially true for experimental investigations of this topic. Consequently, the goal of this thesis is to expand current knowledge regarding active control strategies relevant to the control of turbulent boundary layers and to demonstrate tools for the experimental implementation and investigation of these strategies. The objectives of this thesis are as follows:

- Development of an active deformable surface using an array of actuators placed in a stream-wise arrangement. Each actuator is controlled independently allowing the surface to generate complex on-demand surface deformations.
- Development of an RT-PIV system for fast non-intrusive sensing of velocity fluctuations above the actuators.
- Experimental implementation of two reactive control strategies similar to those numerically investigated by Choi et al. (1994) for reducing drag in turbulent boundary layers.
- Evaluation of the effects of the reactive control schemes applying compliant and opposing actuations of several amplitudes, as well as using different sensor locations to characterize the effects of streamwise and wall-normal distance between measured fluid motions and actuations.

The reactive control for the current investigation was applied to a periodic flow downstream of a wall-mounted spherical cap immersed in a laminar boundary layer. The coherence and periodicity of the structures in this flow were desirable for this initial investigation as it was hypothesized this would allow for clearer observation of the effects and underlying mechanisms of the reactive control. This investigation represents an initial step towards the control of more complex flows.

### 1.3 Thesis overview

**Chapter 2** of this thesis provides reviews of topics relevant to understanding the later methodology and results chapters of this work. The topics reviewed include turbulent boundary layers and the coherent structures found within turbulent boundary layers. As well, flow control strategies and actuation methods relevant to wall-bounded flows are outlined. Lastly, reviews of particle image velocimetry and the efforts to implement this measurement technique in real-time are provided.

**Chapter 3** describes the experimental methodology employed in the experiments conducted for the current investigation. This includes descriptions of the flow facility, the actuation system, real-time and offline measurement systems, and the control strategies that were implemented.

**Chapter 4** outlines the results of the experimental investigations of reactive control conducted for this thesis. This includes discussion of actuation amplitudes and the relation of this to the turbulent kinetic energy flow. As well, observations from the instantaneous and time-averaged flow fields are outlined. Lastly, a discussion of the suppression of vortex shedding as a result of the applied reactive control is provided.

Lastly, **chapter 5** provides a summary of the overall thesis and clearly outlines its key results and conclusions. This chapter concludes with suggestions for future work that may build upon the work outlined in this thesis.

## Chapter 2

# Background

### 2.1 Turbulent boundary layer flows

Boundary layer flows can be found throughout numerous technologies and industries and in a variety of forms due to differing velocities, pressure and temperature gradients, and surface characteristics. These flows are characterized by a “no-slip” boundary condition at the interface between the solid surface and the fluid medium of a flow. The no-slip condition results in a velocity profile where fluid velocity grows from zero at the wall toward the freestream velocity of the flow as you move further from the wall. This thesis is primarily concerned with turbulent boundary layer flows over flat and smooth surfaces. Developing our understandings of these idealized flows is fundamental to understanding a variety of more complex flows. Consequently, this class of boundary layer flow has been the focus of a large amount of investigation. The review provided here will cover only a very small portion of the immense body of literature on these flows with a primary focus on coherent structures in turbulent boundary layers. For a more detailed review of boundary layer flows, readers are directed to Schlichting and Gersten (2017).

Boundary layer flows are often characterized by their Reynolds number ( $Re$ ),

$$Re = \frac{\rho U_{\infty} L}{\mu} \quad (2.1)$$

where  $\rho$  is the density of the flow medium,  $U_{\infty}$  is the freestream velocity,  $L$  is a characteristic length, and  $\mu$  is the dynamic viscosity of the flow medium. The Reynolds number of a flow describes the ratio of inertial and viscous forces within a flow. Depending on the scenario being

investigated, several different characteristic lengths may be used to calculate  $Re$ . One value that is common when characterizing whether a point in a boundary layer flow is laminar or turbulent is the streamwise ( $x$ ) dimension from the leading edge of the flat plate to the point of interest. The notation  $Re_x$  is typically used when this dimension is used as the characteristic length in equation 2.1. Although different sources cite slightly different numbers, Cengel and Cimbala (2014) note that up to  $Re_x \approx 10^5$  a laminar boundary layer will occur on a smooth, flat plate. In the range of approximately  $10^5 < Re_x < 10^6$ , flows are considered transitional. In a transitional boundary layer, disturbances begin to propagate and grow, however, the flow retains some linear characteristics. For  $Re_x \approx 10^6$  and above, the boundary layer will likely be turbulent and have highly non-linear characteristics.

Turbulent boundary layers can generally be divided into an inner layer where viscous and Reynolds stresses are dominant, and an outer layer where the pressure field, momentum, and Reynolds stresses all contribute significantly to the characteristics of the flow. The inner layer is of great interest for many researchers as it is where a majority of turbulence production occurs within turbulent boundary layers (Kim et al., 1970; Panton, 2001). As such, many characteristics of the outer layer are driven by mechanisms occurring within the inner layer. The inner layer encompasses the approximate range  $y/\delta < 0.1$ , where  $\delta$  is the boundary layer thickness (i.e. distance from wall at which mean flow speed equals  $0.99U_\infty$ ). Within the inner layer, variables are generally normalized using inner scaling and this normalization is denoted by a superscript “+” (e.g.  $y^+$ ). Variables with units of velocity are normalized by the friction velocity of the flow ( $u_\tau$ ). As well, variables with units of length are normalized by an inner length scale  $\delta_\nu = u_\tau/\nu$ , where  $\nu$  is the kinematic viscosity of the flow medium. The friction velocity of a turbulent boundary layer can be determined from the velocity profiles of both the viscous sublayer or the logarithmic layer of turbulent boundary layers. The viscous sublayer is a thin layer in turbulent boundary layers immediately next to the wall where viscous forces are dominant. Within this layer ( $y^+ < 5$ ), the velocity profile can be well approximated by the relation  $u^+ = y^+$ . Above the viscous sublayer is the buffer layer ( $5 < y^+ < 30$ ). Across this region there is a shift from viscous effects being dominant toward Reynolds stresses being dominant in the flow. Peak turbulence production occurs within the buffer layer and subsequently

decreases with increasing wall-normal distance (Kim et al., 1970). Beyond  $y^+ \approx 30$ , the logarithmic layer begins. Within this layer viscous effects become relatively negligible and the mean velocity profile across the remainder of the inner region and into the outer region follows a logarithmic profile. The interactions of the various layers within turbulent boundary layers, and between the turbulent boundary layer and the freestream flow are complex. In essence, however, as highlighted very succinctly by Robinson (1991), the turbulent boundary layer transforms kinetic energy from the freestream into turbulent fluctuations that are subsequently transformed into internal energy through viscous dissipation.

### 2.1.1 Coherent structures

Turbulent boundary layers exhibit many complex and non-linear characteristics that present a significant challenge to studying, modelling, and controlling these flows. A large proportion of research on turbulent boundary layers relies heavily on statistical quantification of these flows. While this is useful in many scenarios, developing greater understandings of the instantaneous structure and dynamics of turbulent boundary layers could be beneficial for a variety of current and future technologies. Consequently, a large amount of work has been done over the past several decades to characterize the coherent structures that occur in turbulent boundary layers. Coherent structures are commonly accepted as playing a critical role in the self-sustained mechanism of turbulence in wall-bounded flows (Robinson, 1991). As such, studying these structures presents a pathway for understanding many of the critical aspects of turbulent boundary layers without having to grapple with all the non-linear and chaotic elements within these flows.

Definitions for what constitutes a coherent structure in a turbulent boundary layer are generally quite nonspecific. This is partly a result of the wide range of scales and forms that coherent structures can exhibit. In Robinson (1991), coherent structures are defined as three-dimensional regions of space in a flow that demonstrate correlation within and/or between fundamental flow variables across spatio-temporal scales significantly larger than the smallest scales of the flow. This definition, while useful, exemplifies the trend toward open-ended definitions of coherent structures. Additionally, Jiménez (2018) provides a description that is similar in content and specificity to that

provided by Robinson (1991). This consistency in definition over almost 30 years highlights that, although coherent structures may allow for some simplified understandings of the instantaneous fields and dynamics of turbulent boundary layers, they still have significant complexities and require further investigation.

Despite the variety of forms that coherent structures can exhibit, there are several coherent structures that have been identified and are generally agreed upon as contributing significantly to the characteristics of turbulent boundary layers. Two of these important coherent structures are low-speed streaks and streamwise vortices. Figure 2.1 shows a simple schematic of several coherent structures including a low-speed streak and a streamwise vortex. Low-speed streaks, as the name may suggest, are characterized by streamwise elongated regions of relatively low-speed streamwise fluid occurring in the wall-normal range of  $y^+ < 40 - 50$  (Kline et al., 1967). The formation of low-speed streaks is generally attributed to some extent to streamwise vortices near the wall that lift up low-speed fluid close to the wall and concentrates it into elongated streamwise streaks (Kline et al., 1967; Panton, 2001; Jiménez, 2018). Kline et al. (1967) observed that the low-speed streaks undergo a gradual lift-up followed by oscillation and then “bursting” of the low-speed streak. They indicate that the bursting of low-speed streaks, and the subsequent ejection of near-wall fluid, likely plays a significant role in the production and transport of turbulence in turbulent boundary layers. A more modern interpretation of the bursting events is that they correspond with the passage of a vortex (Robinson, 1991). As such, when viewed from a fixed point, the localized and short-term burst event described by Kline et al. (1967) is observed. However, the burst event, in fact, has a much longer lifespan and continues to occur while the vortex persists and advects downstream. This understanding has led to growing use of the terms “ejection” and “sweep” as opposed to “burst”. Ejection and sweep motions are, respectively, the motion of low-speed fluid away from the wall and of high-speed fluid toward the wall. Analysis of the probability density function of streamwise and wall-normal velocity fluctuations within turbulent boundary layers (i.e. quadrant analysis) highlights that a majority of the strongest fluctuations correspond to ejection and sweep motions (Jiménez, 2018). Consequently, these two motions are centrally important to turbulence production and the transport of streamwise momentum across different layers of turbulent boundary layers.

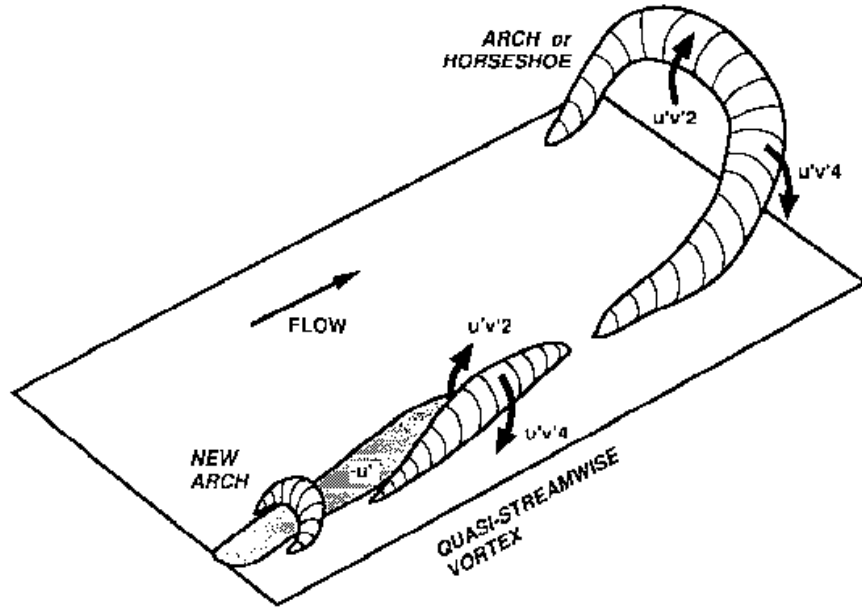


Figure 2.1: Schematic demonstrating the organization of a low-speed streak ( $-u'$ ), a quasi-streamwise vortex, and hairpin vortices (i.e. arch or horseshoe vortical structures) in a turbulent boundary layer. The relationship between ejection ( $u'v'2$ ) and sweep ( $u'v'4$ ) motions and the coherent structures is also illustrated. Taken with permission from Robinson (1991).

Hairpin vortices are a coherent structure that is closely correlated with the occurrence of ejection and sweep motions. They are perhaps the most relevant coherent structure for this thesis as they were the structures that were produced by the experimental apparatus that is described in section 3.1. These structures have seen a significant amount of investigation and were perhaps one of the earliest described coherent structures with the description of “horseshoe” vortices in turbulent wall-bounded flows by Theodorsen (1952). The basic structure of these vortices, as shown by figure 2.1, is characterized by a few elements. Two counter-rotating, quasi-streamwise vortices form the legs of the hairpin structure. The two legs are then connected to one another downstream by an arch-shaped vortex (also called the head) that is tilted away from the wall at approximately 45 degrees. The structure of hairpin vortices inherently promotes ejection and sweep motions. The rotation of the hairpin induces a focused ejection from the interior of the hairpin structure and a more diffuse sweep event around the outside of the structure, as indicated by figure 2.1. It should be noted that the importance of hairpin vortices to high Reynolds number turbulent boundary layers is somewhat uncertain (Jiménez, 2018). In transitional boundary layers and low Reynolds number

turbulent boundary layers, however, there is significant evidence of hairpin vortices. As such, they certainly play a role in turbulent wall-bounded flows with relatively low Reynolds numbers.

A well accepted mechanism for the formation of hairpin vortices in turbulent boundary layers is provided by Smith et al. (1984). The mechanism they proposed is somewhat demonstrated in figure 2.1 by the “new arch” vortex. Their model of hairpin vortex formation suggests that hairpin vortex roll up is initiated in the shear layer that surrounds low-speed streaks. The spanwise vorticity that rolls up on the top of low-speed streaks becomes the head of a hairpin vortex while the vorticity that rolls up on either side of the streak becomes the legs. Following their formation, the evolution of hairpin vortices can be understood through basic kinematics. As outlined by Adrian (2007), the head, being farther from the wall than the legs, will experience a higher mean velocity. Consequently, the head moves downstream at a greater rate than the legs, stretching and intensifying the structure. This subsequently causes the vortex to move further from the wall which causes additional stretching and strengthening. Therefore, this would suggest that newly formed hairpin vortices would be found closer to the wall and more mature hairpin vortices farther into the boundary layer. Support for this evolution process can be found in a number numerical and experimental works which have observed hairpin vortices throughout the inner and outer layers of turbulent boundary layers (Robinson, 1991; Panton, 2001; Adrian, 2007). This mechanism of growth and evolution of hairpin vortices is interesting as it highlights the potential importance of these vortices to characteristics across multiple different layers of turbulent boundary layers.

An additional important characteristic of hairpin vortices is the tendency for multiple hairpin vortices to form as a streamwise packet. One of the earliest references to the formation of hairpin vortex packets is given by Bandyopadhyay (1980). They noted that large slanting structures observed in turbulent boundary layers could be explained by a streamwise packet of hairpin vortices where the maturity of the hairpin vortices increases with streamwise location. Flow visualizations of both simulated and physical turbulent boundary layers by Adrian et al. (2000) and Hommema and Adrian (2003) provide support for the occurrence of hairpin packets. They observed what can be interpreted as a series of hairpin heads organized in a structure reminiscent of that suggested by Bandyopadhyay (1980). As well, Zhou et al. (1996) observed that new hairpin vortices can

form both upstream and downstream of an initial strong hairpin vortex. From this observation, they proposed an “autogeneration” mechanism whereby hairpin packets result as new vortices are induced by subsequent generations of hairpin vortices. The evidence of the occurrence of hairpin packets and the potential that they can arise through an autogeneration mechanism is a further indication that these structures may contribute significantly to the characteristics of turbulent boundary layers.

## 2.2 Active control of turbulent wall-bounded flows

Modern control of turbulent flows is largely concerned with developing active strategies for controlling these flows. Achieving active control of turbulence presents enormous potential for improving the efficiency and efficacy of innumerable real-world systems. Given this, growing focus has been applied to the development of AFC techniques over the past several decades (Gad-el Hak, 2000; Brunton and Noack, 2015; Duriez et al., 2017). A major driver of the increasing attention toward AFC has been a result of improvements in electronics and computing over the past several decades. This has led to the development of better sensors, actuators, and computing systems for real-time control that make the investigation of AFC a more attainable venture.

Among the numerous potential applications of AFC, the control of turbulent wall-bounded flows is of great interest due to the prevalence of these flows in innumerable systems. A major detrimental effect of turbulent boundary layers in many technologies where they occur is the large amount of skin friction drag that they cause (Schlichting and Gersten, 2017). Choi et al. (1994) notes that skin friction drag reductions in excess of 60% can theoretically be achieved by steering turbulent boundary layers toward more laminar states. Unfortunately, as highlighted in section 2.1, turbulent boundary layers are highly non-linear and chaotic in nature. This makes developing AFC strategies for these kinds of flows extremely challenging. The following section discusses a branch of AFC strategies called reactive control with a specific focus on the work of Choi et al. (1994) and the subsequent investigations that have built upon it. The reactive control strategies proposed by Choi et al. (1994) provided significant inspiration of the reactive control conducted for this thesis. As well, given the use of wall-normal motion and deformation of the wall in this thesis,

a discussion of this actuation technique for AFC is provided in section 2.2.2.

### 2.2.1 Reactive control

Reactive control describes AFC strategies where sensors detect oncoming coherent motions and actuators attempt to favourably influence them (Gad-el Hak et al., 1998). As described by section 2.1, coherent structures contribute significantly to the characteristics of turbulent boundary layers. As such, through targeting one or multiple coherent structures, reactive control has the potential to significantly impact turbulent boundary layers in a desirable manner without the need to consider all of the non-linear and chaotic elements of these flows.

While reactive control simplifies the problem of turbulence control somewhat, it is still a difficult task given that detecting coherent structures is not trivial and the optimal approach for manipulating coherent structures is likewise unclear. Choi et al. (1994) investigated reactive control using the direct numerical simulation (DNS) of a turbulent channel flow on a coarse grid with  $32 \times 65 \times 32$  grid points (streamwise, wall-normal, and spanwise, respectively). A finer grid with  $128 \times 129 \times 128$  grid points was used for verification of a select number of cases. At each time instant of the simulation, reactive control was realized by setting the boundary condition for each grid point of the wall to a velocity that was proportional to one detected at a grid point above the wall. Of the control strategies that Choi et al. (1994) investigated, we will specifically focus on control strategies based on streamwise and wall-normal velocity components as these strategies are most relevant to those evaluated in the current investigation. These were so called  $u$ -control and  $v$ -control, where  $u$  and  $v$  denote streamwise and wall-normal velocity fluctuations, respectively.

Choi et al. (1994) defined  $u$ -control as inducing streamwise fluid motions at the wall that were proportional to streamwise velocity fluctuations measured at a streamwise-spanwise plane close to the wall. Both compliant and opposing actuations were investigated for  $u$ -control. Compliant actuations indicate that the streamwise velocity fluctuations induced at the wall had the same sign as those measured in the flow and vice versa for opposing actuations. For  $u$ -control, Choi et al. (1994) observed a 10% drag reduction when applying compliant actuations and a drag increase when applying opposing actuations. They indicate that compliant actuations led to a reduction of the

wall-normal gradient of streamwise velocity (i.e.,  $\partial u/\partial y$ ) close to the wall while opposing actuations increased this gradient in the near-wall region. This conclusion is supported somewhat indirectly by the experimental investigation of a reactive control technique similar to  $v$ -control (described below) by Rebbeck and Choi (2006). They applied active wall-normal blowing at a single point in a turbulent boundary layer to counteract sweep motions detected in real-time by an upstream hot-wire anemometer. Their investigation showed that the wall-normal blowing intended to oppose sweep motions also caused some degree of “in-phase” (compliant)  $u$ -control due to the advection of the blowing actuation. The advection of the wall-normal blowing with the targeted sweep motion allowed the opposing motions to continue to interact downstream of the actuation location. This led to prolonged opposition of the wall-ward advance of sweep motions which reduced the wall-normal gradient of streamwise velocity near the wall. It is worth noting that  $u$ -control received minimal attention in Choi et al. (1994) and has likewise seen almost no further subsequent investigation. This is attributed to the fact that Choi et al. (1994) found it was less effective at reducing skin friction drag in comparison to other reactive control schemes they investigated.

The  $v$ -control strategy, as Choi et al. (1994) defined it, involved detecting ejection and sweep motions based on their wall-normal velocity at a streamwise-spanwise plane near the wall, and targeting them with proportional wall-normal fluid motions induced at the wall. It should be noted that Choi et al. (1994) and most subsequent works on  $v$ -control have only investigated opposing actuations, where wall-normal fluid motions induced at the wall have an opposite sign to those measured in the flow. This type of  $v$ -control is also commonly referred to as opposition control. Unless otherwise noted, references to  $v$ -control in this section should be assumed to denote  $v$ -control where opposing actuations are being applied.

Choi et al. (1994) found that  $v$ -control produced a 25% drag reduction. The opposition of sweep motions is one of the mechanisms they not as contributing to this drag reduction. This action of  $v$ -control pushes high shear rate regions away the wall where they contribute less skin friction drag. As well, through investigating the effect of  $v$ -control on a minimal channel flow and an isolated vortex pair, they also observed that  $v$ -control prevents the lift up of near-wall vorticity. This decreases the formation of streamwise vortices to some extent which, in turn, reduces skin friction

drag. A similar numerical investigation of  $v$ -control by Wang et al. (2016) further supports these conclusions. They characterized the circulation of vortices in a DNS simulated turbulent channel flow during  $v$ -control. They found that  $v$ -control caused weaker and relatively fewer vortices to occur in the flow.

It is noted in Choi et al. (1994) and many subsequent works on  $v$ -control, that the wall-normal location of the streamwise-spanwise sensor plane,  $y_s^+$ , is critical to the effectiveness of  $v$ -control. Choi et al. (1994) investigated four  $y_s^+$  values of 5, 10, 20, and 26 and determined that  $y_s^+ = 10$  produced the greatest drag reduction. Furthermore, for  $y_s^+ = 26$ , they observed a steep increase in drag. Several other numerical studies also found drag reductions were achieved by  $v$ -control with approximately  $y_s^+ < 20$ ; however for  $y_s^+ > 20$ , the effect of  $v$ -control becomes unstable and there is a substantial drag increase (Hammond et al., 1998; Lim and Kim, 2004; Chung and Talha, 2011; Deng and Xu, 2012). Deng and Xu (2012) used the streak transient growth (STG) mechanism proposed by Schoppa and Hussain (2002) to explain the change in behaviour of  $v$ -control based on variation in  $y_s^+$ . They note that in the STG stage of streamwise vortex development, wall-normal velocity fluctuations change in sign at  $y^+ \approx 20$ . As such, they indicate that for  $v$ -control with  $y_s^+ < 20$ , the desired opposition of wall-normal velocity fluctuations occurs; however, for  $y_s^+ > 20$ , fluid motions induced at the wall may be compliant with the wall-normal velocity fluctuations closest to the wall.

Additionally, several numerical simulations have investigated the impact of different amplitudes of opposing actuations. Chung and Talha (2011) and Deng and Xu (2012) found that by applying weaker opposing actuations, drag reductions could be achieved with  $y_s^+$  values of up to 30. Furthermore, Chung and Talha (2011) also found that applying actuations greater in strength than the velocity fluctuations measured at the sensor plane led to  $v$ -control becoming hydrodynamically unstable and inducing significant drag increases at all the sensor plane locations they tested ( $5 < y_s^+ < 30$ ). They attribute this instability to the occurrence of a positive feedback loop when stronger actuations are applied. Deng et al. (2014) likewise investigated strengthened  $v$ -control, however, they added what they refer to as “time relaxation” to their adapted  $v$ -control scheme. The time relaxation was essentially a form of low-pass filtering and considered the velocity induced at the wall at a previous time step in calculating the velocity that would be induced at the current

timestep. The time relaxation was successful at stabilizing strengthened  $v$ -control and they were able to achieve a maximum drag reduction of 33% using  $y_s^+ = 15.4$  and wall-normal suction and blowing significantly larger in amplitude than the wall-normal velocities measured at the sensor plane.

Beyond the investigation of variables such as actuation amplitude and sensor plane location, different actuation techniques have also been explored as an alternative to suction and blowing. Endo et al. (2000), Kang and Choi (2000), and Pamiés et al. (2011) numerically investigated adaptations of  $v$ -control that used active wall deformation in the wall-normal direction. As such, the wall was moved at opposing velocities to wall-normal fluid velocities measured at the sensor plane. Both Endo et al. (2000) and Kang and Choi (2000) investigated cases with complete control of the deformation of all grid points of the wall. With this full control, they were able to achieve drag reductions in the range of 12 – 17%. The root-mean-square (RMS) wall deformation was in the range of 1 – 3.2 wall units for these investigations. As well, Endo et al. (2000) and Pamiés et al. (2011) numerically investigated semi-realistic scenarios where active wall-deformation was achieved using an array of finite size actuators that were elongated in the streamwise direction to target streamwise vortices. Endo et al. (2000) achieved a drag reduction similar to that of their case with complete control of the wall’s deformation. Pamiés et al. (2011), however, noted a negligible drag reduction in their simulation. The actuator design and specific reactive control employed by these two works does differ somewhat and, as such, this likely explains their opposing results. This highlights the significant difficulty of developing active turbulence control in that two works applying seemingly similar control strategies can have much different levels of efficacy.

Despite the many promising numerical results of  $v$ -control and associated reactive control strategies highlighted so far, there has been very little experimental investigation related to  $v$ -control. Rebbeck and Choi (2006) represents one of the only experimental investigations of real-time control meant to mimic  $v$ -control. They applied intermittent wall-normal blowing at a single location in a turbulent boundary layer to oppose sweep motions detected by an upstream hot-wire anemometer. They demonstrated that the penetration of sweep motions toward the wall can be blocked by an opposing blowing actuation induced at the wall. As well, the investigation by Goldin et al. (2013)

into the damping of Tollmien-Schlichting (TS) waves in a laminar boundary layer is a tangential example of an experimental implementation of reactive control. Goldin et al. (2013) used hot-wire anemometers to detect TS waves and then controlled a streamwise cascade of bars that could be actuated in the wall-normal direction to induce a “counter-wave”. They were able to reduce the RMS amplitude of TS waves by up to 85% with this strategy. The results of Rebbeck and Choi (2006) and Goldin et al. (2013) are positive indications that reactive control can be achieved in experimental settings. However, significant development is needed to push experimental implementations of reactive control toward more complex and applicable states.

### **2.2.2 Actuation using motion and deformation of the wall**

As will be outlined in chapter 3, active motion and deformation of the wall in the wall-normal direction was chosen as the actuation technique for the reactive control outlined by this thesis. Therefore, it is necessary to provide some deeper discussion of this specific actuation technique for AFC. A few investigations have demonstrated the potential of active wall-normal surface deformation for actuating wall-bounded flows. Breuer et al. (1989) represents perhaps the earliest example of an experimental application of active wall-normal surface deformation for AFC. They employed a series of pneumatically driven flexible membranes embedded in the wall to oppose disturbances generated in a laminar boundary layer by an upstream pneumatically driven flexible membrane. Their work indicated that the active wall deformation was successful at delaying the growth of the artificial disturbance using actuations relatively weaker than the disturbance. As well, the numerical work of Carlson and Lumley (1996) is another foundational work on active wall-normal surface deformation for flow control. They employed the simulation of a minimal flow unit to evaluate the effects of an outward Gaussian wall deformation with an amplitude of approximately twelve wall units on a pair of high- and low-speed streaks in the near-wall region. The wall-normal deformation was found to lift whichever streaky structure it occurred below. This lifting of one streaky structure caused the adjacent, opposing structure to expand. The lifting of high- and low-speed streaks was associated with drag reductions and increases, respectively. Additionally, the investigations of Kim et al. (2003) and Gibeau and Ghaemi (2022, 2023) evaluated the effects

of localized periodic wall-motion on laminar and turbulent boundary layers. These investigations used a circular membrane to replace a section of the wall and actuated the membrane at various frequencies using an electromagnetic linear actuator. They observed that a series of relatively strong high- and low-speed streamwise motions were produced by the downward and upward wall motions, respectively, in both laminar and turbulent boundary layers. Gibeau and Ghaemi (2023) notes that active wall motions induce streamwise velocity fluctuations that are stronger than the corresponding wall-normal velocity fluctuations. This suggests that this type of actuation is also suitable to control strategies that focus on inducing streamwise velocity fluctuations. Furthermore, Cattafesta and Sheplak (2011) note that these types of actuators are becoming more viable with technological advances in the areas of piezoelectric actuators and microelectromechanical systems. Consequently, this actuation technique was chosen for the current investigation given the numerical and experimental demonstrations of the capabilities of active wall deformation for AFC and the growing viability of these actuators.

## 2.3 Particle image velocimetry

Particle image velocimetry (PIV) is a non-intrusive, optical flow measurement technique that has become a fundamental tool for fluid dynamics research over the past several decades. To date, the vast majority of uses of PIV have been for offline analyses of flows, where the flow is imaged and then the PIV analysis is conducted after the fact. A brief review of the working principles of PIV is provided by section 2.3.1. Note that for detailed discussions of PIV, readers are referred to Raffel et al. (2018).

The primary use of PIV as an offline measurement tool can be attributed to the high computational cost of the technique and the large amounts of data involved in it. These factors present significant obstacles to creating real-time PIV (RT-PIV) systems. Despite this, the potential of PIV as a real-time sensor for flow visualization, analysis, and control has long been recognized. Efforts to develop RT-PIV systems date back to Arik and Carr (1997) who developed an RT-PIV system to aid in tuning standard PIV systems. Section 2.3.2 outlines several topics relevant to RT-PIV such as factors contributing to their latency and some algorithm and hardware optimizations that

have been applied for the development of RT-PIV systems.

### 2.3.1 Principles of PIV

PIV has been an extremely powerful tool for advancing understandings of fluid dynamics on a wide variety of scales and in numerous different scenarios. In this thesis, planar PIV was used to capture all flow measurements. As such, this is the only form of PIV that will be discussed.

PIV requires specific flow characteristics in order to be a viable measurement technique. Since it is an optical technique, one of the critical requirements is that the flow medium and portions of the apparatus containing the flow must be transparent to allow optical access to the interior of the flow. As well, seeding particles must be added to the flow medium. The seeding particles are what is actually imaged and analyzed during PIV. As such, the seeding particles must have characteristics that allow them to closely follow the flow field and to scatter a significant amount of light so that they will appear clearly in images. For water flows, such as that used in the experiments outlined by this thesis, it is common to use solid or hollow glass spheres with diameters in the range of one to tens of micrometers. These particles are well suited for PIV in water flows as their size and density allow them to closely follow the flow field. Furthermore, they also have an excellent ability to scatter light. Melling (1997) provides an in-depth discussion of seeding particles for PIV and the considerations that must be made to select appropriate particles for different flow scenarios.

With regards to capturing PIV images, figure 2.2 shows a schematic of a basic planar PIV imaging system. The system consists of a camera that is focused on an image plane that encompasses the desired field of view (FOV) within the flow. A laser sheet with a thickness of  $\sim 1$  mm is used to illuminate the image plane for a brief moment during image exposures. Precise timing between image exposures and illumination of the flow by the laser sheet is critical for enabling the later calculation of velocity vector fields from image pairs. A standard timing diagram for a PIV imaging system is illustrated by figure 2.3. A laser pulse with a duration of several nanoseconds occurs during each image exposure. This extremely brief illumination period allows for a “frozen” image of the flow to be captured at the instant of the laser pulse. Additionally, as the fluid medium is transparent, the frozen image only shows the illuminated seeding particles suspended in the flow.

Two laser pulses with a temporal spacing of  $\Delta t$  are subsequently able to expose a PIV image pair with the desired timing. Note that figure 2.3 shows the timing diagram for a PIV system using a double-frame camera. Each of the short image exposures in figure 2.3 corresponds to the first frame of an image pair and each longer exposure is the second frame. The short first image exposure followed by a longer second exposure is a characteristic of double-frame cameras. These cameras are commonly used in PIV applications as they have especially small interframe times on the order of 1  $\mu$ s. This allows for very small  $\Delta t$  values that are necessary for PIV measurements of high-speed flows. It is also possible to use standard video or high-speed video cameras for many applications of PIV where the flow speed is more moderate.

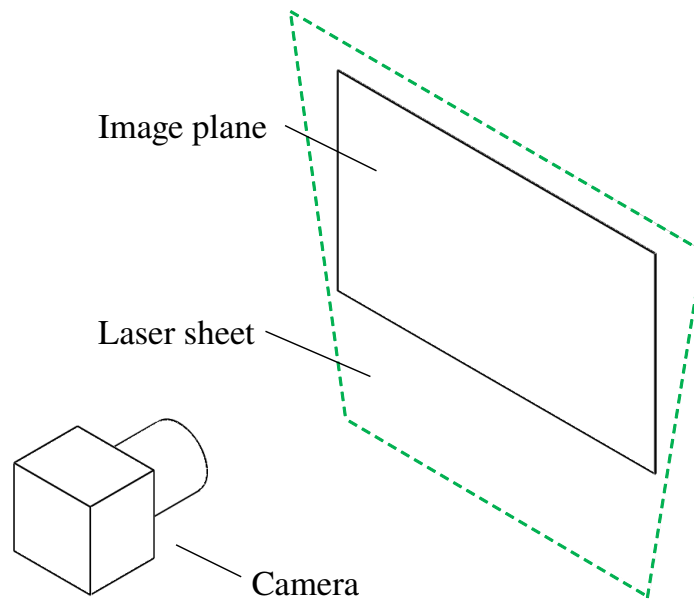


Figure 2.2: Schematic of a planar PIV imaging system.

For standard PIV, all the desired image pairs are collected and then undergo PIV processing to calculate velocity vector fields. Figure 2.4 provides a basic visualization of a planar PIV algorithm. The first step of PIV processing involves dividing each frame of an image pair into many smaller sub-images that are referred to as interrogation windows (IWs). Corresponding IWs from each frame of an image pair are then compared using a statistical technique called cross-correlation. Cross-correlation allows the similarity of two signals to be measured at different offsets to one

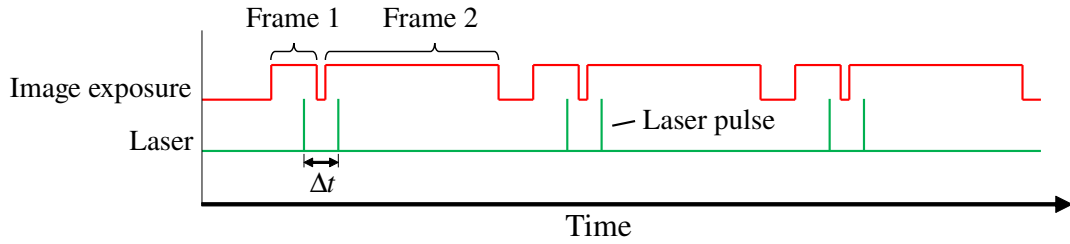


Figure 2.3: Timing diagram for a PIV system illustrating the coordination of a laser and a double-frame camera to acquire PIV image pairs. Each short image exposure corresponds to frame 1 of an image pair while the longer image exposure corresponds to frame 2.

another. A two-dimensional cross-correlation is used for image data and allows the offset to be found where IWs have the greatest similarity to each other. This offset is taken as the particle displacement ( $\Delta\mathbf{s}$ ) that occurred within the IW over  $\Delta t$ . To achieve accurate  $\Delta\mathbf{s}$  values,  $\Delta t$  should be chosen so that the maximum displacement of particles between image frames is limited to approximately  $N/4$  to  $N/3$ , where  $N$  is the side length of IWs being used (Raffel et al., 2018). After the displacement of particles is found using cross-correlation, a velocity vector is calculated using the relation  $\mathbf{U} = \Delta\mathbf{s}/\Delta t$ , where  $\mathbf{U} = (U, V)$  is a velocity vector of the flow. This process is repeated for all the IWs in an image pair to produce a complete velocity vector field for the flow over the imaged FOV.

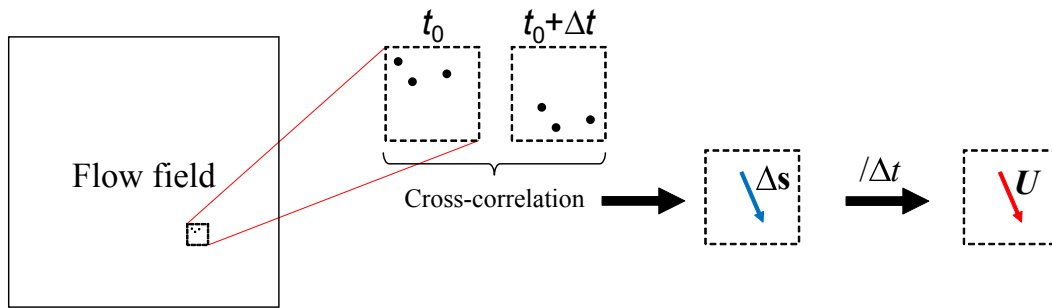


Figure 2.4: Visualization of a planar PIV algorithm. The displacement of particles within an interrogation window over a time period  $\Delta t$  is determined through cross-correlation. A velocity vector,  $\mathbf{U}$ , is then calculated by dividing the particle displacement by  $\Delta t$ .

The accuracy of PIV can be improved through a variety of techniques. One common technique is to implement multiple iterative passes of PIV processing. With this technique, each subsequent pass of PIV processing is informed by the results of the prior pass and IWs are shifted and/or

deformed to achieve larger signal-to-noise ratios in their cross-correlations. As well, PIV algorithms commonly involve a sub-pixel interpolation step that allows the displacements found through cross-correlation to be refined below the scale of individual image pixels. Outside of the PIV algorithm itself, there are likewise a variety of image pre-processing techniques and vector field post-processing techniques that can be applied prior to or following PIV processing to improve the quality of PIV measurements. Readers are referred to Raffel et al. (2018) for detailed discussions of these various techniques.

### **2.3.2 RT-PIV**

The potential of RT-PIV to be a powerful tool for real-time visualization, analysis, and control of flows has been recognized for several decades. Arik and Carr (1997) described the first effort at developing an RT-PIV system. They developed an RT-PIV system with the goal of using it for optimizing standard PIV setups. Since this initial work, a number of other researchers have demonstrated RT-PIV systems. Early RT-PIV systems required complex and custom hardware systems in order to handle the large amounts of data and significant computational requirements of PIV algorithms (Maruyama et al., 2001; Fujiwara et al., 2003; Siegel et al., 2003; Yu et al., 2006; Aubert et al., 2006; Muñoz et al., 2009). Furthermore, none of these early RT-PIV systems appear to have gone on to be used in further experiments. As such, it seems likely that these systems were not practically applicable.

In recent years, the improvement of computing technologies and the commonality of machine vision applications in industry has greatly improved the feasibility of RT-PIV systems. Willert et al. (2010) demonstrated the first practical application of a RT-PIV system. They used an RT-PIV system producing fifteen vector fields per second to control vortex formation on an airfoil immersed in an oil tunnel facility. More recently, Gautier and Aider (2015) demonstrated a groundbreaking RT-PIV system that leveraged GPU architecture and an optical flow algorithm developed by Le Besnerais and Champagnat (2005) to enable calculation of dense velocity vector fields from 2-megapixel images at a rate of up to several hundred velocity fields per second.

While RT-PIV is an exciting technology, it should be noted that it is not a practical sensor for

real-world applications of AFC. Rather, RT-PIV allows for physical experimentation that begins to approach the complexity seen in numerical works on AFC. Once effective AFC strategies are developed with the wealth of information provided by RT-PIV, efforts can begin to be made to transition these strategies to more practical states using wall-measurable flow variables. This approach has been applied frequently in numerical investigations of reactive control (Choi et al., 1994; Lee et al., 1997, 1998; Kang and Choi, 2000; Endo et al., 2000; Xu et al., 2002; Lorang et al., 2008; Ge et al., 2015).

RT-PIV applies essentially the same working principles as PIV, except that it involves implementing some additional hardware components to allow real-time processing of images as they are captured. Immediate access to PIV images can be accomplished through a variety of methods such as the use of a frame grabber and compatible camera or using a USB camera that streams images directly to a computer. These imaging systems are generally only capable of operating at fixed frequencies and do not have the double-frame capability that is common for PIV cameras. This should not be an issue for most applications of RT-PIV, however, as the applicability of RT-PIV to high-speed flows that require double-frame cameras is likely limited due to the latency of these systems. This latency of RT-PIV systems between measurement of the flow and output of velocity field measurements is discussed in section 2.3.2.1. Following this, discussions of algorithm and hardware optimizations that have been applied in RT-PIV systems are outlined in sections 2.3.2.2 and 2.3.2.3, respectively.

### **2.3.2.1 Latency**

The description of RT-PIV as "real-time" is perhaps somewhat misleading in certain situations because there is always some level of delay involved in RT-PIV systems. There are a variety of things that can be done to reduce this delay, however, a system that may be considered "real-time" for one flow or fluid dynamics application, may not be for another. Consequently, this is a hurdle to the wider application of RT-PIV as researchers must individually determine what an acceptable delay is for their specific application and flow.

Figure 2.5 shows a sample timing diagram for an RT-PIV system to illustrate the different

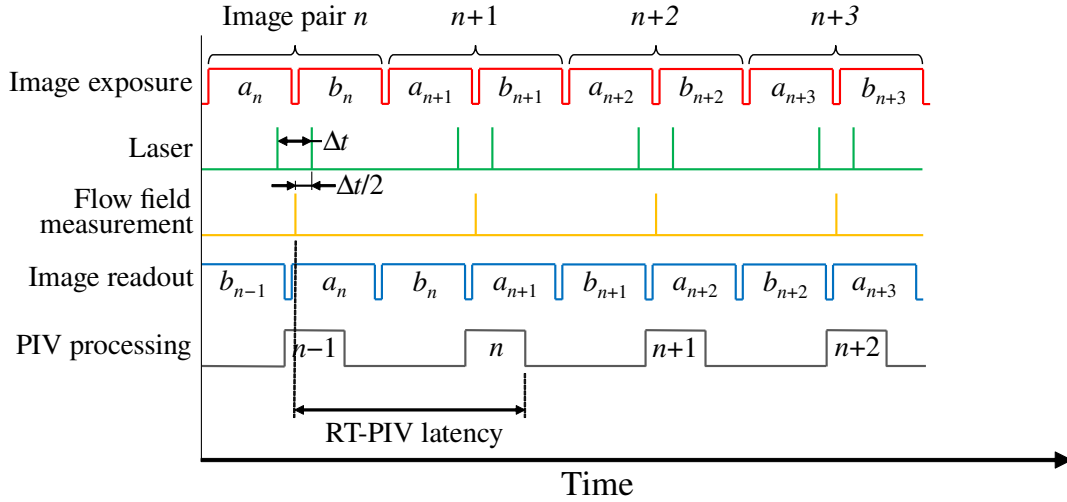


Figure 2.5: Timing diagram of an RT-PIV system demonstrating the various steps contributing to the overall latency of the system. The symbols  $a$  and  $b$  in the figure denote the first and second frames of an image pair, respectively. The spikes on the flow field measurement (yellow) line are placed at the midpoint between laser pulses for each image pair and indicate the instants at which the flow field is measured by the RT-PIV system.

factors contributing to the latency of these systems. In determining this latency value, it is first necessary to define the time when measurements of the flow field are taken. It is common in PIV to define the flow field measurement instant as the midpoint between the laser pulses that expose an image pair. This is highlighted by the yellow "flow field measurement" line in figure 2.5. The time that passes from this measurement instant to when a vector field is output by the RT-PIV system is defined as the latency of the system. Figure 2.5 illustrates that there are three primary components of this delay. Two of these components are the image exposure time and the image readout time. In both cases, it is primarily the exposure and readout of the second image frame that contributes to the system latency. This is because the laser pulse exposing the first image can be placed close to the end of the exposure time of the first image. Additionally, the first image is then read out during the exposure time of the second image and does not contribute to the overall latency. Both the image exposure time and the readout time can be minimized to a certain extent through camera selection. The exposure and readout times can be reduced by choosing a camera with a high frame rate. Increasing the camera frame rate reduces exposure times while maintaining a small delay between image exposures. As well, cameras that are capable of high frame rates will

accordingly have shorter image readout times to allow those high frame rates.

The third component of the RT-PIV system latency is the PIV processing time. PIV is a highly computationally expensive process. This is primarily due to its use of cross-correlation to determine the displacement of particles between image frames. As such, there are two approaches that can be taken with regards to reducing the PIV processing time: first is to optimize the PIV algorithm to reduce its computational intensity; and second is to implement more powerful computing hardware to allow the numerous operations to be completed faster. These options are discussed in the following two sections.

### 2.3.2.2 Algorithm optimization

PIV processing times can be reduced significantly through optimization of the PIV algorithm. Cross-correlation is a core element of traditional PIV algorithms and it likewise accounts for a majority of the computation cost. Consequently, optimizing the cross-correlation calculations can allow for significant performance improvements. There are two primary ways in which 2D cross-correlations can be calculated. The first method, direct cross-correlation (DCC), is shown by equation 2.2,

$$C(x, y) = \sum_{i=-M}^M \sum_{j=-N}^N A(i, j)B^*(i + x, j + y) \quad (2.2)$$

where  $C$  is the cross-correlation map,  $A$  and  $B$  are matrices, and the superscript “\*” denotes complex conjugation. A brief examination of equation 2.2 demonstrates that the number of operations needed to calculate the cross-correlation of even moderately sized arrays grows extremely quickly. In PIV it is common to use  $64 \times 64$ -pixel IWs. If we consider the cross-correlation of two IWs of this size, the number of operations needed to calculate this cross-correlation is approximately  $64^4$  ( $\sim 17$  million). When you further consider analyzing even a small format image pair such as 0.25-megapixels ( $512 \times 512$ -pixels), the number of operations required to calculate a full vector field increases to over one billion. To reduce the computational expense of DCC, Fujiwara et al. (2003) and Aubert et al. (2006) applied a truncated DCC technique in their RT-PIV systems where a larger IW from the first frame of each image pair was cross-correlated with a smaller IW from

the second frame. While this can significantly reduce the computations required for each cross-correlation compared to using equally sized IWs, this is not a standard approach used in PIV and could significantly impact the accuracy of flow measurements.

The second technique that can be applied for conducting cross-correlation is to use a fast Fourier transform cross-correlation (FFT-CC). FFT-CC is conducted according to equation 2.3,

$$C = F^{-1}[F(B)F(A)^*] \quad (2.3)$$

where  $F(\dots)$  denotes the Fourier transform of contents within the brackets,  $F^{-1}(\dots)$  denotes the inverse Fourier transform, and  $A$  and  $B$  are matrices. By leveraging characteristics of the frequency domain, FFT-CC is much less computationally expensive compared to DCC. As was calculated by Fujiwara et al. (2003), the number of operations required to calculate the FFT-CC of two  $64 \times 64$ -pixel IWs is  $\sim 600,000$ . This is roughly 35-times fewer operations than needed to calculate the DCC of two  $64 \times 64$ -pixel IWs. Given this, the use of FFT-CC rather than DCC can significantly increase the speed of PIV algorithms with relatively little impact on the quality of results.

Interestingly, many of the early works on RT-PIV chose DCC over FFT-CC (Maruyama et al., 2001; Fujiwara et al., 2003; Siegel et al., 2003; Yu et al., 2006; Aubert et al., 2006; Muñoz et al., 2009). This choice is perhaps a result of a lack of access to fast Fourier transform algorithms in the real-time hardware and software implemented by these researchers. Both Schiwietz and Westermann (2004) and Willert et al. (2010), however, did implement FFT-CC in their RT-PIV system. This demonstrates that FFT-CC can be applied in real-time given appropriate selection of processing hardware and software.

Outside of reducing the computational expense of cross-correlations, another option for algorithm optimization is to use optical flow algorithms instead of traditional cross-correlation based PIV algorithms. Due to the tangential nature of the topic of optical flow to the work outlined in this thesis, only a brief discussion of its application for RT-PIV is provided. A more detailed summary of optical flow and its application for fluid flow measurements is provided by Heitz et al. (2010). The use of an optical flow algorithm in an RT-PIV system was demonstrated by Gautier and Aider (2015). They implemented the ‘‘FOLKI’’ (iterative Lucas-Kanade optical flow, in French) algorithm

developed by Le Besnerais and Champagnat (2005) to calculate velocity fields from traditional PIV image pairs. The FOLKI algorithm has the benefit of not relying on computationally intensive cross-correlations. Rather, it utilizes a more efficient iterative sum of square differences correlation process to determine the displacements that occur between frames of an image pair (Le Besnerais and Champagnat, 2005). This results in the optical flow algorithm being much less computationally expensive which, in turn, reduces the processing time. Furthermore, as demonstrated by Champagnat et al. (2011), the FOLKI optical flow algorithm can produce flow field measurements of a similar quality to those produced using traditional PIV algorithms. Consequently, optical flow algorithms may be an excellent option not only for RT-PIV, but also for the next generation of faster PIV processing algorithms for standard PIV.

### **2.3.2.3 Hardware optimization**

In addition to optimizing the PIV algorithm, the implementation of specialized computing hardware can likewise significantly reduce PIV processing times in RT-PIV systems. The selection of hardware to improve PIV processing times revolves largely around choosing hardware that enable large amounts of parallel processing. PIV algorithms, and certain optical flow algorithms, are highly parallel. In traditional PIV algorithms this is evident as each vector calculation involves the same process and is completely independent of any other vector calculations. Consequently, with proper processing hardware, all the velocity vectors could be calculated at the same time. This would reduce the PIV processing time to that required to calculate a single velocity vector. In the literature there are two pieces of hardware that have primarily been implemented to improve the parallel processing capabilities of RT-PIV systems. These are field programmable gate arrays (FPGAs) and graphical processing units (GPUs).

As summarized by Yu et al. (2006), the major benefits of FPGAs are their modularity, programming flexibility, and allowance of high levels of parallel processing. FPGAs were implemented in the RT-PIV systems described by Maruyama et al. (2001), Fujiwara et al. (2003), Aubert et al. (2006), and Muñoz et al. (2009). Perhaps the most impressive result was achieved by Aubert et al. (2006). Their RT-PIV system was able to produce approximately 330 vector fields per second,

where the images being analyzed were  $512 \times 512$ -pixels and  $32 \times 32$ -pixel IWs with no overlap were used. As noted previously, Aubert et al. (2006) implemented an unvalidated truncated DCC strategy for calculating cross-correlations. Despite this, the capabilities of their RT-PIV system are impressive and highlight the potential of FPGAs for allowing fast PIV processing.

GPUs are likewise well suited to increasing PIV processing speeds as their architecture is well suited for enabling large amounts parallel processing. Schiwietz and Westermann (2004) provide the first example of integration of a GPU into a PIV system. They note being able to produce ten velocity fields per second, where  $1024 \times 1024$ -pixel images and  $16 \times 16$ -pixel IWs were used. More recently, Gautier and Aider (2015) demonstrated an RT-PIV system which implemented both a highly parallel optical flow algorithm and a GPU. Their system was able to produce up to 224 velocity fields per second from  $2048 \times 1088$ -pixel images. Additionally, where most of the RT-PIV systems discussed so far have not been utilized beyond the initial work describing them, the system described by Gautier and Aider (2015) was utilized in several later active flow control investigations (Gautier and Aider, 2014; Gautier et al., 2015; Varon et al., 2019). Although a non-traditional algorithm was used, the speed and subsequent application of the RT-PIV system described by Gautier and Aider (2015) demonstrates that GPUs are a viable option for reducing PIV processing times in RT-PIV systems.

Lastly, it should be noted that standard central processing units (CPUs) are also capable of being harnessed for the purposes of RT-PIV, although at significantly lower speeds compared to what FPGAs and GPUs can produce. Modern multi-core CPUs have some limited parallel processing capabilities and have the significant benefit of being much more accessible than FPGAs and GPUs. The RT-PIV system described in this work as well as those described by Siegel et al. (2003) and Willert et al. (2010) utilized CPUs for real-time PIV processing. The RT-PIV system described by Willert et al. (2010) was capable of producing fifteen velocity fields per second from  $1024 \times 768$ -pixel images and using  $32 \times 32$ -pixel IWs. As well, they note that the latency of their RT-PIV system was  $\sim 100$  ms. As such, for low-speed flows such as the oil flow investigated by Willert et al. (2010), effective RT-PIV systems can be developed utilizing only CPUs for PIV processing.

## Chapter 3

# Experimental Methodology

This chapter describes the experimental methodology developed and applied for conducting the reactive control of streamwise and wall-normal velocity fluctuations. Experiments were conducted on the underside of a flat plate apparatus mounted in a water flume at the University of Alberta. This flow facility is described in chapter 3.1. An active deformable surface with sixteen independent actuation locations was developed to serve as the actuation system for the reactive control and is described in chapter 3.2. Flow measurements were carried out using particle image velocimetry (PIV) for *a posteriori* analysis of the reactive control as outlined in chapter 3.3. To provide clear distinction, this standard PIV system will be referred to as the “offline PIV” system. An RT-PIV system provided real-time flow measurements for the reactive control system and is described in chapter 3.4. The two PIV systems were synchronized to allow for a single laser to provide illumination of the FOVs of both systems. Lastly, the two reactive control algorithms investigated in this work are described in chapter 3.5.

### 3.1 Flow setup

All experiments for this work were conducted in a water flume at the University of Alberta. The test section of the water flume has a width of 64 cm and a length of 5.2 m. As well, the flume was filled with water such that the depth in the test section was 32 cm. During all experiments, the two centrifugal pumps responsible for recirculating the water in the channel were run at approximately 206 RPM. This resulted in the flow having a freestream velocity of  $U_\infty = 5.3$  cm/s.

The flat plate apparatus, shown in figure 3.1, was positioned horizontally at a zero angle of attack in the channel and with the bottom surface at a depth of 12 cm below the free surface of the water. The leading edge of the flat plate was located 2.9 m downstream of the test section entrance. The flat plate had dimensions of 1.18 m  $\times$  0.62 m  $\times$  15.9 mm ( $L \times W \times T$ ) in the streamwise, spanwise, and wall-normal directions, respectively. An optimized leading-edge profile developed by Hanson and Buckley (2012) was used for the flat plate to ensure a laminar boundary layer would form on the bottom surface. Additionally, the trailing edge of the flat plate tapers down to a thickness of 2 mm to prevent large-scale vortex shedding from this location. A rectangular cut-out in the plate begins 27 cm downstream of the leading-edge and allows for an insert containing the active deformable surface and a spherical cap element to be added to the apparatus. The purpose of the spherical cap was to disturb the laminar boundary layer and generate the periodic velocity fluctuations that were subsequently targeted by reactive control. Detailed drawings of the flat plate apparatus are provided in appendix A.

With consideration of the work of Acarlar and Smith (1987) into similar wake flows, a spherical cap with a height of  $h = 12$  mm and a base diameter of 28 mm was selected for disrupting the boundary layer. The Reynolds number of the spherical cap based on its height is  $Re_h = 635$ . From Acarlar and Smith (1987), this spherical cap was anticipated to have a Strouhal number in the range of  $St_u \approx 0.2 - 0.25$ . The spherical cap was centered  $l = 28.5$  cm downstream of the leading edge. Acarlar and Smith (1987) indicates that the streamwise position of the spherical cap relative to the leading edge is not critical given the low  $Re_h$ . Consequently, the position of the spherical cap was chosen due to the approximate equivalence of the boundary layer thickness and  $h$  at the selected location. Additionally, at this location the Reynolds number of flow based on  $l$  and  $U_\infty$  is  $Re_l \approx 15,000$ . This indicates that the flow should be laminar leading up to the spherical cap.

As is visible in figure 3.1, a Cartesian coordinate system for the flow is defined at the center of the spherical cap element and at the wall. The streamwise, wall-normal, and spanwise directions of the flow are specified by  $x$ ,  $y$ , and  $z$ , respectively. The corresponding flow velocity components are given by  $U$ ,  $V$ , and  $W$ , and the fluctuating velocity components are given by  $u$ ,  $v$ , and  $w$ . This coordinate system will be used for the remainder of this thesis.

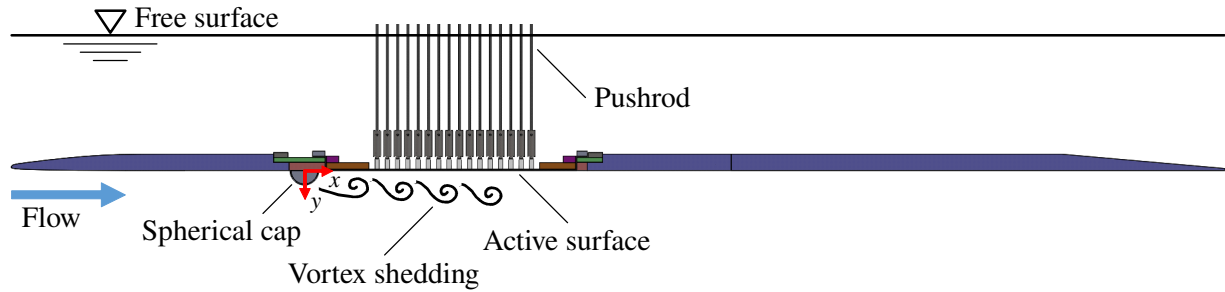


Figure 3.1: Schematic of flat plate apparatus showing the spherical cap and the active surface used for reactive control experimentation.

Prior to the completion of any reactive control experiments, the flow on the bottom surface of the flat plate in the absence of the spherical cap was evaluated using the PIV system described in chapter 3.3. As shown by figure 3.2, good agreement was observed between the measured boundary layer profile and the Blasius boundary layer profile. The agreement between the experimental and the Blasius profiles indicates that the desired laminar boundary layer was indeed obtained on the bottom surface of the flat plate. This was an important result for ensuring that consistent and coherent vortices could be generated and subsequently targeted by the reactive control strategies.

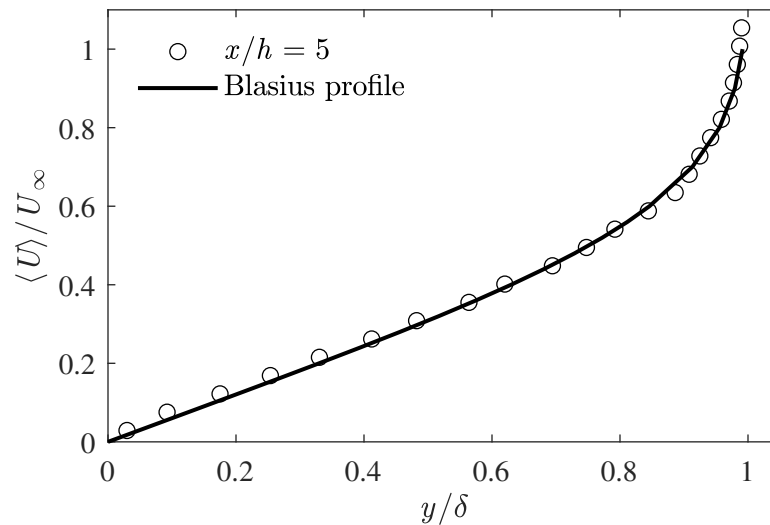


Figure 3.2: Boundary layer profile of the flat plate apparatus in the absence of the spherical cap overlaid with Blasius boundary layer profile.

## 3.2 Active deformable surface

An actively deformable surface composed of sixteen independent actuation locations that can be displaced in the wall-normal direction was developed to serve as the actuator for the AFC system. For readability, it will be referred to as the “active surface” from this point forward. As is visible in figure 3.3(a), the surface that is in contact with the flow is composed of a 1.6-mm-thick silicone rubber sheet that has been stretched such that it is flush with the bottom surface of the flat plate. The rubber sheet replaces an area of the lower flat plate surface with dimensions of  $\Delta x \times \Delta z = 245 \times 60 \text{ mm}^2$ . Adhered to the topside of the rubber surface are sixteen actuator feet that each control one of the independent actuation locations. The actuator feet have dimensions of  $\Delta x \times \Delta z = 4 \times 10 \text{ mm}^2$  and are centered about  $z = 0$ . In the streamwise dimension, the first actuator foot is centered at  $x/h = 5.3$  and subsequent feet are placed with a center-to-center spacing of 10 mm ( $0.83h$ ). Consequently, the sixteenth and final actuator foot is centered at  $x/h = 17.8$ . As is further visible in figure 3.3, each actuator foot is connected by a 2-mm-diameter stainless-steel pushrod to a 20-mm-long servo arm mounted on a high-speed digital servo motor (Savox SH-1290MG). Each servo motor can oscillate the connected actuator foot at frequencies up to 10 Hz, depending on amplitude. This corresponds to a Strouhal number of 2.3 for the actuators, where  $h$  has been used as the characteristic length. As well, the absolute maximum amplitude of the surface was limited to  $\pm 7.2 \text{ mm}$  for all experiments to prevent the surface from entering the FOV of the RT-PIV system (FOV2 in figure 3.3(a)).

As is visible in figure 3.3(b), the pushrods each pass through holes in two nylon guide plates. These guide plates provide additional support to the flexible pushrods and constrain the bottoms of the pushrods to only allow movement of the actuator feet in the  $y$ -direction. As is also shown by figure 3.3(b), an aluminum mounting plate acts as the primary structural element of the active surface assembly. It was secured above the water flume and held the servo motor array securely in place above the flat plate.

As highlighted by figure 3.4, the rotational displacement of the servo arms is converted to linear displacement of the actuator feet using the relation  $y_a = r \times \sin(\theta)$ , where  $y_a$  is the actuator foot displacement,  $r$  is the servo arm length, and  $\theta$  is the angle of the servo arm relative to horizontal. In

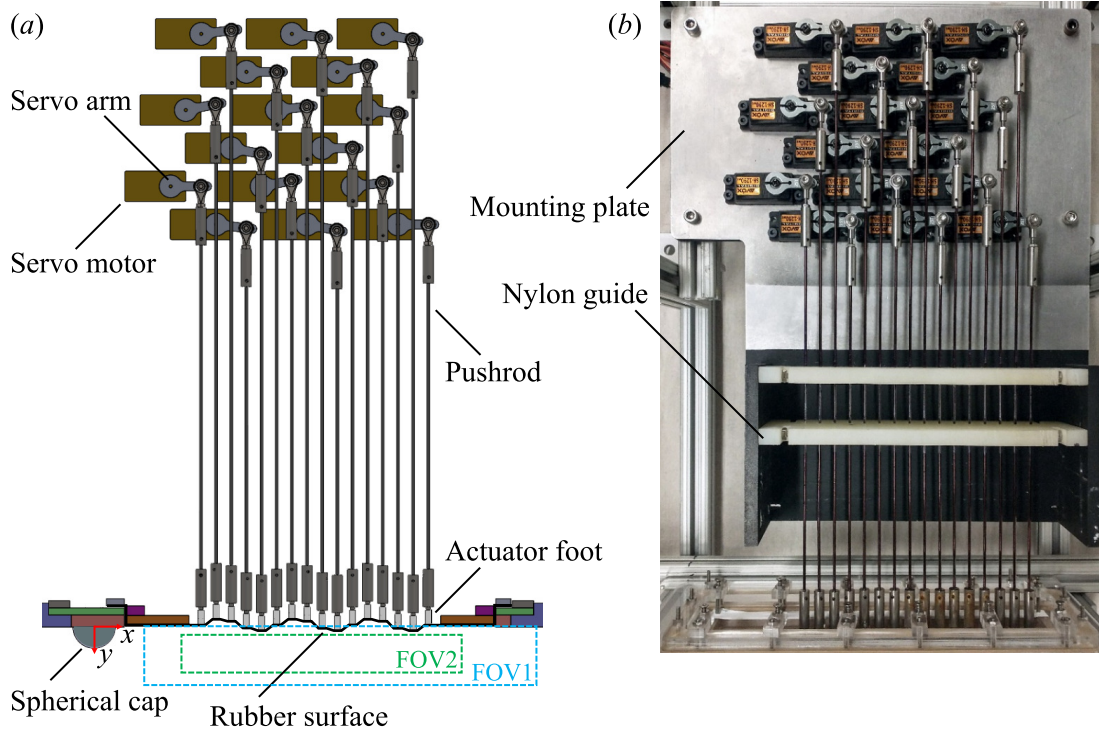


Figure 3.3: (a) Schematic of the active surface mounted in the flat plate. The field of view of the offline PIV and RT-PIV systems are indicated by FOV1 and FOV2 in (a), respectively. (b) Photograph of the active surface assembly showing the mounting plate and nylon guides that hold the servo motors and support the flexible pushrods, respectively.

reality, the left and right sides of the above relation are only approximately equal. This is because the top of the pushrod sees both the desired vertical displacement and a small unwanted horizontal displacement as the servo arm rotates. Given the relatively small angular range of the servo arm ( $|\theta| \leq 21$  degrees) and the length of the pushrods ( $\geq 220$  mm), the error resulting from the small horizontal displacement of the upper end of the pushrods is insignificant for the purposes of this work.

Control of the servo motors was achieved using a Speedgoat real-time target machine (Performance model) with a 16-bit input/output module (model IO135). This system generates and feeds an analog voltage signal for each of the sixteen servo motors to two Teensy 3.2 boards. The Teensy boards read the voltages of the analog signals and output pulse width modulation (PWM) signals to control each of the servo motors. Direct control of the servos from the IO135 module was not

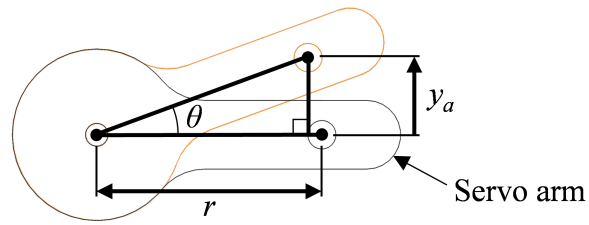


Figure 3.4: Schematic of servo arm highlighting the relation between rotation of the arm and linear motion of the pushrod and actuator foot connected to the end of the servo arm.

possible as it could not produce sixteen independent PWM signals with sufficient resolution to smoothly control the servo motors.

The active surface is capable of approximating a variety of waveforms. Figure 3.5 shows a schematic and photograph of the active surface approximating a sine wave and highlights the discrepancies between the active surface and the waveform it is approximating. According to Nyquist's sampling theorem, the waveforms represented by the surface can have a minimum wavelength of  $\lambda = 20$  mm. There is no specific maximum wavelength, however, for  $\lambda > 150$  mm the active surface will not be able to represent an entire wavelength.

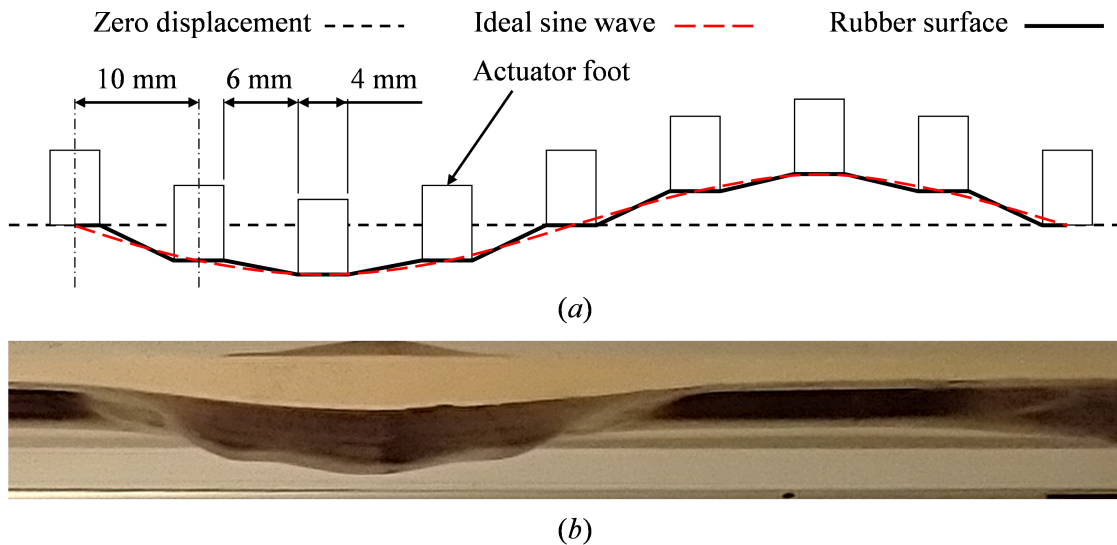


Figure 3.5: (a) schematic and (b) photograph of the active surface approximating a sine wave with an amplitude of 4 mm.

The displacement and response time of the active surface is evaluated by comparing the actual displacement of the surface with the displacement specified by the control signal as shown in figure 3.6. The actual displacements were extracted from images of the active surface captured by the offline PIV system. Since negative displacements were not visible in the PIV images a control signal with positive displacements is evaluated here. As is demonstrated by figure 3.6, the actuator follows the control signal well. The actuator displacements are slightly damped relative to those specified by the control signal. The average displacement extracted from PIV images is approximately 80% of that calculated from the control signal. This level of damping is consistent across different actuators of the active surface and over different cases of reactive control. The primary contributor to the observed damping is attributed to the resistance applied by stretching the rubber surface. Additionally, the actuators lagged their control signal by approximately 40 ms. This delay is mainly attributed to the reaction time of the actuators and the analog-to-digital signal conversion completed by the Teensy 3.2 boards.

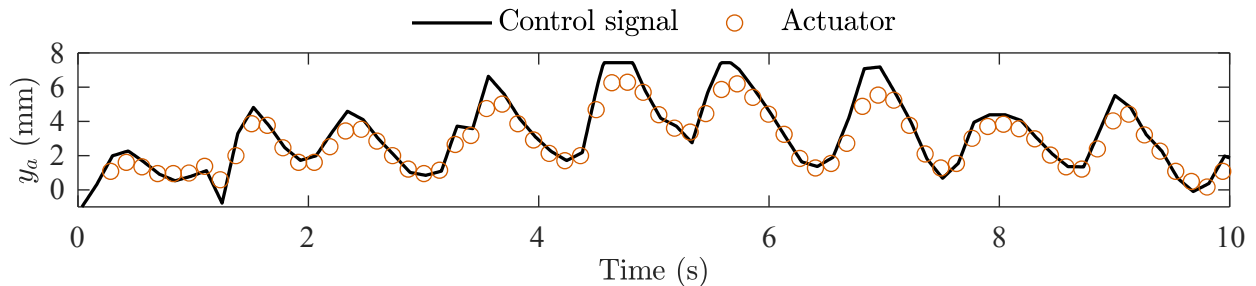


Figure 3.6: Timeseries comparison of a single actuator’s tracking of a sample control signal.

### 3.3 Offline PIV

Planar PIV was used to measure the velocity field during all experiments. These velocity field measurements were subsequently used to evaluate the impact of reactive control on the wake flow behind the spherical cap. Figure 3.7 shows a photograph of the offline PIV system that was used. Two cameras (LaVision GmbH ImagerProX4M) were used with their FOVs stitched together into a single FOV, shown by FOV1 in figure 3.3(a). Each camera features a  $2048 \times 2048$ -pixel monochrome CCD sensor with  $7.4 \times 7.4 \mu\text{m}^2$  pixels and 14-bit resolution. To increase the camera frame rate and

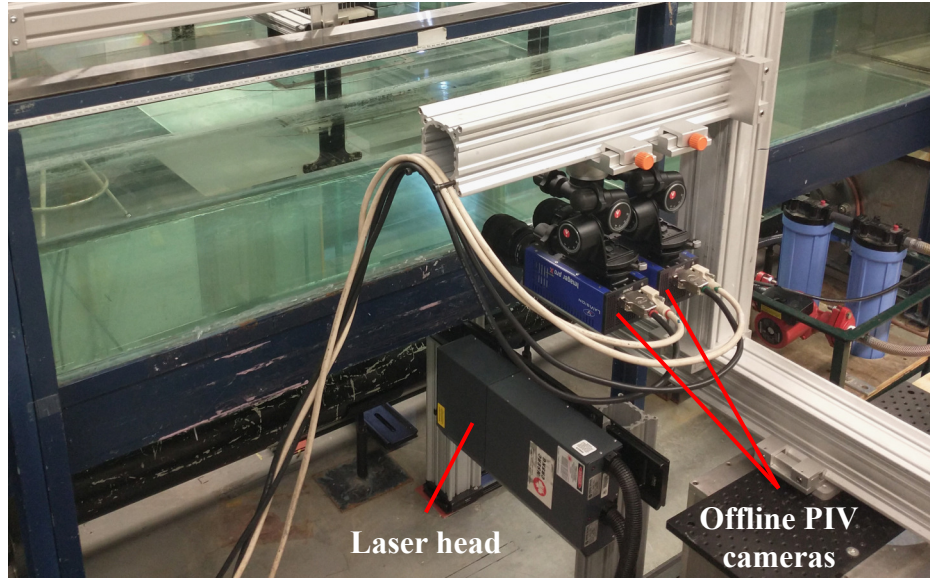


Figure 3.7: Photograph of the offline PIV system used to measure the velocity field above the active surface during reactive control experiments.

eliminate excess data, the camera sensors were cropped to a size of  $2048 \times 625$ -pixels for all sets. Each camera was fitted with a 60-mm lens (Nikon AF Micro Nikkor) with an aperture setting of  $f/4$ . The usable part of the resulting stitched FOV had dimensions of  $\Delta x \times \Delta y = 208 \times 39 \text{ mm}^2$  and a spatial resolution of  $65.5\text{-}\mu\text{m}/\text{pixel}$ . The leading edge of FOV1 was located at  $x/h = 2.7$ . As well, FOV1 was located at the center of the deformable surface in the spanwise direction ( $z = 0$ ). The seeding particles added to the water flow were  $2\text{-}\mu\text{m}$  silver-coated glass spheres (Potters Industries Conduct-O-Fil SG02S40).

FOV1 was illuminated by a dual cavity Nd: YAG laser (New Wave Research Gemini PIV). Each cavity operates independently and can produce laser pulses with an energy of up to 90 mJ per pulse and at a maximum rate of 30 Hz. The laser beam was shaped into a  $\sim 1\text{-mm}$ -thick laser sheet projected upwards through the bottom of the water flume and aligned with the  $x - y$  plane.

The offline PIV system was triggered externally using a delay/pulse generator (Berkeley Nucleonics Corporation model 575). The frame-straddling technique with a laser pulse delay of 16 ms was used to record double-frame images at a rate of 7.35 Hz. For all data sets, the offline PIV system was used to capture 1500 image pairs which corresponds to 204 seconds of data collection

for each set.

Processing of the acquired images was completed using DaVis 8.4.0 (La Vision GmbH). A multi-pass algorithm was used to compute the PIV vector fields. The final processing pass used  $32 \times 32$ -pixel ( $2.1 \times 2.1 \text{ mm}^2$ ) Gaussian-weighted interrogation windows (IW) with 75% overlap. Lastly, the vector fields from each camera were then stitched together into a single field.

### 3.4 RT-PIV

The camera for the RT-PIV system was placed on the opposite spanwise side of the water flume from the two cameras for the offline PIV system. This positioning of the RT-PIV camera is shown by the photograph in figure 3.8. Consequently, the RT-PIV and offline PIV cameras imaged opposite sides of the same laser sheet. A Sony XCL-5005 monochrome camera was used for imaging the tracer particles. This camera features a  $2448 \times 2050$ -pixel CCD sensor with  $3.45 \times 3.45 \text{ }\mu\text{m}^2$  pixels and 8-bit resolution. The camera was fitted with a 35-mm lens (Nikon AF Nikkor) with an aperture setting of  $f/2.8$ . The digital resolution of the camera was set to  $78\text{-}\mu\text{m}/\text{pixel}$ . During experiments, full frame images were cropped to the desired FOV size of  $2368 \times 320$ -pixels ( $185 \times 25 \text{ mm}^2$ ), shown by FOV2 in figure 3.3(a). FOV2 spanned a range from  $y/h = 0.46 - 2.54$  in the wall-normal direction, and a streamwise range of  $x/h = 4.1 - 19.5$ .

The same delay/pulse generator was used to trigger the RT-PIV and synchronize it with the offline PIV system. However, the Sony XCL-5005 camera recorded sequences of single-frame images with each image having an exposure time of 67 ms and an interframe time of 1 ms. Therefore, this camera was triggered at a rate of 14.7 Hz, which is twice the 7.35 Hz acquisition rate of the double-frame offline PIV system. The RT-PIV system was operated in a frame-straddling mode by considering successive images pairs within the single-frame image sequence. More specifically, the RT-PIV camera was triggered such that the laser pulse for the first image of an image pair occurred 1 ms before the end of the image's exposure time. The second laser pulse, occurring 16 ms later, therefore, occurred 14 ms into the exposure time of the second image. Through this, image pairs with the appropriate timing were produced at the same 7.35 Hz frequency as the offline PIV system. This timing is similar to that shown by the sample RT-PIV timing diagram in figure 2.5.



Figure 3.8: Photograph of the RT-PIV and offline PIV cameras on opposite sides of the water flume.

Images were transmitted as they were captured to a frame grabber (Speedgoat GmbH model IO811) via a Base Camera Link connection. The images were then fed immediately into a PIV algorithm implemented in Simulink Real-Time (MathWorks) and run on the Speedgoat target machine. An image of the PIV algorithm implemented in Simulink can be seen in appendix B. The PIV algorithm used for the RT-PIV system is summarized by the block diagram shown in figure 3.9. The algorithm is a basic single-pass PIV algorithm which analyzed  $64 \times 64$ -pixel IWs with no overlap (one vector per  $5 \times 5$  mm<sup>2</sup>). This results in a vector spacing of 5 mm allowing the IWs to align with the actuators spaced 10 mm apart. Cross-correlation of the IW pairs was conducted using the 2D FFT-CC technique outlined in chapter 2.3.2.2 (see equation 2.3). The peak value of the cross-correlation map for each IW pair was identified and then refined using three-point Gaussian sub-pixel interpolation. Lastly, the refined peak location was converted to  $U$  and  $V$  velocities using the known time step between the images and the camera calibration. The final output of the PIV algorithm was a vector field composed of  $37 \times 5$  velocity vectors in the  $x$  and  $y$  directions, respectively.

The performance of the RT-PIV system is evaluated by comparing snapshots of the instantaneous velocity field from RT-PIV in figures 3.10(a) and (c) with those from the offline PIV system

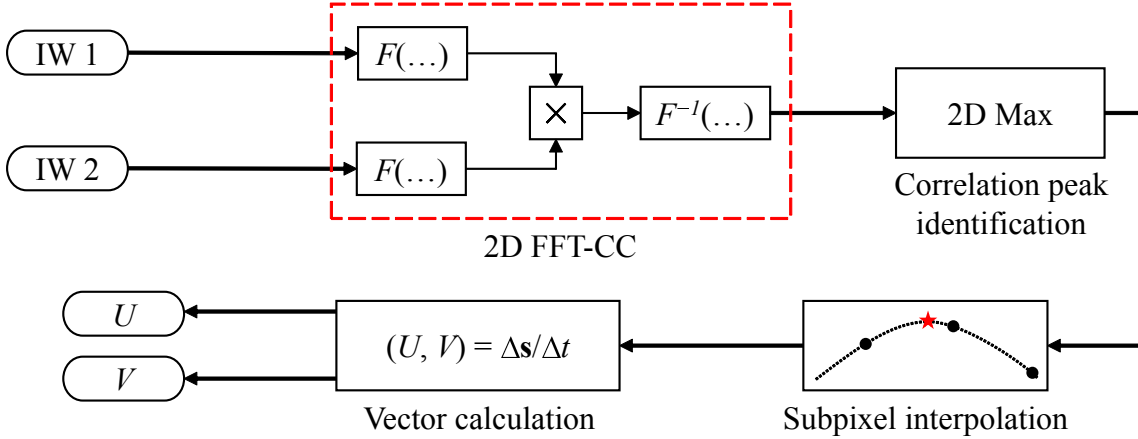


Figure 3.9: Block diagram of PIV algorithm implemented in RT-PIV system.

in figures 3.10(b) and (d). As both systems imaged similar FOVs at the same time instants, this comparison provided a clear indication of the performance of the RT-PIV system versus a commercial PIV system and processing software. Note that the  $y$ -axis in figure 3.10 and all subsequent plots has been flipped relative to the orientation shown in figures 3.1 and 3.3 so that positive  $y$  is in the upward direction. As can be seen in figure 3.10, the RT-PIV measurements have a lower spatial resolution than those from the offline PIV system. This is a result of the offline PIV system employing  $2.1 \times 2.1 \text{ mm}^2$  IWs with 75% overlap, whereas the RT-PIV system used  $5 \times 5 \text{ mm}^2$  IWs with no overlap. Despite this, there is strong agreement between the plots for both the streamwise and wall-normal velocity fields measured by the two systems. Figures 3.10(a) and (b) show similar uplifted regions of low speed fluid that characterize the streamwise velocity field of the periodic flow. As well, figures 3.10(c) and (d) show similar pairs of motions toward and away from the wall.

Figure 3.11 provides an additional comparison of the timeseries of  $U$  and  $V$  velocities measured by the two systems within a  $5 \times 5 \text{ mm}^2$  region of space centered at  $(x, y)/h = (11.2, 1.1)$ . This region corresponds to a single velocity vector measured by the RT-PIV system. For the offline PIV system, the velocity vectors that fell within the selected region were spatially averaged for the comparison. Figure 3.11 shows some minor discrepancies between the RT-PIV and offline PIV measurements. Two likely contributors to these discrepancies are the bit depth of the cameras and the number of PIV processing passes. The RT-PIV camera has a bit depth of only 8-bits whereas

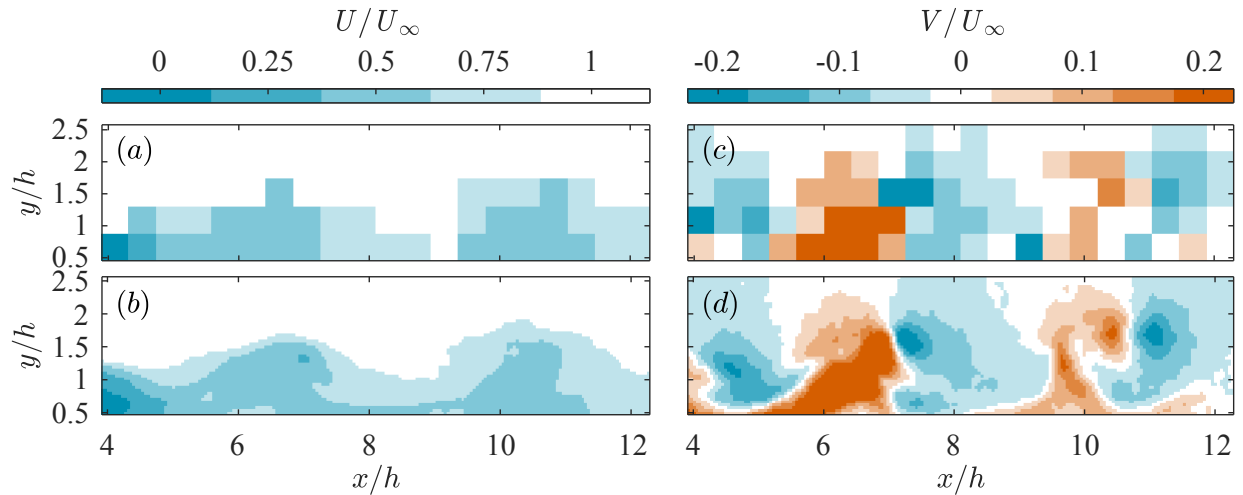


Figure 3.10: Snapshots of streamwise and wall-normal velocity fields measured by (a, c) the RT-PIV system and (b, d) the offline PIV systems for the same time instant. The left-side panels (a, b) show the streamwise velocity component, while the right-side panels (c, d) show the wall-normal velocity component.

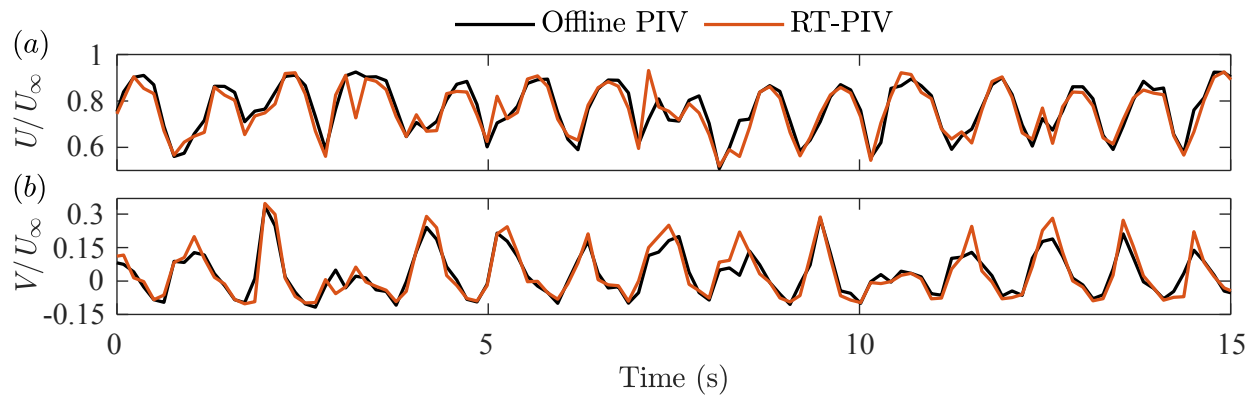


Figure 3.11: Timeseries of velocity measurements from the offline PIV and RT-PIV systems for a  $5 \times 5 \text{ mm}^2$  area centered at  $(x, y)/h = (11.2, 1.1)$ . Due to the higher spatial resolution of the offline PIV system, the vectors within the noted area were spatially averaged.

the offline PIV system employs 14-bit cameras. As well, the RT-PIV system used only a single pass of PIV processing, compared to three passes for the offline PIV system. Both of these factors lead to a lower signal-to-noise ratio for the RT-PIV system and, thus, slightly higher error. Despite the discrepancies, both systems show good agreement in figure 3.11. Overall, figures 3.10 and 3.11 provide confidence that accurate flow measurements were produced by the RT-PIV system. A dominant frequency of  $\sim 1$  Hz is apparent in the time-series of both the streamwise and wall-normal flows.

The latency of the RT-PIV system ( $\Delta t_l$ ) is defined as the time between the measurement instant and when the velocity field computation is completed. Figure 2.5 provides a visualization of the components that contribute to the overall latency of RT-PIV systems and is applicable to the system developed for this thesis. The measurement instant ( $t_0$ ) is defined as the midpoint between the first and second laser pulses. Therefore,  $\Delta t_l$  consists of the remaining exposure time of the image frame, read-out time of the camera, and the time required for velocity computations. Based on the time instants of the laser pulses,  $t_0$  occurs 6 ms into the exposure time of the second image. The remaining exposure time for the second image is 61 ms. Based on the specifications for a Base Camera Link connection and the RT-PIV camera, the image readout time was estimated as  $\sim 60$  ms. Lastly, from the execution time of the Real-time Simulink model containing the PIV algorithm, the PIV processing time was found to approximately equal 44 ms. As such,  $\Delta t_l$  was found to be 165 ms. Over this latency period, the flow structures can have a maximum advection of  $0.73h$  (8.7 mm) based on the freestream velocity.

As is described in more detail in chapter 3.5, each of the sixteen actuators of the active surface reacted to velocity measurements from a single grid point of the RT-PIV vector field that is referred to as a “sensor IW” here. Figure 3.12 shows a schematic of FOV2 relative to the active surface with the sixteen sensor IWs indicated with dotted lines. To counteract the latencies of the active surface and RT-PIV system (40 and 165 ms, respectively), the sensor IW for each actuator was offset upstream of the corresponding actuator foot by a value of  $\Delta x_s$ , as shown in figure 3.12. Considering the combined latency of the active surface and RT-PIV system and the freestream velocity of the flow, three values of  $\Delta x_s/h$  of  $-0.6$ ,  $-0.9$ , and  $-1.2$  were chosen to investigate.

For a structure advecting at the freestream velocity of the flow, these three offsets correspond to actuations that respectively lag, coincide with, and precede the velocity fluctuation detected by the upstream sensor IW. As well, two wall-normal positions of the sensor IWs ( $y_s$ ) were also investigated. Values of  $y_s/h = 1.1$  and  $1.5$  were chosen as these encompassed a range within which peak velocity fluctuations were observed for the unforced flow.

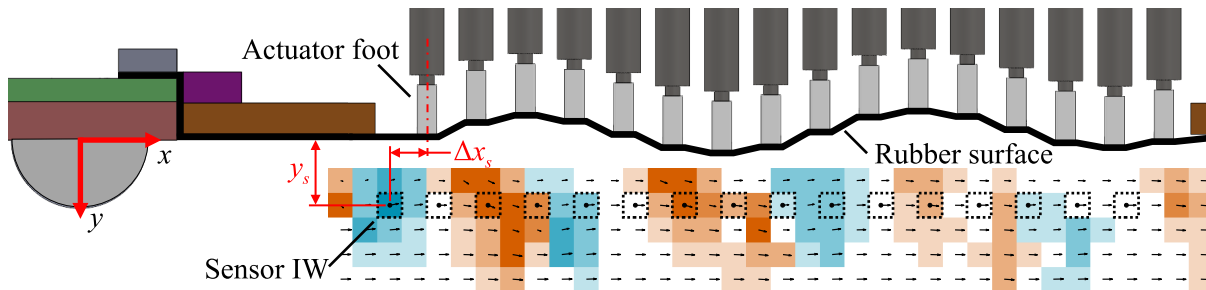


Figure 3.12: Schematic of the active surface relative to FOV2. The velocity field shows contours of wall-normal velocity overlaid with velocity vectors. The dimensions of  $y_s$  and  $\Delta x_s$  noted in the figure correspond to the wall-normal and streamwise offsets of sensor IWs relative to their respective actuator feet.

### 3.5 Reactive control

As noted in chapter 2.2.1, reactive control in wall-bounded flows refers to control where an actuation is applied at the wall in response to the local detection of an oncoming coherent motion (Gad-el Hak, 2000). In the reactive control schemes investigated by this thesis, each of the sixteen actuators respond to velocity measurements from a “sensor IW” location of the RT-PIV measurements. The  $v$ - and  $u$ -control schemes used here are adaptations of the  $v$ - and  $u$ -control strategies of Choi et al. (1994). The  $v$ -control strategy involves measuring the wall-normal velocity close to the wall and deforming the wall at proportional wall-normal velocities. In contrast, the  $u$ -control strategy involves measuring and targeting streamwise velocity fluctuations with wall deformations. Both of the reactive control strategies were realized in Simulink Real-time (MathWorks). Images of the Simulink models for the  $v$ - and  $u$ -control algorithms are provided in appendix B.

### 3.5.1 Control based on wall-normal velocity ( $v$ -control)

The steps of the  $v$ -control algorithm are summarized by the block diagram in figure 3.13. As well, figure 3.14 shows sample timeseries of input, intermediate, and output signals of the  $v$ -control algorithm to demonstrate its effectiveness at moving the active surface at velocities proportional to velocities measured in the flow. The first step of the  $v$ -control algorithm is the application of a simple threshold filter to remove any erroneous measurement of wall-normal velocity ( $V$ ) that does not satisfy  $|V| < 0.5U_\infty$ . Two erroneous measurements are seen at 2.7 and 5.4 seconds of the sample  $V$  signal shown in figure 3.14. The outliers are replaced with a value of zero as this keeps the actuators static until the next valid measurement becomes available. Following this, the mean component of the  $V$  velocity signal was removed by subtracting a running average calculated over a period of 1088 ms (approximately one shedding cycle). This kept the mean value of the input  $V$  signal close to zero. The “Filtered  $V$ ” in figure 3.14 shows the input  $V$  signal after the application of the threshold filter and running average subtraction. The filtered  $V$  signal was next converted to the angular velocity that the servo arm must be moved at to achieve the desired wall velocity. This was done using the relation between the angle of the servo arm and the displacement of the actuator foot noted in chapter 3.2. Following this, the angular velocity signal was up sampled by a factor of ten to allow for micro-stepping of the servo motors in a manner that approximates motion at the desired velocity.

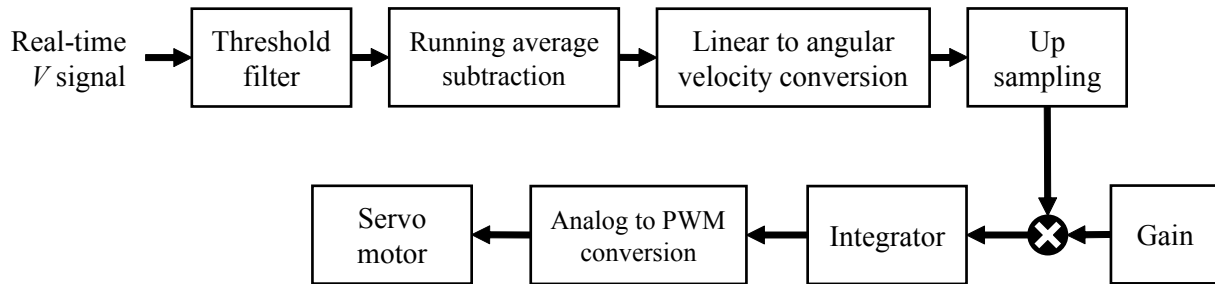


Figure 3.13: Block diagram summarizing steps of the  $v$ -control algorithm.

The signal was next multiplied by a gain value. Six gain values of  $\pm 0.5$ ,  $\pm 1$ , and  $\pm 1.5$  are investigated. The sign of the gain value specifies whether actuators move in the same or an opposing

direction to the measured fluid motion. Negative gain values correspond to opposing actuations similar to the  $v$ -control scheme proposed by Choi et al. (1994). The positive gain cases are included in this investigation to evaluate how compliant actuations impact the flow. A gain magnitude of one corresponds to  $v$ -control that attempts to move the active surface at speeds equal to the measured wall-normal flow speed and gain magnitudes of 0.5 and 1.5 correspond to actuation speeds that are slower and faster than the measured wall-normal velocities, respectively. The signal is next sent through a discrete time integrator. This step converts the angular velocity signal to the angular position signal of the servo arm. The discrete time integrator was the reason for inclusion of the running average subtraction from the input  $V$  signal. If this was not done, the mean component of the  $V$  signal would quickly accumulate during integration of the velocity signal and result in actuators becoming saturated. To evaluate the output signal of the  $v$ -control algorithm with respect to the input  $V$  signal from the real-time PIV, the time-derivative of the  $v$ -control output, i.e.  $dy_a/dt$ , is shown in figure 3.14. The “sample and hold” appearance of the signal is due to each actuator maintaining a constant velocity in the time period between velocity measurements. Lastly, the integrated velocity signal is converted to a PWM signal for controlling the actuators using a manufacturer provided calibration for the servo motors.

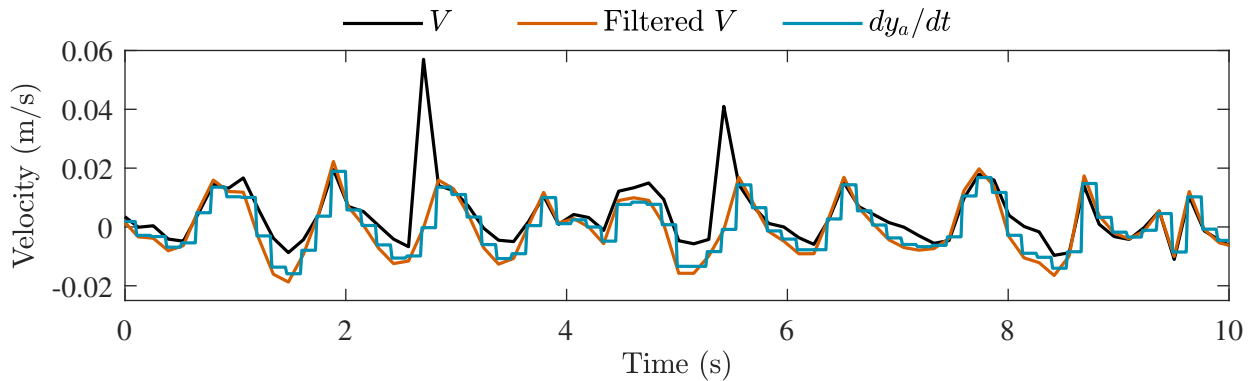


Figure 3.14: Sample timeseries outlining signal processing steps within the  $v$ -control algorithm with a gain of 1.  $V$  is the wall-normal velocity measurement from the RT-PIV system that is input to the  $v$ -control algorithm; “filtered  $V$ ” shows  $V$  after application of the threshold filter and subtraction of a sliding average; and  $dy_a/dt$  is the time-derivative of the output signal obtained from the  $v$ -control algorithm.

### 3.5.2 Control based on streamwise velocity ( $u$ -control)

The intent of the  $u$ -control algorithm is to displace the active surface in the wall-normal direction to generate the desired streamwise velocity fluctuations. Figure 3.15 summarizes the steps of the  $u$ -control algorithm. As well, figure 3.16 shows sample timeseries of input, intermediate, and output signals of the  $u$ -control algorithm to demonstrate its effectiveness at achieving the desired function. The first step of the  $u$ -control algorithm involved converting the real-time  $U$  measurements from the RT-PIV system to fluctuating  $u$  values by subtracting the average velocity of the unforced flow. The average velocity,  $\langle U \rangle$ , was calculated from 2000 velocity field measurements of the unforced flow collected at a rate of 7.35 Hz using the RT-PIV system. The subtraction of a pre-measured average was used because the  $u$ -control algorithm did not require a discrete time integrator and, as such, there was no risk of the actuators becoming saturated due to accumulation of mean components in the  $u$  signal. Following the mean subtraction, a threshold filter was applied to detect values of  $|u| > 0.5U_\infty$ . The outliers were set equal to the most recent valid  $u$  value because this kept actuators stationary until the next valid  $u$  measurement. The  $U$  signal in figure 3.16 shows the input signal to the algorithm and  $u_f$  shows the signal that results after subtraction of the pre-measured average and application of the threshold filter. It is evident that the threshold filter removed an outlier from the input  $U$  signal at 8.7 seconds in figure 3.16.

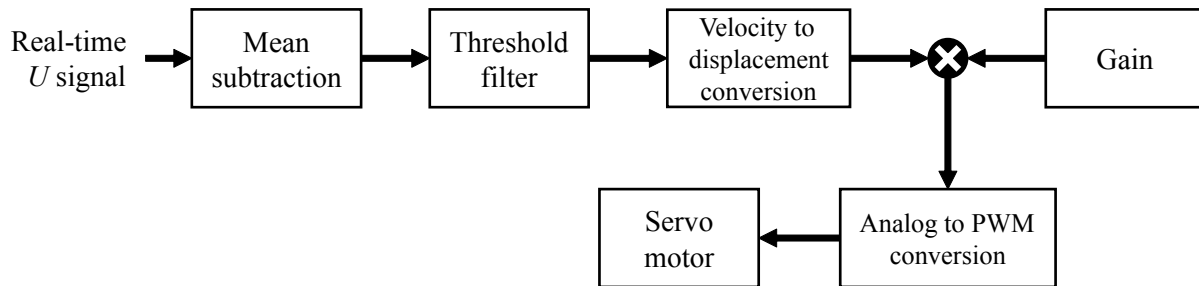


Figure 3.15: Block diagram summarizing steps of the  $u$ -control algorithm.

The  $u_f$  values were then multiplied by a gain value and converted to the desired surface displacement using a linear relation:  $y_a = kG \times u_f$ . Here,  $k$  is a constant equal to  $-0.118$  seconds, and  $G$  is the gain for the control case. The constant  $k$  was determined from open-loop operation of the

active surface in the absence of the spherical cap. The experiments indicated that the strength of streamwise velocity fluctuations produced by the open-loop actuations are linearly proportional to the displacement of the active surface. Based on the measurements, the value of  $k$  was chosen such that the amplitude of actuator displacement was comparable to that seen for  $v$ -control. The direct conversion from velocity to displacement using a linear relation allowed the  $u$ -control algorithm to be designed without requiring the use of a discrete time integrator.

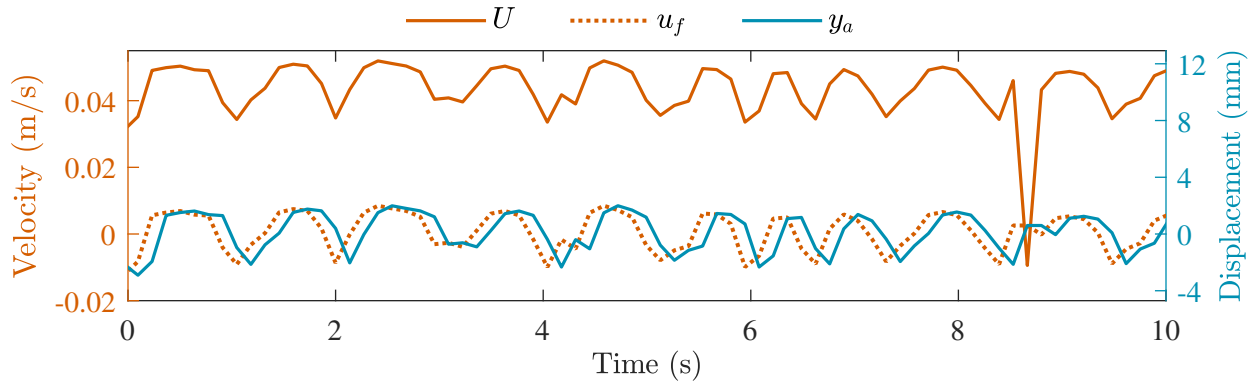


Figure 3.16: Sample timeseries outlining the signal processing within the  $u$ -control algorithm with a gain of  $-1$ . The  $U$  signal is the wall-normal velocity measurement from the RT-PIV system that is input to the  $u$ -control algorithm;  $u_f$  is the threshold filtered fluctuating streamwise velocity signal; and  $y_a$  is the displacement of the active surface at the corresponding actuation location.

As with  $v$ -control, six gain values of  $\pm 0.5$ ,  $\pm 1$ , and  $\pm 1.5$  are investigated. Negative and positive gains correspond to control where streamwise velocity fluctuations induced at the wall are opposing and compliant to the streamwise velocity fluctuations measured in the flow, respectively. Figure 3.16 shows the output  $y_a$  signal of the  $u$ -control algorithm. The displacements shown by  $y_a$  lag  $u_f$  by one sampling period (136 ms). This occurs because actuators were controlled to move to the desired displacement over the time period between velocity measurements. This ensured that actuators moved smoothly between new displacement value. Consequently, as is demonstrated by figure 3.16, the  $u$ -control algorithm was successful at moving the active surface to displacements that were proportional to measured streamwise velocity fluctuations.

# Chapter 4

## Results

This chapter outlines the results of the reactive control investigations carried out for this thesis. The actuation amplitudes and the relation of this to the turbulent kinetic energy (TKE) of the flow is first outlined in chapter 4.1. Following this chapters 4.2 and 4.3 discuss observations from the instantaneous and time-averaged flow fields, respectively. Lastly, chapter 4.4 describes the extent of disruption and suppression of the periodic flow that occurred due to the applied reactive control.

### 4.1 Actuation and flow energy

This chapter describes the actuation amplitudes of the active surface during reactive control. The TKE of the flow (i.e.,  $u^2 + v^2$ ) and its relation to actuation amplitude is then discussed. Quantities with a subscript “u” (e.g.,  $V_u$ ) in this and subsequent chapters denote that they are quantities of the unforced flow.

Figure 4.1 shows the average standard deviation displacement of the active surface ( $\sigma_y$ ) calculated from the control signals for the actuators of the active surface during reactive control with the different gains and sensor locations that are investigated. It illustrates that both  $v$ - and  $u$ -control exhibit similar actuation amplitudes at the different gain magnitudes. This was done intentionally during the design of the  $u$ -control algorithm to allow for easier comparison between the two control strategies. As would be expected, gain magnitude appears to have a relatively monotonous impact on  $\sigma_y$ . As well, there are some small differences that are evident in cases with the same gain magnitude but opposite gain signs. These are encouraging of the idea that the opposing and compliant

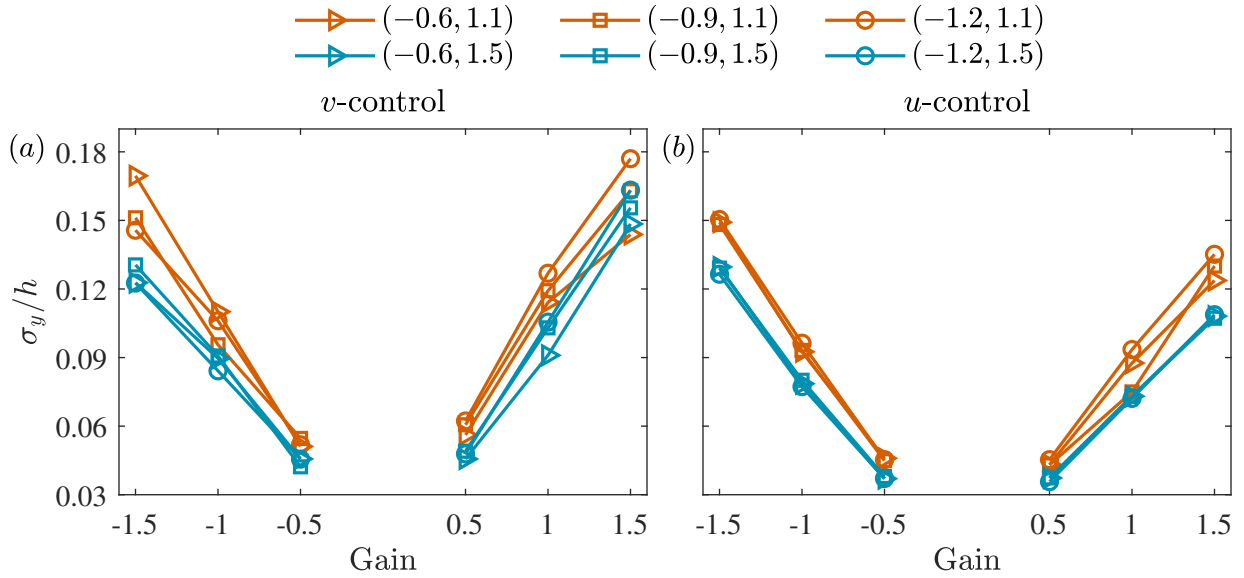


Figure 4.1: Average standard deviation displacement across the active surface ( $\sigma_y$ ) for (a)  $v$ -control and (b)  $u$ -control with different gains and sensor locations. The numbers in brackets in the legend indicate  $(\Delta x_s, y_s)/h$  for each case.

actuators for  $v$ - and  $u$ -control were impacting the flow in different manners.

Another notable trend visible in figure 4.1 is the effect of different  $y_s$  values for both  $v$ - and  $u$ -control. Control cases with  $y_s/h = 1.1$  generally show larger  $\sigma_y$  values compared to cases with  $y_s/h = 1.5$ . This is primarily a result of smaller actuation amplitudes of the first three to four actuators of the active surface due to peak velocity fluctuations passing below the sensors for these actuators when they are positioned at  $y_s/h = 1.5$ . As well, the value of  $\sigma_y$  has less dependence on  $\Delta x_s$  for cases with  $y_s/h = 1.5$ .

For opposing actuation (negative gain) cases of  $v$ -control, the order of the cases in terms of  $\sigma_y$  changes at each gain value. A similar observation can be made for the compliant actuation (positive gain) cases of  $u$ -control with  $y_s/h = 1.1$ . The changing order of cases in terms of  $\sigma_y$  for these groups of cases indicates that the effect of  $\Delta x_s$  on  $\sigma_y$  changes depending on the gain value. For the compliant actuation (positive gain) cases of  $v$ -control, more upstream sensor positions (larger negative values of  $\Delta x_s$ ) lead to larger  $\sigma_y$  values.

Figure 4.2 demonstrates the impacts of reactive control on the TKE of the flow ( $E_t$ ). The  $E_t$  values are calculated from the offline PIV data and are normalized by the TKE of the unforced

flow ( $E_{t,u}$ ). Consequently, cases in figure 4.2 with  $E_t/E_{t,u} < 1$  indicate that the energy added to the flow as a result of the reactive control is less than the kinetic energy that is reduced from other areas of the flow. Reducing the energy of the flow is desirable as it suggests that the reactive control successfully attenuated energetic motions in the flow without adding excess energy elsewhere.

From figure 4.2 it is evident that increasing gain magnitude is predominantly associated with increasing  $E_t$ . This indicates that larger actuations add more kinetic energy to the flow without necessarily achieving better attenuation of energetic motions within the flow. With regards to  $v$ -control, most cases with negative gain values have a value of  $E_t/E_{t,u}$  close to or less than one. This indicates that these cases added less or an equivalent amount of kinetic energy to the flow as compared to amount that they reduced from the flow. The  $v$ -control cases with gains of  $-1.5$  and  $y_s/h = 1.1$  are the exception with TKEs well above that of the unforced flow. This result agrees with Chung and Talha (2011) who found that applying actuations stronger than measured wall-normal velocity fluctuations led to much poorer performance of opposing  $v$ -control. The positive gain cases of  $v$ -control demonstrate trends in  $E_t$  that appear similar to those of  $\sigma_y$  shown by figure 4.1. As such, for these cases the value of  $E_t$  seems closely related to the amplitude of actuations. Comparing  $v$ -control cases with positive and negative gains demonstrates that the opposing actuations generally resulted in lower values of  $E_t$  compared to compliant actuations. The lowest  $E_t$  value for  $v$ -control is  $0.87E_{t,u}$  and occurs for a case with a gain of  $-0.5$  and  $(\Delta x_s, y_s)/h = (-0.9, 1.5)$ .

The opposing actuation  $u$ -control cases demonstrate trends in  $E_t$  that appear similar to those of  $\sigma_y$  shown by figure 4.1. Larger  $\sigma_y$  values correspond with higher  $E_t$  values. The positive gain cases of  $u$ -control also appear to show trends in  $E_t$  that correlate with actuation amplitude, although to a lesser extent than the negative gain cases. The exceptions to this are the three positive gain cases with  $y_s/h = 1.5$  and a gain of  $1.5$ . These cases converge on a value of  $E_t/E_{t,u} \approx 1$ . Additionally, several cases of  $u$ -control, both with positive and negative gains, lowered the TKE of the flow below that of the unforced flow. A minimum  $E_t$  value of  $0.88E_{t,u}$  is achieved for  $u$ -control with a gain of  $-0.5$  and  $(\Delta x_s, y_s)/h = (-0.6, 1.5)$ .

Comparing between the plots for  $v$ - and  $u$ -control, there is some similarity between trends in  $E_t$  for  $v$ -control cases with negative gains and  $u$ -control cases with positive gains. This may

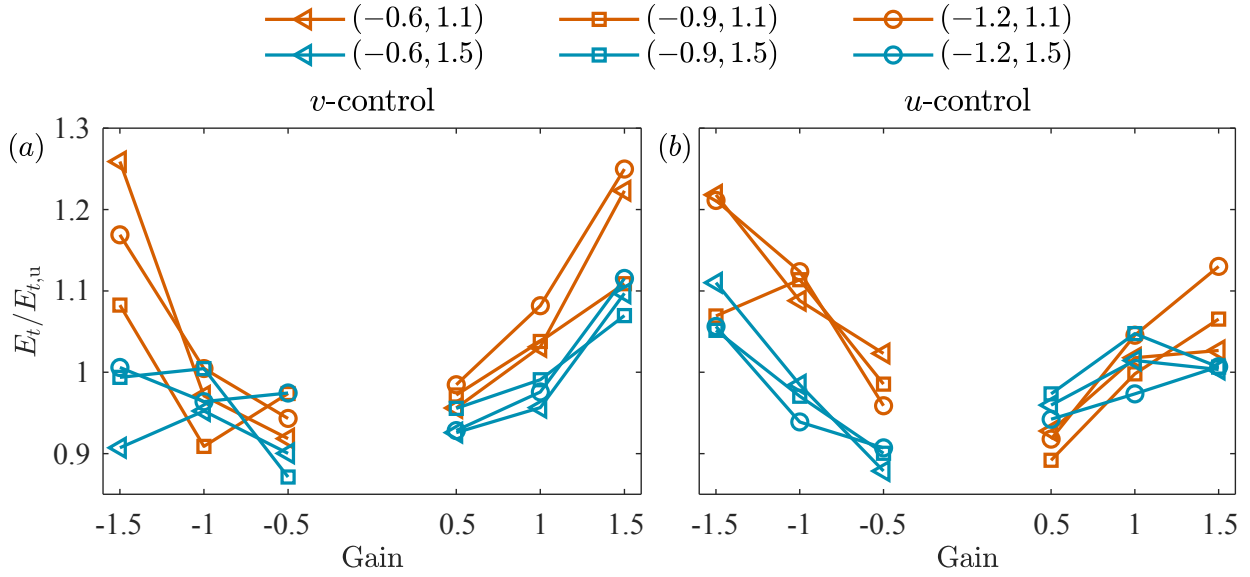


Figure 4.2: Turbulent kinetic energy ( $E_t$ ) for (a) *v*-control and (b) *u*-control cases. The numbers in brackets in the legend indicate  $(\Delta x_s, y_s)/h$  for each case.

indicate that the opposing actuation cases of *v*-control have some similar effects to the compliant actuation cases of *u*-control, and vice versa. This would agree with Choi et al. (1994) who found that drag reductions were achieved with opposing wall-normal actuations and compliant streamwise actuations.

Considering figures 4.1 and 4.2 together, the value of  $\sigma_y$  seems to correlate strongly with  $E_t$  for compliant actuation cases of *v*-control and opposing actuation cases of *u*-control. This indicates that the actuation of the active surface may be generally exciting the flow for these cases. For opposing actuation cases of *v*-control and compliant actuation cases of *u*-control, the impact of the reactive control is less dependent on  $\sigma_y$ .

## 4.2 Instantaneous flow fields

The instantaneous flow is investigated from the offline PIV measurements to evaluate the impact of the different reactive control techniques on the flow. The wake flow behind the spherical cap without any surface deformation is defined as the unforced flow. The unforced flow without any surface deformation is first described in chapter 4.2.1. Impacts of the reactive control techniques are

subsequently described by chapter 4.2.2. A subscript “u” (e.g.,  $U_u$  and  $V_u$ ) is used in the following chapters to denote quantities of the unforced flow.

### 4.2.1 Unforced flow

Figures 4.3(a) and (b) show contours of the instantaneous  $U_u$  and  $V_u$  fields overlaid with vectors of velocity fluctuations,  $(u_u, v_u)$ . The vector fields in figure 4.3 show several spanwise vortices. The first vortex is visible at  $(x, y) \approx (6h, 1.5h)$  and subsequent vortices occur with a streamwise spacing of  $\sim 4h$  (the shedding wavelength) and a height above the wall that gradually increases to  $y/h \approx 2.5$ . Therefore, approximately four actuators fit within this wavelength. As such, the active surface has sufficient spatial resolution to be able to target individual coherent motions within the flow. Additionally, inspection of the frequency spectrum of the unforced flow, highlights that the shedding frequency is  $f_u = 0.9$  Hz. When normalized by  $U_\infty$  and  $h$ , the Strouhal number of the flow is  $St_u = 0.2$ . Consequently,  $St_u$  is much lower than the maximum Strouhal number for the active surface which is 2.3. Consequently, the active surface will be operated well below its maximum capabilities when responding to the periodic motions within the flow.

The  $U_u$  field shows that each vortex results in a region of uplifted low-speed fluid at its upstream edge. As well, in the  $V_u$  field the vortex core is located between an upstream ejection and a downstream sweep motion. The zones of sweep and ejection motions in figure 4.3(b) are inclined with respect to wall with the degree of this incline increasing closer to the wall. This inclination presents some additional challenges to properly timing actuations based on measurements away from the wall. For example, when a sweep motion is detected at  $y/h = 1.5$ , there may actually be an ejection motion in the near-wall region at the same streamwise position. As such, different relative sensor locations allow for investigating the timing of actuations relative to the coherent motions.

Figure 4.3 also shows that the height above the wall of the vortices gradually increases from  $y/h \approx 1$  to 2.5. As a result, ejection and sweep zones stretch gradually away from the wall and attenuate as they advect downstream. Based on investigations by Acarlar and Smith (1987) into similar wake flows, the unforced flow field is the result of a series of hairpin vortices being shed

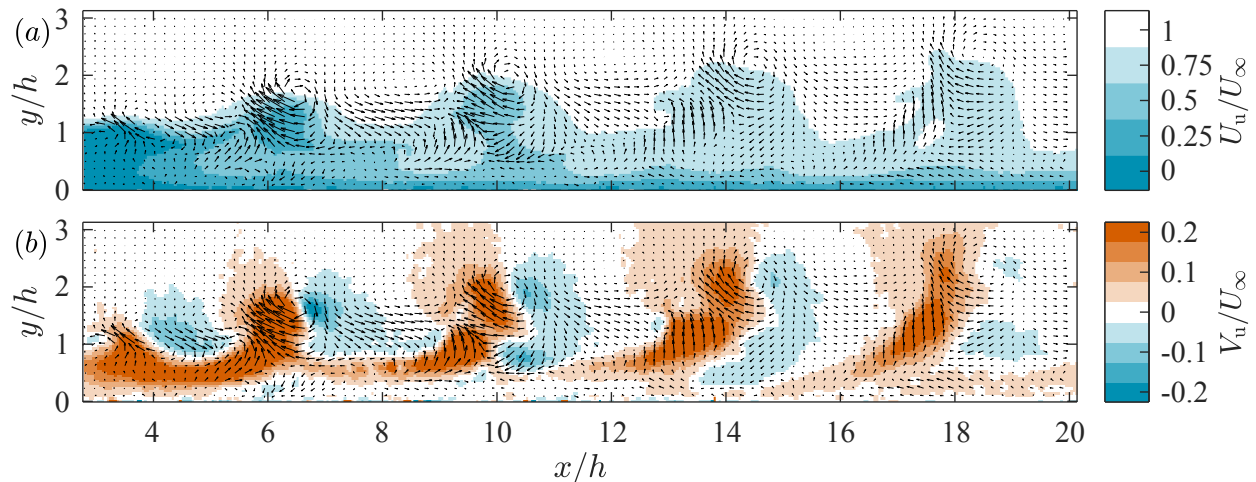


Figure 4.3: Instantaneous (a) streamwise and (b) wall-normal velocity contours of the unforced flow in the wake of the spherical cap overlaid with fluctuating velocity vectors.

from the spherical cap. Consequently, the spanwise vortices evident in figure 4.3 represent the heads of individual hairpin vortices. As well, the inclined shape of the ejection and sweep zones may be explained as a result of the legs of each hairpin vortex extending upstream of the hairpin head. Hairpin vortices are a common coherent structure observed in turbulent wall-bounded flows (Adrian, 2007). As such, this flow field allows for investigation of the impacts of reactive control techniques on coherent structures similar to those found in turbulent wall-bounded flows but with reduced complexity due to their periodicity and coherence.

#### 4.2.2 Impacts of reactive control

The impacts of the reactive  $v$ - and  $u$ -control on the instantaneous flow are significant in many of the investigated control cases; however, the effects are not consistent or easily interpreted simply by viewing the instantaneous fields. Consequently, only a few general conclusions will be discussed based purely on the instantaneous flow field results. More quantitative conclusions on the effects of  $v$ - and  $u$ -control are drawn in subsequent chapters.

Figure 4.4 shows contours of the instantaneous flow fields for  $v$ -control with a gain of  $-1.5$  (opposing actuations). As well, the sensors are centered at  $(\Delta x_s, y_s)/h = (-0.6, 1.1)$ . Note that data close to the wall ( $y/h < 0.5$ ) is excluded from figure 4.4 and all subsequent plots derived from

the reactive control cases because surface deformations did not allow for accurate measurements in this region.

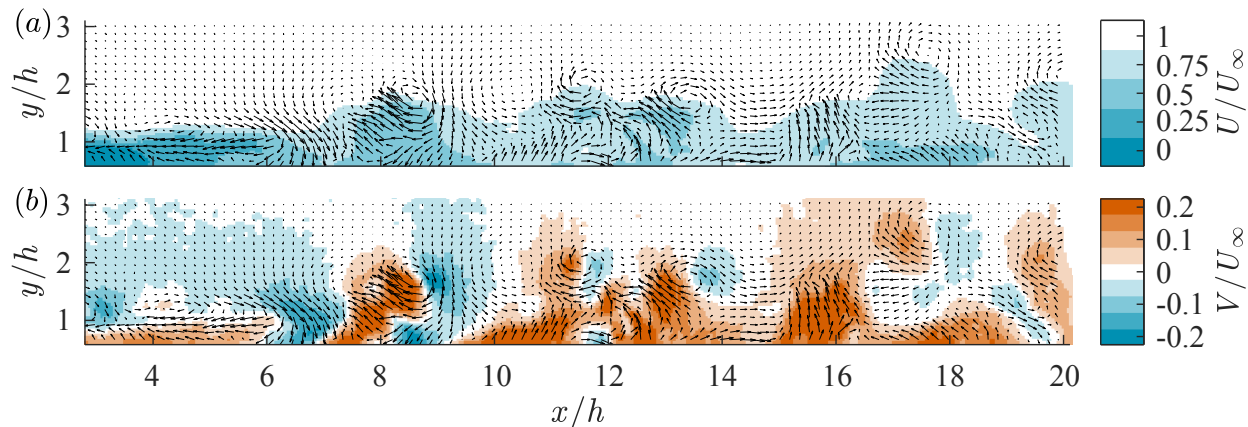


Figure 4.4: Instantaneous (a) streamwise and (b) wall-normal velocity contours overlaid with fluctuating velocity vectors during  $v$ -control with a gain of  $-1.5$  and sensor locations of  $(\Delta x_s, y_s) = (-0.6, 1.1)$ .

As is evident in figure 4.4, the periodicity of the flow field is interrupted and the flow consists of smaller and irregular structures. However, a chaotic pattern of alternating ejections and sweeps still persists in the controlled flow. Relative to the unforced flow, the shape and organization of the ejection and sweep motions is significantly altered as they appear random. As well, the shedding frequency likewise becomes less consistent. This is evident in the closely spaced vortices visible at  $x/h \approx 11.5$  and  $13.5$  in figure 4.4. For all  $v$ -control cases, effects on the spatial organization of the ejection and sweep motions remained visible.

Regarding  $u$ -control, figure 4.5 shows contours of the instantaneous flow fields during  $u$ -control with a gain of  $-1.5$  (opposing actuations) and sensor locations of  $(\Delta x_s, y_s)/h = (-0.6, 1.1)$ . Figure 4.5 shows that the applied  $u$ -control is less disruptive to the periodic flow than the  $v$ -control case shown by figure 4.4. The flow structures exhibit a similar pattern of paired ejection and sweep motions visible in the unforced flow.

However, clear changes to the shapes of the coherent motions could be observed in all the investigated  $u$ -control cases. The controlled flow appears to generally show less lift up of low-speed fluid relative to the unforced flow. In addition, many of the ejection and sweep motions in the

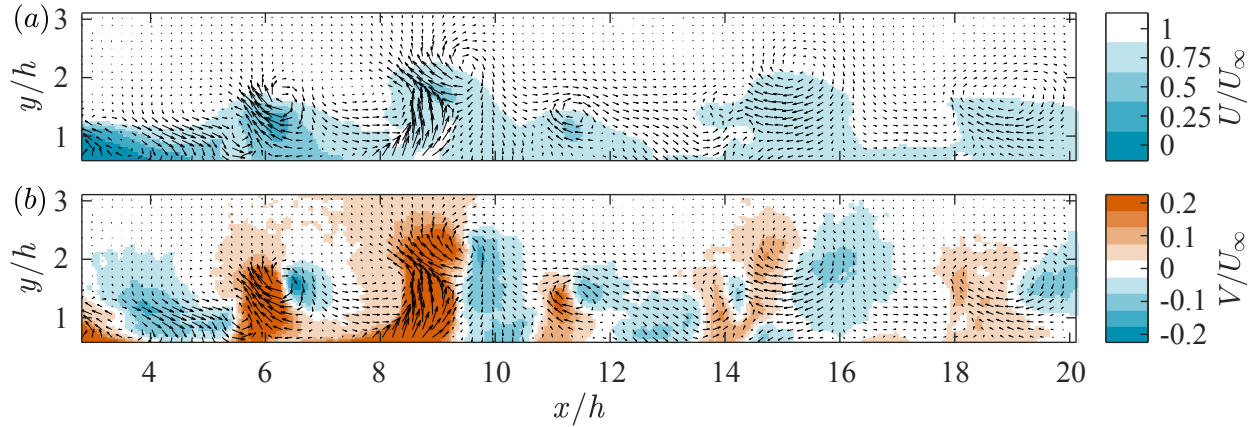


Figure 4.5: Instantaneous (a) streamwise and (b) wall-normal velocity contours overlaid with fluctuating velocity vectors during  $u$ -control with a gain of  $-1.5$  and sensor locations of  $(\Delta x_s, y_s) = (-0.6, 1.1)$ .

flow during  $u$ -control have significantly larger inclination with respect to the wall; the ejection and sweep zones are approximately perpendicular to the wall. This suggests that the applied  $u$ -control affects the flow field, but it does not produce the same degree of disruption of the periodic flow seen in some of the  $v$ -control cases.

### 4.3 Time-averaged flow fields

Mean properties of the flow were subsequently investigated from offline PIV measurements to evaluate the average effects of the reactive control cases. Chapter 4.3.1 first provides an overview of mean properties for the unforced flow. Following this, chapter 4.3.2 provides analysis of the mean flow properties that resulted during the reactive control investigations. In the following discussions,  $\langle \dots \rangle$  denotes an ensemble average.

#### 4.3.1 Unforced flow

Figure 4.6 shows the average velocity fields of the unforced unforced flow along with contours of Reynolds shear stress. The average streamwise flow in figure 4.6(a) shows a small region of reverse flow in the near-wake of the spherical cap up to  $x/h \approx 4$ , as shown by the black contour line. Consequently, the first actuator foot centered at  $x/h = 5.3$  is outside of the reverse flow region.

The average streamwise flow field shows fast recovery of the velocity deficit up to  $x/h \approx 8$ . Beyond this, a more gradual recovery of the velocity deficit is observed.

The average wall-normal flow field shown by figure 4.6(b) exhibits three key regions. There is a single negative region at the upstream edge of figure 4.6(b). This region is associated with fluid being drawn downward in the near-wake of the spherical cap. Below this negative region there is an intense, gradually tapering positive region extending from the upstream edge of figure 4.6(b) to  $x/h \approx 8$ . This region is a result of the spanwise vortices which generate strong ejection motions. As can be observed in figure 10, the region close to the wall up to  $x/h \approx 8$  is dominated by a series of interconnected ejection motions. Past  $x/h \approx 8$ , stretching of the ejection motions into the flow and penetration of sweep motions towards the wall results in an abrupt end to this initial, intense upward motion. The final key region is the region of weak upward motion that extends diagonally in a wide band from the top of the region of intense upward motion to the upper right corner of figure 4.6(b). This region is the cumulative result of the passage of periodic ejection and sweep motions. The positive sign of this region demonstrates that the ejection motions were generally stronger than sweep motions. The decreasing magnitude of the region with increasing streamwise position highlights the gradual attenuation of the vortices. Additionally, the inclination of this positive region with respect to the flow direction demonstrates the stretching of vortices as they advect downstream.

The Reynolds shear stress contour, shown by figure 4.6(c), has two notable regions. The first is the positive region that extends across the entire streamwise range. This positive region is associated with the passage of ejection and sweep motions. The attenuation of this region along its streamwise dimension and its inclination with respect to the flow direction further highlights the weakening and stretching of vortices as they advected downstream. Additionally, this positive region indicates strong production of turbulent kinetic energy (TKE). The second notable region in figure 4.6(c) is the negative region of Reynolds shear stress below the positive region and close to the wall. For  $x/h > 6$ , the gradient  $d\langle U_u \rangle / dy$  is positive across the measured wall-normal range, as seen in the overlaid velocity vectors in figure 4.6(a). As such, this negative Reynolds stress region contributes to the negative production of TKE.

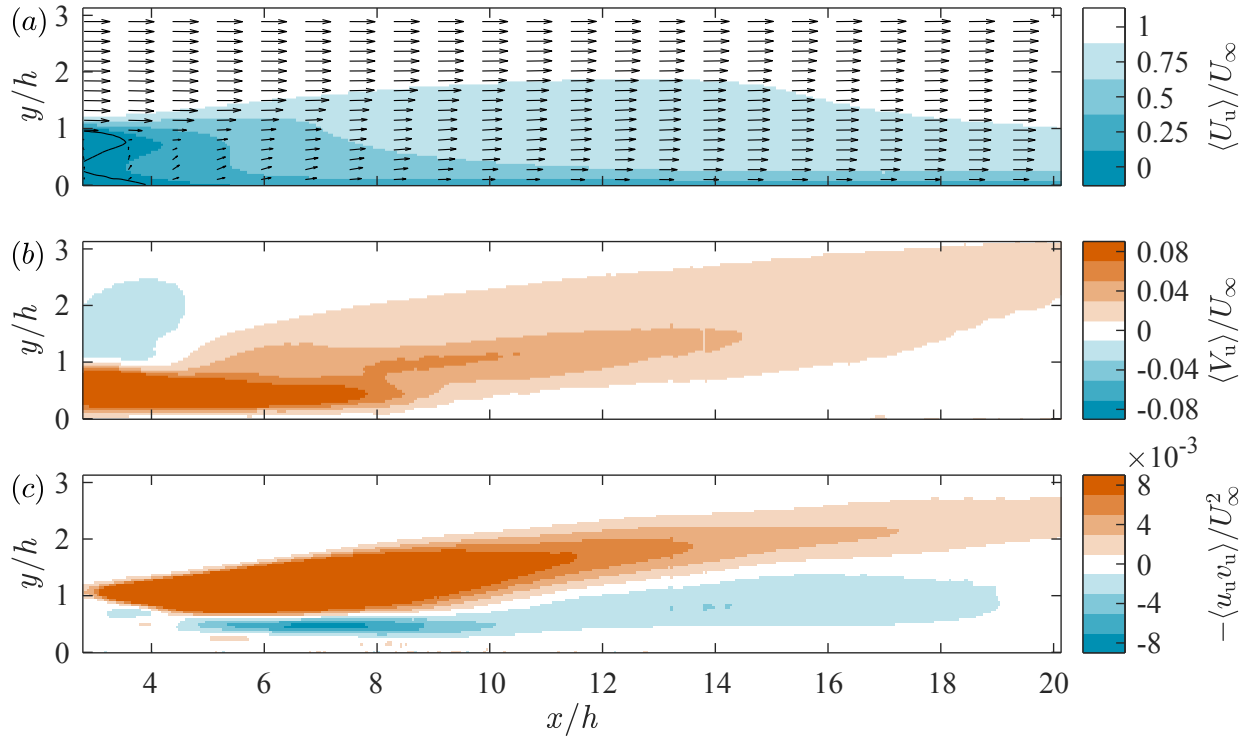


Figure 4.6: (a) Average streamwise velocity, (b) average wall-normal velocity, and (c) Reynolds shear stress contours of the unforced flow. Panel (a) is also overlaid with average velocity vectors and the black line indicates the  $\langle U_u \rangle = 0$  contour.

### 4.3.2 Impacts of reactive control and varied gain

The reactive control investigation involved a parametric study of the impacts of varying the gain and the sensor locations used in the  $v$ - and  $u$ -control algorithms. The impacts of varying gain will first be discussed. As previously outlined, both the  $v$ - and  $u$ -control algorithms included a gain value that specified the strength and direction of actuations relative to the real-time velocity measurements. Negative gains correspond to control intended to oppose the natural fluid motions. These cases were of interest for their relation to the numerous previous works on  $v$ -control with opposing actuations (Choi et al., 1994; Rebbeck and Choi, 2006; Deng et al., 2014). Additionally, positive gain values indicate control intended to apply actuations that were compliant with natural fluid motions. The positive gain cases were included to evaluate the effects of compliant actuations. As well, these cases were also valuable for the comparison they allowed between the effects of opposing and compliant actuations on the flow.

Figure 4.7 shows contour plots of the average streamwise velocity during reactive control relative to the unactuated case (i.e.,  $\langle U \rangle - \langle U_u \rangle$ ). Six tested gains are considered here and the sensors are located at  $(\Delta x_s, y_s)/h = (-0.6, 1.1)$  relative to their respective actuator feet. By subtracting the  $\langle U_u \rangle$  field, the impacts of the reactive control cases were made more evident. In figure 4.7, positive regions within the plots indicate areas where the average streamwise velocity is greater than that of the unforced flow, shown in figure 4.6(a), and vice versa for negative regions.

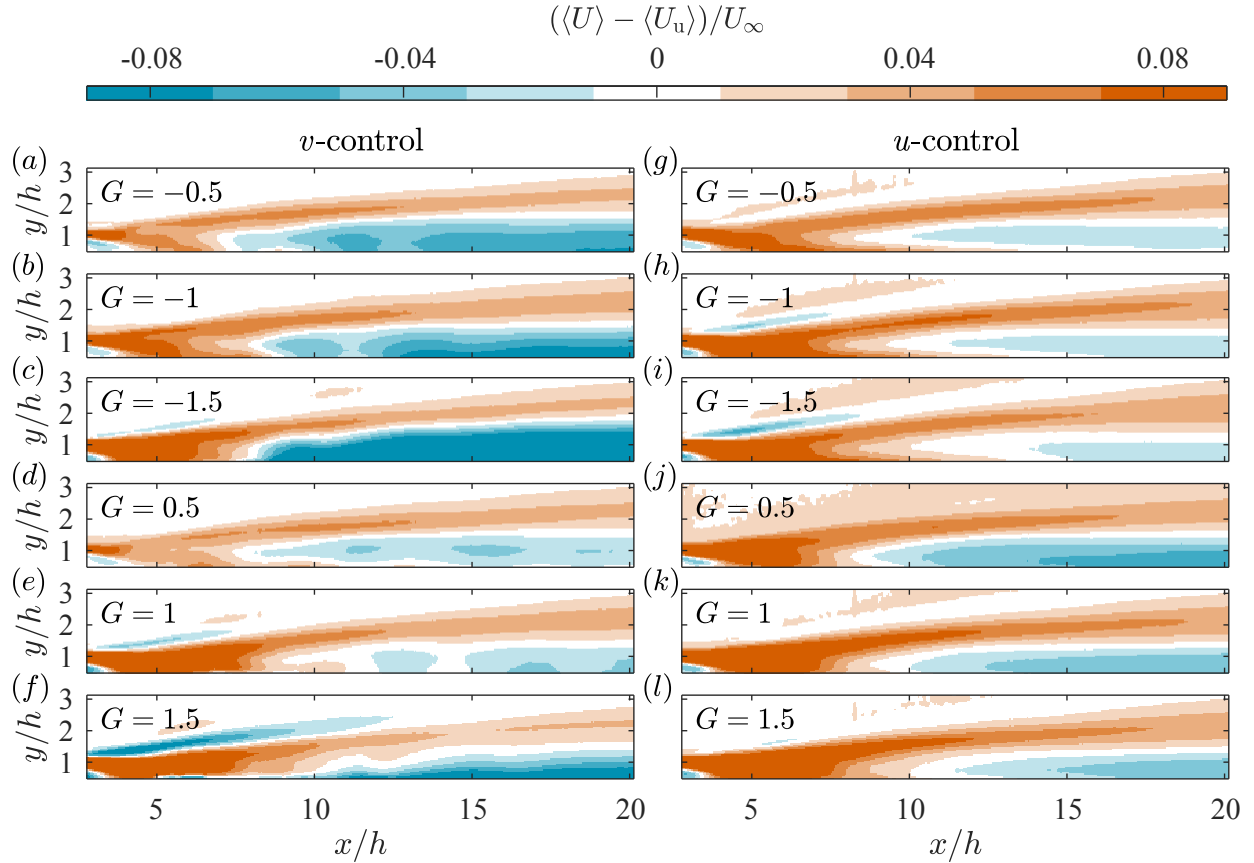


Figure 4.7: Average streamwise velocity field relative to the unforced flow for (a – f)  $v$ -control and (g – l)  $u$ -control cases with  $(\Delta x_s, y_s)/h = (-0.6, 1.1)$  and at all tested gain values.

As evident in figure 4.7, the general features of the relative streamwise velocity fields for the different reactive control cases are similar between  $v$ - and  $u$ -control and across the different gain values. A positive region extends diagonally from the most upstream region near the wall to the most downstream region away from the wall in all plots. This positive region indicates a weaker wake

deficit in the controlled flow and, therefore, an enhancement of the wake recovery. The positive region is most intense and attached to the bottom of the plots in the range of approximately  $x/h < 8$ , though there is significant variation between cases. Downstream of  $x/h \approx 8$ , the positive region is less intense and separated from the bottom of each plot. Consequently, the applied control generally induces an increase in the rate of recovery of the velocity deficit across this positive region. Additionally, the plots in figure 4.7 all feature negative regions encapsulated underneath the positive regions. These negative regions are indicative of larger velocity deficits in the near wall region as a result of the applied control.

The positive and negative regions are both interesting for separate reasons. The positive regions are encouraging from a drag reduction perspective as they indicate that the controlled wake flows are regaining momentum faster in the positive areas than observed in the unforced flow. The negative regions may indicate that sweep motions, which transport high-speed fluid towards the wall, have been somewhat hindered from penetrating towards the wall by the reactive control. Preventing high-speed fluid from reaching the wall and causing high shear rate regions is a key drag reduction mechanism of opposition  $v$ -control (Choi et al., 1994). As such, the negative regions may indicate that, to some extent, the reactive control is producing this drag reduction mechanism.

Regarding the impacts of varying gain, the negative gain cases of  $v$ -control, figures 4.7(*a* – *c*) show a consistent trend of increasing magnitude of the positive regions with increasingly negative gains. The increased magnitude of the positive regions is predominantly observed for  $x/h < 8$ . Consequently, this highlights that  $v$ -control with increasing negative gains is associated with a steady increase to the rate of velocity deficit recovery in the wake flow. The positive gain cases of  $v$ -control, show a relatively large increase in the magnitude of the positive region from a gain of 0.5 to 1, figures 4.7(*d*) and (*e*). However, the cases with gains of 1 and 1.5, figures 4.7(*e*) and (*f*), show relatively similar positive regions. Therefore, within a certain range, increasing positive gains lead to increases to the rate of velocity deficit recovery. However, above a certain gain, these increases appear to be minimal. The increase in the rate of velocity deficit recovery with increasing gain magnitude, in most cases, can be somewhat explained as a result of increasing magnitude of actuations causing vortices to form earlier in the wake by destabilizing the shear layer extending

behind the spherical cap. As such, at higher gain magnitudes the flow is able to regain momentum faster as the earlier formation of vortices promotes earlier entrance of high-speed fluid into the wake.

Additionally, increasing negative gains for  $v$ -control are associated with a steady increase in magnitude of the negative regions close to the wall. This may indicate that the opposing actuations are increasingly inhibiting the penetration of high-speed fluid towards the wall. For positive gain cases, there is less of a consistent trend of the size and magnitude of the negative regions close to the wall. From a gain of 0.5 to 1, there is a decrease in the size and magnitude of the negative region close to the wall. For the case with a gain of 1.5, figure 4.7( $f$ ), the magnitude of the negative region significantly increases again. These observations indicate that the compliant actuations were less capable at inhibiting the motion of high-speed fluid towards the wall.

The  $u$ -control cases, figures 4.7( $g - l$ ), while showing the same general features as the  $v$ -control cases, demonstrate some notable differences. As with  $v$ -control, increasing gain magnitude for  $u$ -control corresponds with significant increases to the magnitude of the positive regions. This may be explained to some degree by the explanation provided for this trend in the  $v$ -control cases. As well, increasing gain magnitudes are associated with decreasing size and magnitude of the negative regions close to the wall. Consequently, for  $u$ -control, increasing gain magnitude enhances the wake recovery and minimizes the reduction of average streamwise velocity close to the wall. The latter of these effects may indicate that  $u$ -control with larger gain magnitudes are less capable at impeding the motion of high-speed fluid towards the wall.

Regarding the impacts of positive versus negative gains for  $u$ -control, the cases with negative gains, figures 4.7( $g - i$ ), show positive regions that are attached to the bottoms of the plots over a significantly larger streamwise range in comparison to cases with equivalent positive gains, figures 4.7( $j - l$ ). As well, the negative gain cases have negative regions close to the wall that are significantly reduced in size and magnitude in comparison to the equivalent positive gain cases. Consequently,  $u$ -control cases with negative gains induced recovery of the velocity deficit over a larger streamwise range while also exhibiting less reduction of the streamwise velocity close to the wall. As well, the greater magnitude of the near-wall negative region for the positive gain cases

seems to agree with the suggestion of Rebbeck and Choi (2006) that compliant streamwise velocity fluctuations induced near the wall aid at inhibiting the penetration of sweep motions toward the wall. The different impacts on the streamwise flow between cases of  $u$ -control with negative and positive gains demonstrates that opposing and compliant actuations have some slightly different effects on the flow. The differences between  $u$ -control cases with equivalent positive and negative gain magnitudes are less evident than those between  $v$ -control cases with equivalent positive and negative gains.

A similar analysis is conducted for the average wall-normal velocity fields of the reactive control cases. Figure 4.8 shows contour plots of the average wall-normal velocity relative to that of the unforced flow during reactive control at the six tested gains and with  $(\Delta x_s, y_s)/h = (-0.6, 1.1)$ . As is shown by figure 4.6(b), the  $\langle V_u \rangle$  field is predominantly positive with the exception of a small negative region attached at the upstream edge of the plot. As such, in the subsequent discussion, negative regions in the plots in figure 4.8 indicate areas of the flow where the average wall-normal velocity away from the wall is reduced in comparison to the unforced flow, and vice versa for positive regions.

There are several common features that exist across all the subplots in figure 4.8, although with some variation in their presentation. One of these common features are the negative regions near the wall and attached to the upstream edge of each plot in figure 4.8. As such, these negative regions are attributed to an upstream shift of the average wall-normal flow field due vortices forming earlier in the wake. This is consistent with the conclusion that the increased velocity deficit recovery seen in the plots in figure 4.7 is also somewhat due to vortices forming earlier in the wake. A second common feature of all the plots in figure 4.8 is a negative region extended in the streamwise dimension and roughly at the center of each plot. These negative regions, which will be referred to as the primary negative regions from this point forward, indicate a reduction to the region of positive  $\langle V \rangle$  in figure 4.6(b) that is associated with the stretching of vortices away from the wall. Consequently, the primary negative regions are attributed to weaker vortices as a result of the applied reactive control. As well, there are two positive regions common to all of the plots in figure 4.8. The first is a positive region above and slightly downstream of the upstream, near-wall negative

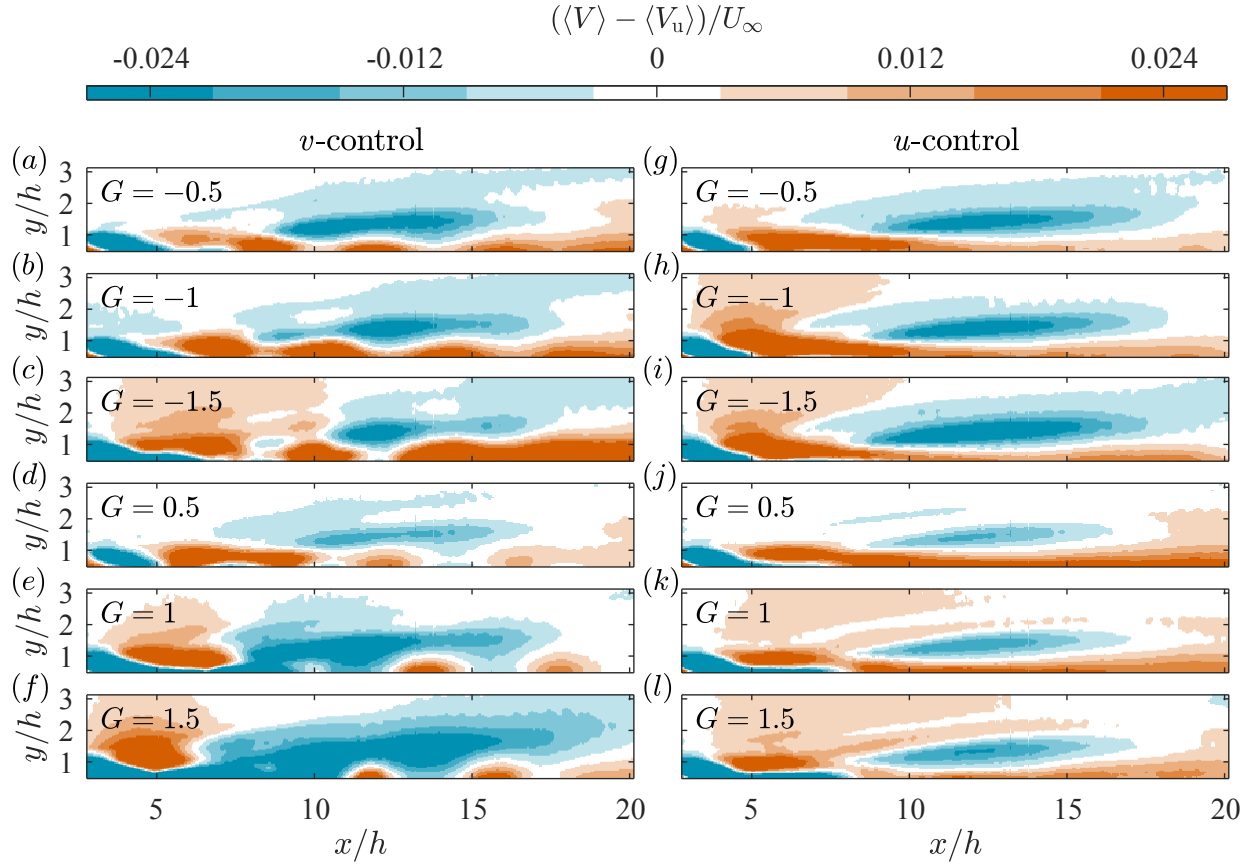


Figure 4.8: Average wall-normal velocity field relative to the unforced flow for (a – f)  $v$ -control and (g – l)  $u$ -control cases with  $(\Delta x_s, y_s)/h = (-0.6, 1.1)$  and at all tested gain values.

regions. As with the upstream, near-wall negative regions, these positive regions are partially due to the upstream shift of the average wall-normal flow. Additionally, all of the plots exhibit positive regions close to the wall, often over a significant streamwise range. These are attributed in part to decreased penetration of sweep motions towards the wall because of the applied control. Some portion of the near-wall positive regions may also be due to the outward deformations of the wall.

With regards to the  $v$ -control cases, there are some clear trends that are visible between cases with gains of the same sign. The negative gain (opposing actuation) cases of  $v$ -control, figures 4.8(a – c), show a trend of decreasing size and magnitude of the primary negative region with increasing gain magnitude. This indicates that at larger negative gains,  $v$ -control is not affecting the strength of the vortices as much as at lower negative gains. As well, there is an increase to the size and

magnitude of the near-wall positive regions for increasing negative gain values. This indicates that the penetration of sweep events towards the wall is inhibited to a greater degree at larger negative gains. This is consistent with the conclusions drawn from the corresponding average streamwise plots shown in figure 4.7.

For the positive gain (compliant actuation) cases, figures 4.8( $d - f$ ), there is a trend of increasing size and magnitude of the primary negative region with increasing gain magnitude. This indicates that  $v$ -control cases with larger positive gains had a greater weakening effect on vortices. As well, the positive gain  $v$ -control cases all exhibit multiple distinct positive regions close to the wall. The near-wall positive regions of the negative gain cases of  $v$ -control likewise show this, although with less distinction between individual positive regions. The cause of this is partially attributed to individual actuators being biased towards outward or inwards deformations during the  $v$ -control case. This resulted due to imperfect removal of the mean component of the wall-normal velocity in the  $v$ -control algorithm. Overall, however, the intermittency and weaker magnitudes of the near-wall positive regions for the positive gain cases of  $v$ -control indicates that these cases were less successful at inhibiting the progress of sweep motions toward the wall.

With regards to  $u$ -control, the negative gain cases, figures 4.8( $g - i$ ), show slightly increasing magnitudes of the primary negative regions with increasing gain magnitude. This indicates that cases of  $u$ -control with larger negative gains weakened vortices more than cases with smaller negative gains. Additionally, figures 4.8( $g - i$ ) all show similar near-wall positive regions. This indicates that all the negative gain values for  $u$ -control similarly inhibited the progress of sweep motions toward the wall. The positive gain cases of  $u$ -control, figures 4.8( $j - l$ ), likewise demonstrate slightly increasing magnitudes of the primary negative regions with increasing gain magnitude. As well, there is a reduction of the near-wall positive region with increasing positive gain. As such, larger positive gains led to slightly weaker vortices and less inhibition of the penetration of sweep motions toward the wall. These observations are consistent with those from the average streamwise flow fields in figure 4.7.

Comparing cases of  $u$ -control with equivalent positive and negative gain magnitudes, the negative gain cases have larger and higher magnitude primary negative regions. Therefore, the oppos-

ing actuation cases had a relatively stronger effect toward weakening the vortices compared to the compliant actuation cases. Additionally, the positive gain cases of  $u$ -control have near-wall positive regions that are moderately larger and higher in magnitude. This indicates that  $u$ -control cases with positive gains are relatively more effective at inhibiting the progress of sweep motions toward the wall.

Lastly, the effect of different gain values on Reynolds shear stress ( $-\langle uv \rangle$ ) is characterized. Figure 4.9 shows shows Reynolds shear stress relative to that of the unforced flow at the the six tested gains and with  $(\Delta x_s, y_s)/h = (-0.6, 1.1)$ . Referring back to figure 4.6(c), the Reynolds shear stress contour for the unforced flow is characterized by a negative region close to the wall that spans most of the streamwise range and a positive region above this that spans the entire streamwise range and is inclined with respect to the flow direction. As with figures 4.7 and 4.8, all the reactive control cases had some overall similar effects on the Reynolds shear stress field. All the plots in figure 4.9 have a positive region attached to the upstream edge. This region is attributed to the earlier formation of vortices in the wake of the spherical cap. As well, all the plots show a negative region inclined with respect to the flow direction that extends across most of the streamwise range. This region indicates that the reactive control generally reduced the positive region of Reynolds shear stress seen in the unforced flow. This reduction of positive Reynolds shear stress is interpreted as a weakening of vortices relative to the unforced flow. Lastly, the plots in figure 4.9 all have positive regions below the large negative region. These near-wall positive regions demonstrate that the reactive control reduced, and even eliminated in some cases, the negative region of Reynolds shear stress seen close to the wall seen in the unforced flow.

For both  $v$ - and  $u$ -control, increasing gain magnitudes lead to larger positive regions in figure 4.9. This indicates greater reduction of the negative regions of Reynolds stress close to the wall. A second common trend across both control strategies in figure 4.9 is the increase in magnitude of the negative regions with increasing gain magnitude. This trend indicates that increasing actuation amplitudes, regardless of direction, generally reduce the strength of vortices within the wake flow. As well, these negative regions indicate areas where the production of TKE is reduced relative to the unforced flow.

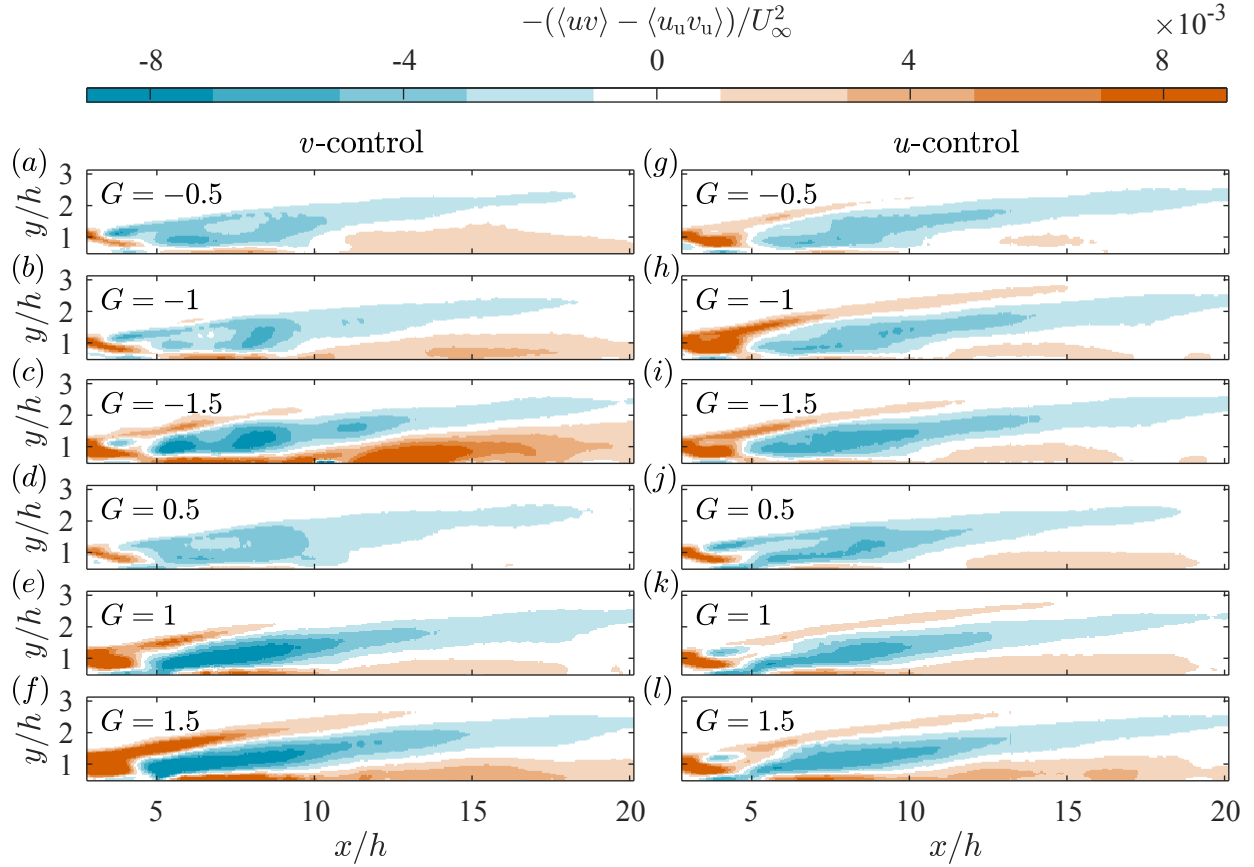


Figure 4.9: Reynolds shear stress field relative to that of the unforced flow for (a – f)  $v$ -control and (g – l)  $u$ -control cases at all tested gain values and with  $(\Delta x_s, y_s)/h = (-0.6, 1.1)$ .

Regarding the  $v$ -control cases, figures 4.9(a – f), the trends exhibited are relatively consistent with those shown by figures 4.7 and 4.8. The negative gain cases show a steady increase in the magnitude of the negative and positive regions with increasing gain magnitude. For the positive gain cases there is a relatively large increase in the magnitudes of the positive and negative regions when the gain increases from 0.5 to 1. From a gain of 1 to 1.5, however, there is relatively little change in the Reynolds stress field. As well, the negative gain cases of  $v$ -control appear to have a larger impact on the Reynolds stresses close to the wall compared to the positive gain cases.

The  $u$ -control cases likewise show increasing magnitudes of the positive and negative regions with increasing gain. Consequently, vortices were further weakened and the near-wall flow is disrupted more by larger amplitudes of both opposing and compliant actuations. The negative gain

cases, figures 4.9( $g - i$ ), have positive and negative regions that are relatively lower in magnitude than those of the positive gain cases, figures 4.9( $j - l$ ). This indicates that the positive gain cases had an overall larger impact on the Reynolds stress field.

From the above discussion of figures 4.7 – 4.9, it is evident that there were notable differences between  $v$ - and  $u$ -control, and both were sensitive to changes in gain magnitude and sign. The differences observed between cases of each control strategies for gains of opposite sign are particularly encouraging as this indicates that the opposing and compliant actuations are impacting the flow in different ways. This suggests that  $v$ - and  $u$ -control are able to impact the flow in consistent ways that, with further development, can be harnessed to control flows toward desired states. The negative gain cases of  $v$ -control present some of the most compelling results in that the mean flow fields indicate that sweep motions are increasingly inhibited from penetrating towards the wall with increasing strength of opposing actuations. This is a significant drag reduction mechanism of the  $v$ -control strategy numerically investigated by Choi et al. (1994). As such, the observation of this effect indicates that the  $v$ -control applied in this work is behaving to some extent as was predicted by numerical works.

### 4.3.3 Impacts of sensor location

We have so far characterized the impact of gain sign and magnitude on the average flow fields during the application of  $v$ - and  $u$ -control for a single location of sensor IWs. The remaining discussion in this chapter describes the impact of sensor location on the two control schemes when applying opposing and compliant actuations. Only the average streamwise velocity fields are considered in this chapter as similar conclusions are drawn from the wall-normal velocity fields.

As previously outlined, sensors were offset from their respective actuators by  $(\Delta x_s, y_s)$ . Here,  $\Delta x_s/h$  values of  $-0.6$ ,  $-0.9$ , and  $-1.2$  are evaluated along with  $y_s/h$  values of  $1.1$  and  $1.5$ . The three  $\Delta x_s$  values were selected with consideration for the estimated delays inherent to the measurement and actuation systems. For  $\Delta x_s/h = -0.9$ , actuations will occur directly below the fluid motions measured by the RT-PIV system. Accordingly,  $\Delta x_s/h$  values of  $-0.6$  and  $-1.2$  correspond to actuations that lag and precede the fluid motions they are intended to target, respectively. As

well, the two  $y_s$  values were selected as they covered a range within which peak streamwise and wall-normal velocity fluctuations occurred.

Figure 4.10 shows the average streamwise flow fields relative to that of the unforced flow for  $v$ - and  $u$ -control with a gain of  $-1$  (opposing actuations) and for each of the six different sensor locations. Regarding the two  $y_s$  values tested, a general result across almost all the subplots is that the positive regions have a reduced magnitude for  $y_s/h = 1.5$  as compared to cases with  $y_s/h = 1.1$ . As highlighted by chapter 4.1, for  $y_s/h = 1.5$  the active surface saw lower actuation amplitudes in comparison to the cases with  $y_s/h = 1.1$ . As such, the weaker positive regions shown by cases with  $y_s/h = 1.5$  are attributed to this weaker actuation. The near-wall negative regions show less of a consistent effect of  $y_s$ . For  $v$ -control there appears to be relatively minimal effect of the  $y_s$  value on the negative near-wall regions. However, for  $u$ -control the near-wall negative regions are larger in size and magnitude for cases with  $y_s/h = 1.5$ .

Changes to the  $\Delta x_s$  value likewise demonstrate some notable impacts on the effects of  $v$ -control applying opposing actuations, figures 4.10(a – f). For cases with  $y_s/h = 1.1$ , moving the sensors further upstream, i.e.,  $\Delta x_s/h$  goes  $-0.6$  to  $-1.2$ , resulted in slight increases to the velocity deficit recovery rate in the near-wake while also decreasing the extent of flow speed reductions close to the wall. The cases with  $y_s/h = 1.5$  show a decrease in both the near-wake velocity deficit recovery rate and in the reduction of the near-wall flow speed when the sensors are moved further upstream. The weaker reduction of the near-wall flow speed for more upstream sensor locations could indicate that sweep motions penetrate toward the wall to a greater extent for these cases.

The opposing actuation  $u$ -control cases show similar trends across the different  $\Delta x_s$  values at both  $y_s$  values. Comparing cases with  $\Delta x_s/h = -0.6$  and  $-0.9$ , the more upstream sensor position ( $\Delta x_s/h = -0.9$ ) leads to a lower near-wake velocity deficit recovery rate and greater reduction of the near-wall flow speed. From  $\Delta x_s/h = -0.9$  to  $-1.2$ , however, the opposite occurs. The cases with  $\Delta x_s/h = -1.2$  show greater near-wake velocity deficit recovery rates and less reduction of the near-wall flow speed in comparison to cases with  $\Delta x_s/h = -0.9$ .

Figure 4.11 shows the average streamwise flow fields relative to that of the unforced flow for  $v$ - and  $u$ -control with a gain of one (compliant actuations) and for each of the six different sensor

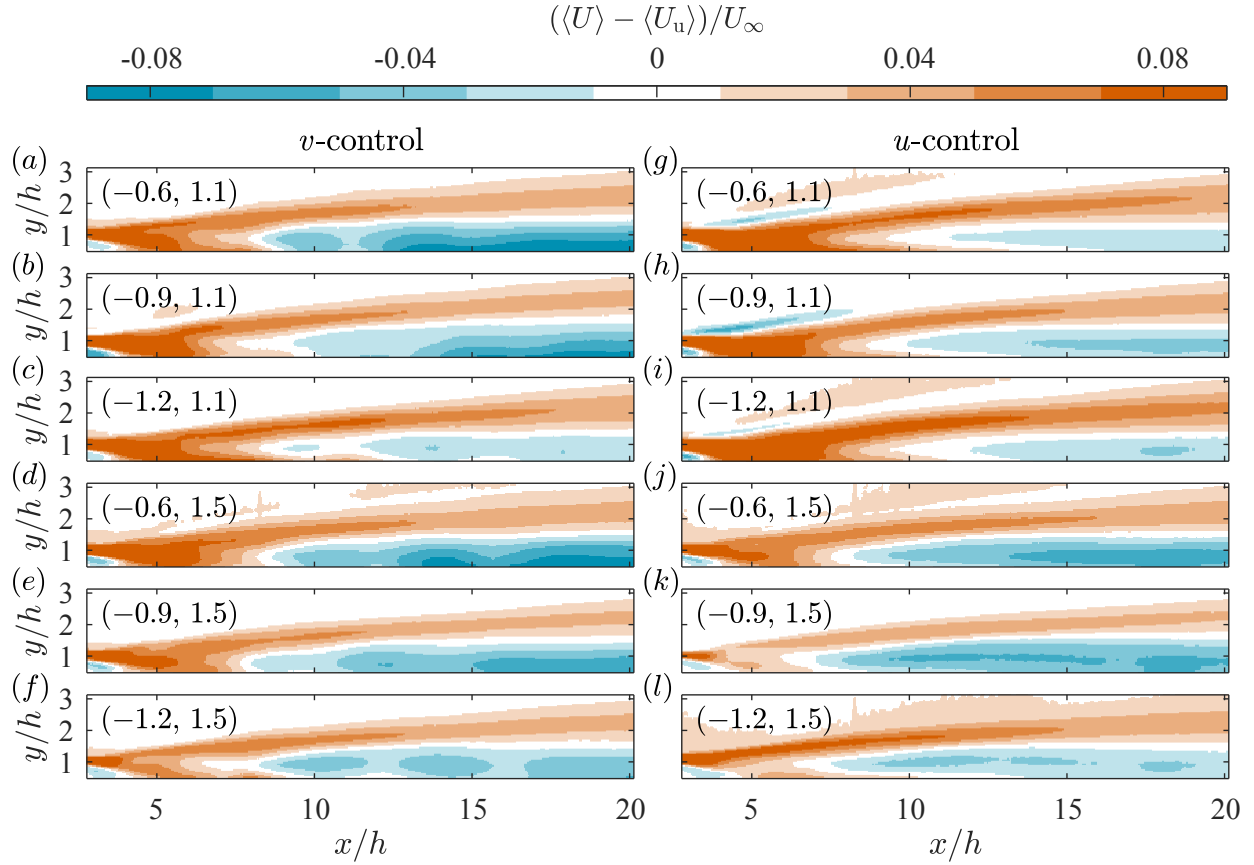


Figure 4.10: Average streamwise velocity fields relative to that of the unforced flow for reactive control cases with a gain of  $-1$  and at the six tested sensor locations. Text in the upper left corner of each plot is  $(\Delta x_s, y_s)/h$  for each case.

locations. The two  $y_s$  values appear to effect the strength of the positive regions. Cases with  $y_s/h = 1.5$  generally have weaker positive regions compared to cases with  $y_s/h = 1.1$ . As with the opposing actuation cases in figure 4.10, This is attributed primarily to weaker actuation of the surface for cases with  $y_s/h = 1.5$ . As well, for both  $v$ - and  $u$ -control, cases with  $y_s/h = 1.1$  predominantly show stronger reductions of the near-wall flow speed.

The impact of  $\Delta x_s$  on  $v$ -control applying compliant actuations, figures 4.11(a - f), is significant and differs at the two  $y_s$  values. Cases with  $y_s/h = 1.1$  show a small decrease in the near-wake velocity deficit recovery rate with increasing upstream sensor positions. As well, there is a significant increase in the reduction of the near-wall flow speed as  $\Delta x_s/h$  goes from  $-0.6$  to  $-0.9$ . As such, the opposition of sweep motions penetrating toward the wall is increased by the more upstream sensor

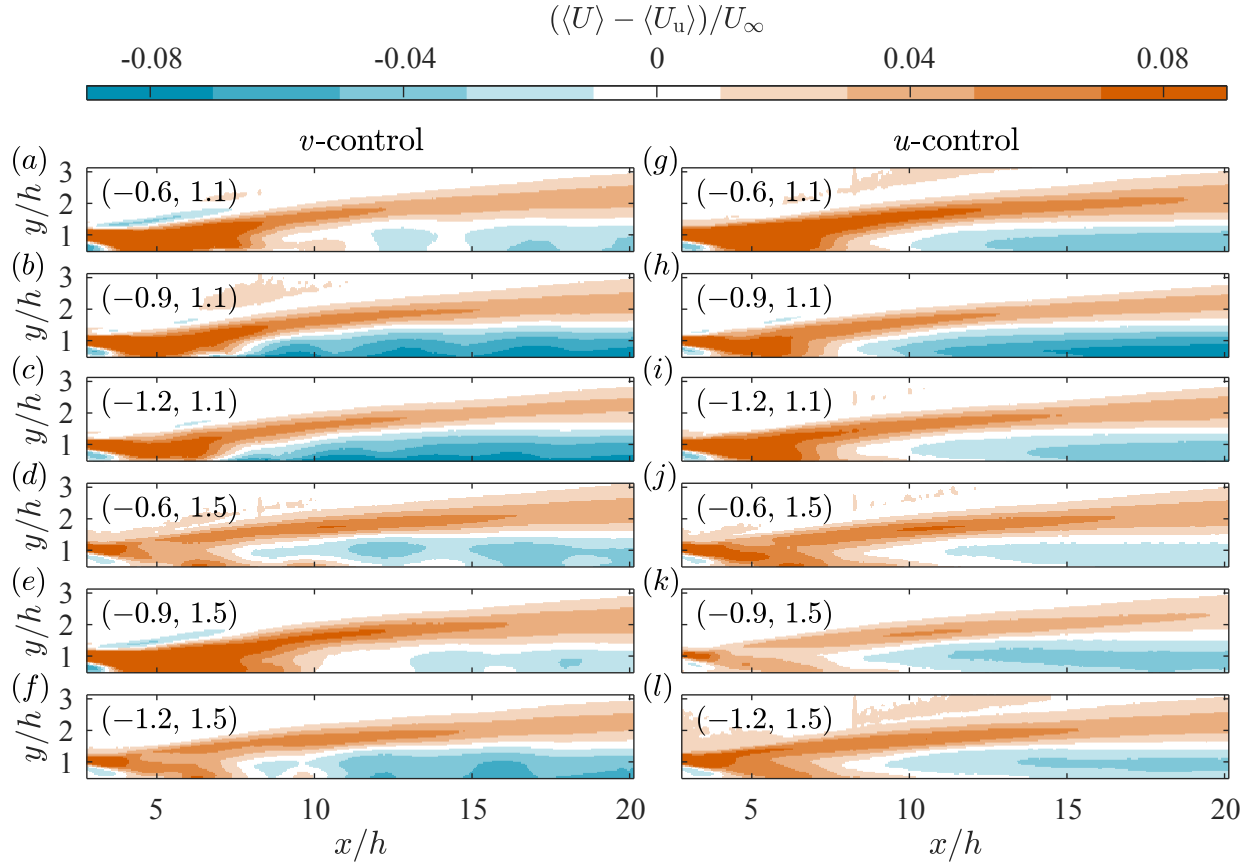


Figure 4.11: Average streamwise velocity fields relative to that of the unforced flow for reactive control cases with a gain of 1 and at the six tested sensor locations. Text in the upper left corner of each plot is  $(\Delta x_s, y_s)/h$  for each case.

position. For the compliant actuation  $v$ -control cases with  $y_s/h = 1.5$ , figures 4.11(d - f), the cases with  $\Delta x_s/h = -0.6$  and  $-1.2$  are relatively similar and show near-wake velocity deficit recovery rates and near-wall flow speed reductions of moderate strength compared to the other plots in figure 4.11. The case with  $\Delta x_s/h = -0.6$ , figures 4.11(e), has a significantly increased near-wake velocity deficit recovery rate and shows quite minimal reduction of the near-wall flow speed. Consequently, this case appears to have induced relatively little opposition to sweep motions.

The effect of  $\Delta x_s$  on compliant actuation cases of  $u$ -control is similar to the effect it had for opposing actuation cases of  $u$ -control. The cases with  $\Delta x_s/h = -0.9$  have slightly lower near-wake velocity deficit recovery rates and greater reductions of the near-wall flow speed compared to cases with the other two streamwise sensor locations. As such, the cases with  $\Delta x_s/h = -0.9$  appear to

have most strongly opposed the advance of sweep motions toward the wall.

Considering figures 4.10 and 4.11 together, it is evident that  $v$ - and  $u$ -control were sensitive to sensor location when applying opposing and compliant actuations. The effects of sensor location differed significantly for  $v$ -control applying opposing actuations compared to  $v$ -control applying compliant actuations. The greatest reduction of the near-wall flow speed is achieved with  $\Delta x_s/h = -0.6$  for opposing actuations and with  $\Delta x_s/h = -1.2$  for compliant actuations. As well, the opposing actuations cases show consistent changes in the positive and negative regions with changing streamwise sensor position. This is not observed for the compliant actuation cases. Regarding  $u$ -control, there is greater similarity between the effects of sensor location between cases applying opposing and compliant actuations. The primary difference that is observed is that, for opposing actuations, the greatest reduction of the near-wall flow speed occurs with  $y_s/h = 1.5$ , while for compliant actuations, it occurs with  $y_s/h = 1.1$ .

#### 4.4 Suppression of vortex shedding

The disruption of the periodic flow is investigated here using proper orthogonal decomposition (POD) based on the snapshot method of Sirovich (1987). The spatial modes produced by POD are sorted by their TKE and, as such, can provide information on the importance of different structures. For this work, data within the region of  $x/h = 5 - 18.3$  and  $y/h = 0.5 - 3.3$  is analysed. The streamwise range extends from just upstream of the first actuator to slightly downstream of the final actuator. Additionally, the lower wall-normal limit of  $y/h = 0.5$  is applied to exclude data close to the wall that may have been corrupted by active wall deformations. The upper wall-normal limit of  $y/h = 3.3$  simply represents upper spatial limit of the data. This FOV is used for the POD analysis as it includes only portions of the flow directly being acted upon by reactive control.

Figure 4.12 shows the energy content of the first six POD modes for the unforced flow and  $v$ - and  $u$ -control with  $(\Delta x_s, y_s) = (-0.9, 1.1)$ . Note that in figure 4.12, all of the mode energies are normalized by the TKE of the unforced flow ( $E_{t,u}$ ) as opposed to the TKE of the corresponding reactive control case. This allowed for a clearer comparison of the energy content of the spatial modes. The unforced flow shows two dominant modes that account for approximately 65% of the

TKE contained within the unforced flow. These dominant modes correspond to the vortex shedding process. Likewise, the first two modes of the reactive control cases, at all gains, also correspond to the vortex shedding process. This was verified through inspection of the spatial pattern of the modes and the spectra of the corresponding time-varying coefficients. The energy of the first two modes is significantly lower for all the reactive control cases compared to the unforced flow. As such, although the vortex shedding process continues to contribute a significant proportion of the TKE of the flow for the reactive control cases, the energy of the vortex shedding process is significantly reduced compared to that of the unforced flow.

Regarding the impacts of varying gain, it is evident in figure 4.12 that increasing gain magnitude leads to further reductions in the energy content of the first two POD modes. Therefore, larger gain magnitudes, which correspond to larger actuation amplitudes, result in greater attenuation and disruptions of the vortex shedding. This agrees with observations previously drawn from the analyses of the mean flow fields. Two of the  $u$ -control cases shown by figure 4.12(b) have third POD modes with energies above 10% of  $E_{t,u}$ . Several  $u$ -control cases at other sensor locations and predominantly with negative gains also show third POD modes with energies above 10% of  $E_{t,u}$ . This third high energy mode was attributed to structures generated above the actuators due to large actuations. Interestingly, none of the  $v$ -control cases exhibit this third high energy POD mode.

As illustrated by figure 4.12, the energy content of the first two POD modes is descriptive of the overall impact of each of the tested reactive control schemes on the vortex shedding. As such, figure 4.13 was created showing the sum of the energy contributions from the first two POD modes,  $E_s = E_1 + E_2$ , for all the investigated reactive control cases. The cumulative energies shown by figure 4.13 are all normalized by  $E_s$  for the unforced flow ( $E_{s,u}$ ). Figure 4.13 reinforces the conclusions previously drawn regarding the influences of varying gain. Except for a few reactive control cases, increasing gain magnitude is predominantly associated with greater reduction of the energy of the first two POD modes and, consequently, the energy of the vortex shedding process. Furthermore, figure 4.13 highlights that the lowest  $E_s$  values for both  $v$ - and  $u$ -control are achieved by cases with negative gains. For opposing actuation (negative gain) cases,  $v$ -control has a minimum  $E_s$

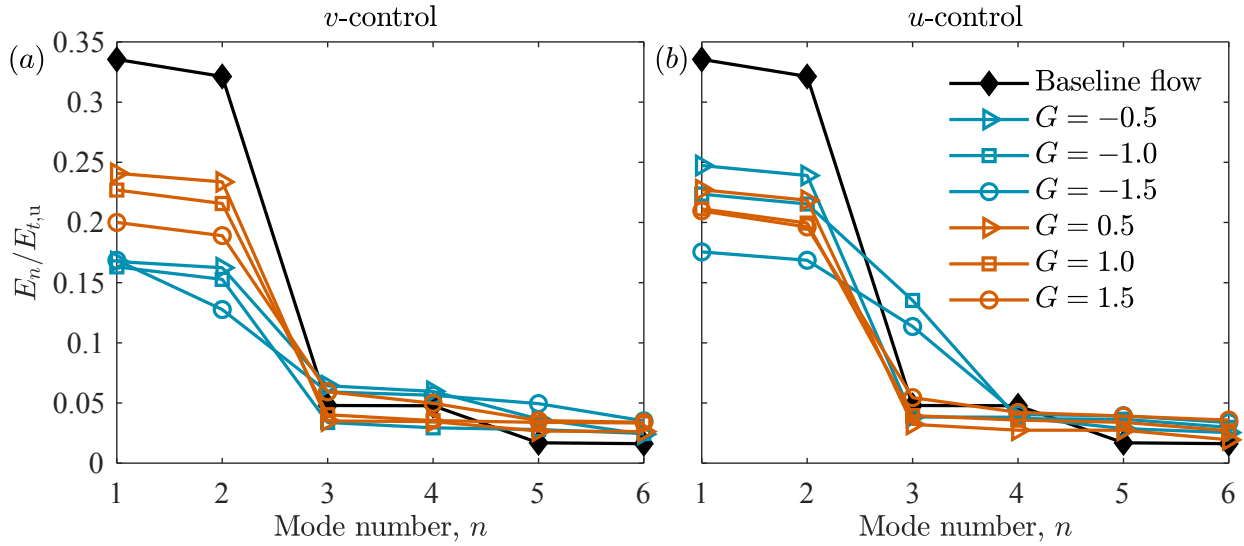


Figure 4.12: Energies of first six POD modes for (a)  $v$ -control and (b)  $u$ -control at different gains ( $G$ ) with  $(\Delta x_s, y_s)/h = (-0.9, 1.1)$ . Mode energies ( $E_n$ ) are normalized by the turbulent kinetic energy of the unforced flow ( $E_{t,u}$ ).

value of  $0.31E_{s,u}$  with a gain of  $-1.5$  and  $(\Delta x_s, y_s)/h = (-1.2, 1.1)$ , while  $u$ -control a minimum  $E_s$  value  $0.41E_{s,u}$  with a gain of  $-1.5$  and  $(\Delta x_s, y_s)/h = (-0.6, 1.1)$ . For compliant actuations (positive gain) cases, the minimum  $E_s$  values are respectively  $0.42E_{s,u}$  and  $0.52E_{s,u}$  for  $v$ - and  $u$ -control with a gain of  $1.5$  and  $(\Delta x_s, y_s)/h = (-1.2, 1.1)$ . This indicates that opposition control for both reactive control strategies has a greater ability to disrupt the vortex shedding.

Figure 4.13 also demonstrates a complete picture of the effects of different sensor locations. For  $v$ -control the effect of the varied sensor locations differs between the cases with positive and negative gains. For cases with negative gains, there is a separation between cases with the two different  $y_s$  values. Those cases with  $y_s/h = 1.1$  have lower  $E_s$  values than the cases with  $y_s/h = 1.5$ . This observation may in part be attributed to the larger actuation amplitudes for cases with  $y_s/h = 1.1$ , as highlighted by figure 4.1. For positive gains there is more overlap of cases with both  $y_s$  values. This suggests that the negative gain  $v$ -control cases are more sensitive to changes in the  $y_s$  value than those with positive gains.

For  $v$ -control with negative gains and  $y_s/h = 1.5$ , there is a relatively consistent trend of decreasing  $E_s$  values with moving the sensor location from  $\Delta x_s/h = -0.6$  to  $-1.2$ . This trend can

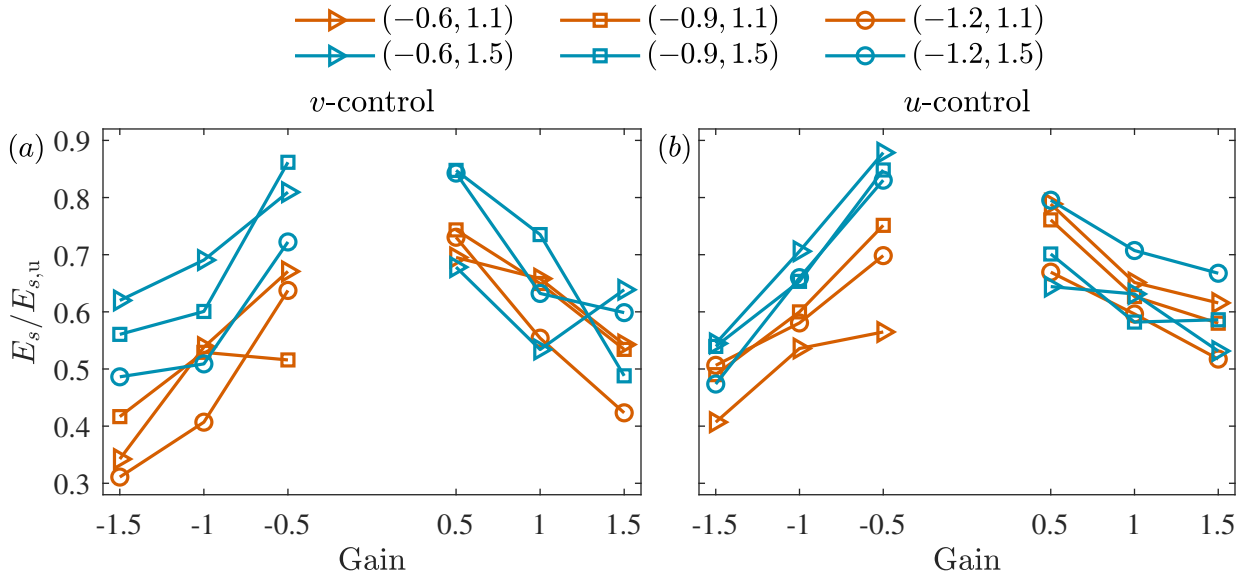


Figure 4.13: Sum of energy of first two POD modes ( $E_s$ ) for (a)  $v$ -control and (b)  $u$ -control cases.  $E_s$  is normalized by  $E_s$  of the unforced flow ( $E_{s,u}$ ) in all cases. The numbers in brackets in the legend indicate  $(\Delta x_s, y_s)/h$  for each case.

likewise be observed for  $v$ -control cases with positive gains and  $y_s/h = 1.1$ . This indicates that, for these two groups, changes in the effect of  $v$ -control at different  $\Delta x_s$  values can be attributed to the changes in timing that the different streamwise sensor positions induce. For negative gain  $v$ -control cases with  $y_s/h = 1.1$  and positive gain cases with  $y_s/h = 1.5$ , the energy of the first two POD modes does not vary consistently according to the streamwise position of the sensors. As such, for these two groups the change in energy of the first two POD modes is dependent on both the gain and the streamwise sensor position.

The  $u$ -control cases in figure 4.13(b) show significant effects of different sensor location on  $E_s$ . With regards to the negative gain cases, those with  $y_s/h = 1.5$  show larger changes in  $E_s$  as the gain magnitude increases in comparison to cases with  $y_s/h = 1.1$ . The positive gain  $u$ -control cases with both  $y_s$  values overlap significantly. As such, this indicates the  $y_s$  value has a relatively smaller impact on the positive gain cases than it does on the negative gain cases. As well, for the negative gain cases with  $y_s/h = 1.1$  and positive gain cases with  $y_s/h = 1.5$ , the value of  $E_s$  decreases consistently with moving the sensors from  $\Delta x_s/h = -1.2$  to  $-0.6$ . For the positive gain cases with  $y_s/h = 1.1$  and negative gain cases with  $y_s/h = 1.5$ , the opposite relation is observed. These cases

show an increase to the value of  $E_s$  with moving the sensors from  $\Delta x_s/h = -1.2$  to  $-0.6$ . The inversion of trends in  $E_s$  between cases with the same gain sign and different  $y_s$  values may be attributed to the shapes of fluid motions in the flow. Positive  $u$  regions extend further downstream at  $y/h = 1.1$  compared to  $y/h = 1.5$ . As such, cases with  $y_s/h = 1.1$  will detect positive  $u$  regions slightly earlier than cases with  $y_s/h = 1.5$ . Consequently, more upstream positioning of sensors for cases with  $y_s/h = 1.5$  results in similar timing of actuations to cases with  $y_s/h = 1.1$  and less upstream sensor positions. As well, the inverse trends in  $E_s$  for cases with different gain signs and the same  $y_s$  value may be attributed to actuations beginning to interact with fluid motions upstream or downstream of the targeted fluid motion. For example, if we consider a negative gain  $u$ -control case with  $y_s/h = 1.1$  and  $\Delta x_s/h = -1.2$  (the most upstream sensor position), it may be acting somewhat on the fluid motion downstream of the intended one and, thus, the actuation does not have as much of the intended opposing effect.

## Chapter 5

# Conclusions

Active flow control is an area of research with immense potential for improving the efficacy and efficiency of engineering systems. In wall-bounded turbulent flows, active flow control may allow for significant drag reductions to be achieved. This can aid in reducing the energy intensity of vital industries. The current investigation has improved understandings of reactive control strategies relevant to the control of turbulent wall-bounded flows. The development of novel actuation and real-time measurement systems for active control and their application to conduct reactive control of a periodic wall-bounded flow was presented. Section 5.1 of this chapter provides a summary of the findings of the reactive control investigation. Following this, several recommendations for future work that can expand on the findings of this thesis are described by section 5.2.

### 5.1 Summary of results

The objectives of the current investigation were to experimentally implement and evaluate reactive control in a wall-bounded flow using novel actuation and real-time measurement systems. The actuation system developed for forcing the flow was an active deformable surface. It was composed of a streamwise array of sixteen actuation points capable of deforming the wall in the wall-normal direction. As well, the inputs to the reactive control strategies are real-time velocity measurements captured by a real-time particle image velocimetry (RT-PIV) system. The flow that reactive control was applied to was the wake flow behind a spherical cap immersed in a laminar boundary layer. This flow was characterized by the periodic shedding of coherent hairpin vortices that are similar to

the hairpin vortices observed in turbulent wall-bounded flows. As such, the impact of the reactive control strategies on these structures is informative for the eventual control of more complex and turbulent flows.

The reactive control strategies investigated through this work were so called  $v$ -control and  $u$ -control and were inspired in part by similar strategies proposed and numerically investigated by Choi et al. (1994). The  $v$ -control algorithm involved moving the active surface at velocities proportional to wall-normal velocity fluctuations measured close to each actuation location by the RT-PIV system. Similarly, the  $u$ -control algorithm applied wall-normal deformations of the active surface to induce streamwise velocity fluctuations that were proportional to nearby streamwise velocity fluctuations measured by the RT-PIV system. The control strategies were used to apply opposing and compliant actuations of several different strengths. As well, six different sensor locations were investigated to evaluate the effects of changes in streamwise and wall-normal distance between sensing and actuation locations.

The reactive control cases investigated through this work demonstrated a few overall impacts on the flow, although with significant variation in the extent of these effects for different gains and sensor locations. One of the general effects was the inhibited penetration of sweep motions toward the wall. This conclusion was drawn primarily from evaluation of the time-averaged flow fields. This analysis highlighted that, close to and above the active surface, the average streamwise velocity is reduced relative to the unforced flow. As well, the region of average upward flow seen for the unforced flow was held closer to the wall for many reactive control cases. These observations indicate that downwashes of high-speed fluid (sweep motions) penetrated toward the wall to a lesser extent during the application of reactive control. This effect is encouraging as Choi et al. (1994) noted that opposing the wall-ward advance of sweep motions is a mechanism of drag reduction in turbulent wall-bounded flows. A second overall effect of the reactive control was that it has a general disruptive effect on the periodic flow. The level of disruption is closely tied to the amplitude of actuations in most cases. As well, for a majority of cases, greater disruption of the periodic vortex shedding corresponded to a higher turbulent kinetic energy (TKE) of the flow. For these cases, although the primary energetic structures of the flow were weakened, significant turbulent energy

was introduced by the reactive control in the form of other flow motions.

The reactive control investigated here can be broken down into four groups separated by the two reactive control schemes and whether actuations were opposing or compliant. Of these four groups, opposing actuation (negative gain)  $v$ -control has the most grounding in literature as it is closely related to the opposition  $v$ -control first proposed by Choi et al. (1994) and since investigated by many other researchers. The opposition  $v$ -control cases in the current investigation showed some of the strongest indications of opposition toward the wall-ward advance of sweep motions. Furthermore, there appeared to be a consistent increase in the opposition of sweep motions with increasing gain magnitudes and decreasing the streamwise distance from the sensing location. These cases also showed the greatest disruption of the periodic vortex shedding with a minimum cumulative energy of the first two POD modes equal to 31% of the value for the unforced flow. As well, these cases generally had TKE values that were close to or below that of the unforced flow. This highlights that the opposing  $v$ -control was able to attenuate energetic motions in the flow without inducing other flow motions that contributed proportionally more turbulent energy to the flow.

The compliant actuation (positive gain)  $v$ -control cases generally showed weaker regions of average upward flow above the active surface than opposing actuation  $v$ -control cases. This indicates that these cases did not oppose the wall-ward penetration of sweep motions to the extent seen with opposing  $v$ -control cases. The extent of opposition to sweep events also did not follow a clear trend based on gain magnitude or sensor location. As well, the level of disruption of vortex shedding is less for compliant  $v$ -control cases compared to opposing actuation cases. The minimum value for the cumulative energy of the first two POD modes was 42% of the value for the unforced flow. The TKE of the flow for these cases correlated strongly with actuation amplitude with larger actuation amplitudes corresponding to higher TKE values. The TKE of these cases was also higher on average than that for the opposing actuation  $v$ -control cases. As such,  $v$ -control applying compliant actuations caused relatively less disruption and more excitation of the flow.

The opposing actuation  $u$ -control cases showed relatively weak opposition of sweep motions. The strength of opposition to the wall-ward penetration of sweep motions decreased with increasing gain magnitudes and was consistently strongest for cases with streamwise sensor offsets of  $\Delta x_s/h = -0.9$ .

Both the level of disruption of vortex shedding and the TKE of the flow correlated with actuation amplitude. Larger actuation amplitudes correspond to greater disruption of vortex shedding and higher TKE values, and vice versa for smaller actuation amplitudes. It was interesting to note that the level of disruption increased with gain value (i.e., actuation amplitude) while the opposition of sweep motions decreased. This suggests that disruption of the periodic flow does not necessarily correspond to greater opposition to the penetration of sweep motions toward the wall.

Lastly, compliant actuation  $u$ -control cases showed relatively strong opposition against sweep motions penetrating toward the wall. As with opposing actuation  $u$ -control cases, the extent of the opposition decreased with increasing gain magnitude and was strongest for cases with  $\Delta x_s/h = -0.9$ . The maximum level of disruption of the vortex shedding was relatively small compared to all of the other groups of cases. The minimum value for the cumulative energy of the first two POD modes was 52% of the value for the unforced flow. This was 11% higher than the minimum value for opposing actuation  $u$ -control cases and 21% higher than the minimum value for  $v$ -control cases. Regarding TKE, the compliant actuation  $u$ -control resulted in lower values on average compared to  $u$ -control with opposing actuation. The compliant actuation cases of  $u$ -control also have a maximum TKE value of 113% of the value for the unforced flow. This is 9 – 13% lower than the maximum values of the other three groups of reactive control cases. Consequently, the compliant actuation  $u$ -control was able to significantly diminish the penetration of sweep motions toward the wall while having relatively smaller impacts on the energy and periodicity of the flow.

Consequently, regarding the four types of reactive control investigated here, they all produced some interesting effects on the flow. The opposition  $v$ -control and compliant  $u$ -control cases were perhaps the most compelling as they showed the greatest opposition against sweep motions penetrating toward the wall. As well, the stronger opposition against sweep motions shown by  $u$ -control cases with lower actuation amplitudes is intriguing and supports the idea that small actuations may be able to efficiently control wall-bounded flows. A significant amount of further work on reactive control is required, however, the results of the current investigation are encouraging that it has potential for successful application to real-world flows.

In closing, it is worth noting that the RT-PIV system utilized in the current investigation is not

a practical sensor for eventual real-world applications of AFC. However, the use of RT-PIV systems can allow for physical experimentation that begins to approach the complexity seen in numerical works on AFC. Once effective AFC strategies are developed with the wealth of information provided by RT-PIV, efforts can begin to be made to transition these strategies to more practical states using wall-measurable flow variables.

## 5.2 Future work

The work outlined by this thesis presents opportunities for a variety of extensions that may further advance experimental investigations of active flow control. Several future work recommendations are briefly summarized below.

### **Reactive control of a turbulent boundary layer**

Almost all of cited works on reactive control in this thesis have studied the effects of reactive control on turbulent wall-bounded flows. The current investigation, however, applied reactive control to a periodic wake flow from a spherical cap immersed in a laminar boundary layer. This presented a significant challenge to drawing connections between the results of the current investigation and those from literature. As such, it is recommended to conduct reactive control experiments on a turbulent boundary layer using an active deformable surface and RT-PIV system similar to those used in the current investigation. This could yield more direct comparisons to and validation of existing reactive control literature. One of the primary challenges to conducting this investigation would likely involve developing a RT-PIV system capable of measuring a turbulent flow at a high enough rate and with a low enough latency to allow reactive control to be applied.

### **Implementation of machine learning and more advanced control strategies**

The reactive control schemes implemented in the experiments outlined by this thesis are quite basic and used only a fraction of the real-time measurement data that was captured by the RT-PIV system. As is outlined by Brunton and Noack (2015) and Duriez et al. (2017), there are a variety of other promising flow control strategies and machine learning techniques that could perhaps better

harness the active deformable surface and real-time data produced by the RT-PIV system. Consequently, there is significant potential for investigating a variety of more advanced flow control and machine learning strategies using the experimental apparatus developed for this work.

### **Characterization of active deformable surface arrays and geometries**

The capabilities of active deformable surfaces for controlling wall-bounded flows is an area with significant room for development. Gibeau and Ghaemi (2022, 2023) characterized the behaviour of a single deformable surface actuator in laminar and turbulent boundary layers. These investigations provided valuable insights into the effects of these types of actuators; however, there is still a large amount of further investigation that can be done. The active deformable surface developed for this thesis could be utilized and adapted to characterize the impacts of different arrays and geometries of active deformable surface actuators on wall-bounded flows.

# Bibliography

- M. Acarlar and R. Smith. A study of hairpin vortices in a laminar boundary layer. part 1. hairpin vortices generated by hemisphere protuberance. *Journal of Fluid Mechanics*, 175:1–41, 1987.
- R. Adrian. Hairpin vortex organization in wall turbulence. *Physics of Fluids*, 19:041301, 2007.
- R. Adrian, C. Meinhart, and C. Tomkins. Vortex organization in the outer region of the turbulent boundary layer. *Journal of Fluid Mechanics*, 422:1–54, 2000.
- E. Arik and J. Carr. Digital particle image velocimetry system for real-time wind tunnel measurements. In *Proceedings of the International Congress on Instrumentation in Aerospace Simulation Facilities*, pages 267–273, Pacific Grove, USA, 1997. IEEE.
- A. Aubert, N. Bochard, and V. Fresse. An adaptive embedded architecture for real-time particle image velocimetry algorithms. In *Proceedings of the 14th European Signal Processing Conference*, pages 1–4, Florence, Italy, 2006. IEEE.
- P. Bandyopadhyay. Large structure with a characteristic upstream interface in turbulent boundary layers. *Physics of Fluids*, 23(11):2326–2327, 1980.
- K. Breuer, J. Haritonidis, and M. Landahl. The control of transient disturbances in a flat plate boundary layer through active wall motion. *Physics of Fluids A: Fluid Dynamics*, 1(3):574–582, 1989.
- L. Brunton and B. Noack. Closed-loop turbulence control: progress and challenges. *Applied Mechanics Review*, 67(5):050801, 2015.
- H. Carlson and J. Lumley. Active control in the turbulent wall layer of a minimal flow unit. *Journal of Fluid Mechanics*, 329:341–371, 1996.
- L. Cattafesta and M. Sheplak. Actuators for active flow control. *Annual Review of Fluid Mechanics*, 43:247–272, 2011.
- Y. Cengel and J. Cimbala. *Fluid mechanics: fundamentals and applications*. McGraw-Hill, New York, USA, 2014.
- F. Champagnat, A. Plyer, G. Le Besnerais, B. Leclaire, S. Davoust, and Y. Sant. Fast and accurate piv computation using highly parallel iterative correlation maximization. *Experiments in Fluids*, 50:1169–1182, 2011.
- H. Choi, P. Moin, and J. Kim. Active turbulence control for drag reduction in wall-bounded flows. *Journal of Fluid Mechanics*, 262:75–110, 1994.
- Y. Chung and T. Talha. Effectiveness of active flow control for turbulent skin friction drag reduction. *Physics of Fluids*, 23(2):025102, 2011.
- B. Deng and C. Xu. Influence of active control on stg-based generation of streamwise vortices in near-wall turbulence. *Journal of Fluid Mechanics*, 710:234–259, 2012.

- B. Deng, C. Xu, W. Huang, and G. Cui. Strengthened opposition control for skin-friction reduction in wall-bounded turbulent flows. *Journal of Turbulence*, 21:122–142, 2014.
- T. Duriez, S. Brunton, and B. Noack. *Machine learning control - taming nonlinear dynamics and turbulence*. Springer, 2017.
- T. Endo, N. Kasagi, and S. Yuji. Feedback control of wall turbulence with wall deformation. *International Journal of Heat and Fluid Flow*, 21:568–575, 2000.
- T. Fujiwara, K. Fujimoto, and T. Maruyama. A real-time visualization system for piv. In *Proceedings of the 13th International Conference on Field Programmable Logic and Applications*, pages 437–447, Lisbon, Portugal, 2003. Springer.
- M. Gad-el Hak. *Flow control: passive, active, and reactive flow management*. Cambridge University Press, New York, USA, 2000.
- M. Gad-el Hak, A. Pollard, and J. Bonnet (eds.). *Flow control: fundamentals and practices*. Springer, Berlin, Germany, 1998.
- N. Gautier and J. Aider. Feed-forward control of a perturbed backward-facing step. *Journal of Fluid Mechanics*, 759:181–196, 2014.
- N. Gautier and J. Aider. Real-time planar flow velocity measurements using an optical flow algorithm implemented on gpu. *Journal of Visualization*, 18(2):277–286, 2015.
- N. Gautier, J. Aider, T. Duriez, B. Noack, M. Segond, and M. Abel. Closed-loop separation control using machine learning. *Journal of Fluid Mechanics*, 770:442–457, 2015.
- M. Ge, C. Xu, and G. Cui. Active control of turbulence for drag reduction based on the detection of near wall streamwise vortices by wall information. *Acta Mechanica Sinica/Lixue Xuebao*, 31(4):512–522, 2015.
- B. Gibeau and S. Ghaemi. Laminar boundary layer forcing with active surface deformations. *Physical Review Fluids*, 7(11):114101, 2022.
- B. Gibeau and S. Ghaemi. Manipulation of a turbulent boundary layer using active surface deformations [under review]. *Journal of Fluid Mechanics*, 2023.
- N. Goldin, R. King, A. Patzold, W. Nitsche, D. Haller, and P. Woias. Laminar flow control with distributed surface actuation: damping tollmien-schlichting waves with active surface displacement. *Experiments in Fluids*, 54:1478, 2013.
- E. Hammond, T. Bewley, and P. Moin. Observed mechanisms for turbulence attenuation and enhancement in opposition-controlled wall-bounded flows. *Physics of Fluids*, 9:2421–2423, 1998.
- R. Hanson and H. Buckley. Aerodynamic optimization of the flat-plate leading edge for experimental studies of laminar and transitional boundary layers. *Physics of Fluids*, 53(4):863–871, 2012.
- D. Heitz, E. Mémin, and C. Schnörr. Variational fluid flow measurements from image sequences: synopsis and perspectives. *Experiments in Fluids*, 48:369–393, 2010.
- S. Hommema and R. Adrian. Packet structure of surface eddies in the atmospheric boundary layer. *Boundary-Layer Meteorology*, 106:147–170, 2003.
- J. Jiménez. Coherent structures in wall-bounded turbulence. *Journal of Fluid Mechanics*, 842, 2018.
- S. Kang and H. Choi. Active wall motions for skin-friction drag reduction. *Physics of Fluids*, 12:3301–3304, 2000.

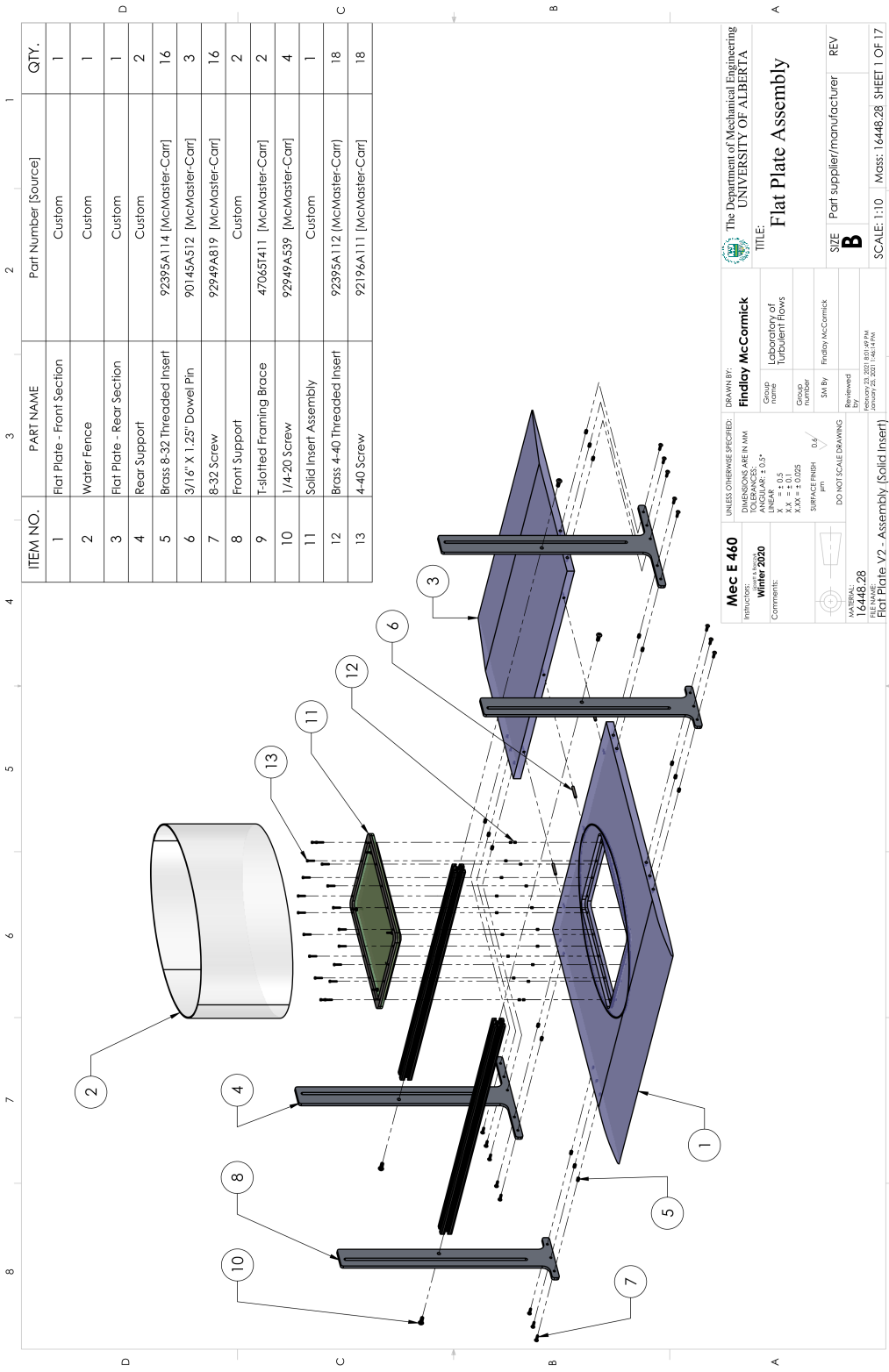
- C. Kim, W. Jeon, and H. Park, J. and Choi. Effect of a localized time-periodic wall motion on a turbulent boundary layer flow. *Physics of Fluids*, 15:265–268, 2003.
- H. Kim, S. Kline, and W. Reynolds. The production of turbulence near a smooth wall in a turbulent boundary layer. *Journal of Fluid Mechanics*, 50(1):133–160, 1970.
- S. Kline, W. Reynolds, F. Schraub, and P. Runstadler. The structure of turbulent boundary layers. *Journal of Fluid Mechanics*, 30(4):741–773, 1967.
- G. Le Besnerais and F. Champagnat. Dense optical flow by iterative local window registration. In *Proceedings of the 2005 IEEE International Conference on Image Processing*, pages 137–140, Genoa, Italy, 2005. IEEE.
- C. Lee, J. Kim, D. Babcock, and R. Goodman. Application of neural networks to turbulence control for drag reduction. *Physics of Fluids*, 9:1740–1747, 1997.
- C. Lee, J. Kim, and H. Choi. Suboptimal control of turbulent channel flow for drag reduction. *Journal of Fluid Mechanics*, 358:245–258, 1998.
- J. Lim and J. Kim. A singular value analysis of boundary layer control. *Physics of Fluids*, 16(2):1980–1988, 2004.
- L. Lorang, B. Podvin, and P. Quere. Application of compact neural network for drag reduction in a turbulent channel flow at low reynolds numbers. *Physics of Fluids*, 20:045104, 2008.
- T. Maruyama, Y. Yamaguchi, and A. Kawase. An approach to real-time visualization of piv method with fpga. In *Proceedings of the 11th International Conference on Field Programmable Logic and Applications*, pages 601–606, Belfast, Ireland, 2001. Springer.
- A. Melling. Tracer particles and seeding for particle image velocimetry. *Measurement Science and Technology*, 8(12):1406–1416, 1997.
- J. Muñoz, D. Dellavale, M. Sonnaillon, and F. Bonetto. Real-time particle image velocimetry based on fpga technology. In *Proceedings of the 5th Southern Conference on Programmable Logic*, pages 147–153, Sao Carlos, Brazil, 2009. IEEE.
- M. Pamiés, E. Garnier, A. Merlen, and P. Sagaut. Opposition control with arrayed actuators in the near-wall region of a spatially developing turbulent boundary layer. *International Journal of Heat and Fluid Flow*, 32(3):621–630, 2011.
- R. Panton. Overview of the self-sustaining mechanisms of wall turbulence. *Progress in Aerospace Sciences*, 37(4):341–383, 2001.
- M. Raffel, C. E. Willert, F. Scarano, C. kähler, S. Wereley, and J. Kompenhans. *Particle Image Velocimetry: A Practical Guide*. Springer, Berlin, Germany, 2018.
- H. Rebbeck and K. Choi. A wind-tunnel experiment on real-time opposition control of turbulence. *Physics of Fluids*, 18:035103, 2006.
- S. Robinson. Coherent motions in the turbulent boundary layer. *Annual Review of Fluid Mechanics*, 23:601–639, 1991.
- T. Schiwietz and R. Westermann. Gpu-piv. In *Proceedings of the 9th Vision, Modelling, and Visualization Conference*, pages 151–158, Stanford, USA, 2004.
- H. Schlichting and K. Gersten. *Boundary-layer theory*. Springer, Berlin, Germany, 2017.
- W. Schoppa and F. Hussain. Coherent structure generation in near-wall turbulence. *Journal of Fluid Mechanics*, 453:57–108, 2002.

- S. Siegel, K. Cohen, T. McLaughlin, and J. Myatt. Real-time particle image velocimetry for closed-loop flow control studies. In *Proceedings of the 41st Aerospace Sciences Meeting and Exhibit*, Reno, USA, 2003. AIAA.
- L. Sirovich. Turbulence and the dynamics of coherent structures, parts i-iii. *Quarterly of Applied Mathematics*, 45(3):561–571, 1987.
- C. Smith, G. Patterson, and J. Zakin. A synthesized model of the near-wall behavior in turbulent boundary layers. In *Proceedings of the 8th Symposium on Turbulence*, pages 299–327, Rolla, USA, 1984. University of Missouri.
- T. Theodorsen. Mechanism of turbulence. In *Proceedings of the Midwestern Conference on Fluid Mechanics*, Columbus, USA, 1952. Ohio State University.
- E. Varon, J. Aider, Y. Eulalie, S. Edmige, and P. Gilotte. Adaptive control of the dynamics of a fully turbulent bimodal wake using real-time piv. *Experiments in Fluids*, 60:124, 2019.
- Y. Wang, W. Huang, and C. Xu. Active control for drag reduction in turbulent channel flow: the opposition control schemes revisited. *Fluid Dynamics Research*, 48:055501, 2016.
- C. Willert, M. Munson, and M. Gharib. Real-time particle image velocimetry for closed-loop flow control applications. In *Proceedings of the 15th International Symposium on Applications of Laser Techniques to Fluid Mechanics*, Lisbon, Portugal, 2010.
- C. Xu, J. Choi, and H. Sung. Suboptimal control for drag reduction in turbulent pipe flow. *Fluid Dynamics Research*, 30:217–231, 2002.
- H. Yu, M. Leaser, G. Tadmor, and S. Siegel. Real-time particle image velocimetry for feedback loops using fpga implementation. *Journal of Aerospace Computing, Information, and Communication*, 3:52–57, 2006.
- J. Zhou, R. Adrian, and S. Balachandar. Autogeneration of near-wall vortical structures in channel flow. *Physics of Fluids*, 8(1):288–290, 1996.

# Appendices

## **A Technical drawings of experimental apparatuses**

This section contains technical drawings of the flat plate apparatus and active deformable surface components. Note that item number 2 in the flat plate assembly drawing on page 83 was included in the initial design but excluded from the final assembly used for experimentation as it was judged unnecessary.



ITEM NO.	PART NAME	Part Number [Source]	QTY.
1	Flat Plate - Front Section	Custom	1
2	Water Fence	Custom	1
3	Flat Plate - Rear Section	Custom	1
4	Rear Support	Custom	2
5	Brass 8-32 Threaded Insert	92395A114 [McMaster-Carr]	16
6	3/16" X 1.25" Dowel Pin	90145A512 [McMaster-Carr]	3
7	8-32 Screw	92949A819 [McMaster-Carr]	16
8	Front Support	Custom	2
9	T-slotted Framing Brace	47065T411 [McMaster-Carr]	2
10	1/4-20 Screw	92949A539 [McMaster-Carr]	4
11	Solid Insert Assembly	Custom	1
12	Brass 4-40 Threaded Insert	92395A112 [McMaster-Carr]	18
13	4-40 Screw	92196A111 [McMaster-Carr]	18

**Mec E 460**  
 INSTRUCTOR: **Winter 2020**  
 Comment:

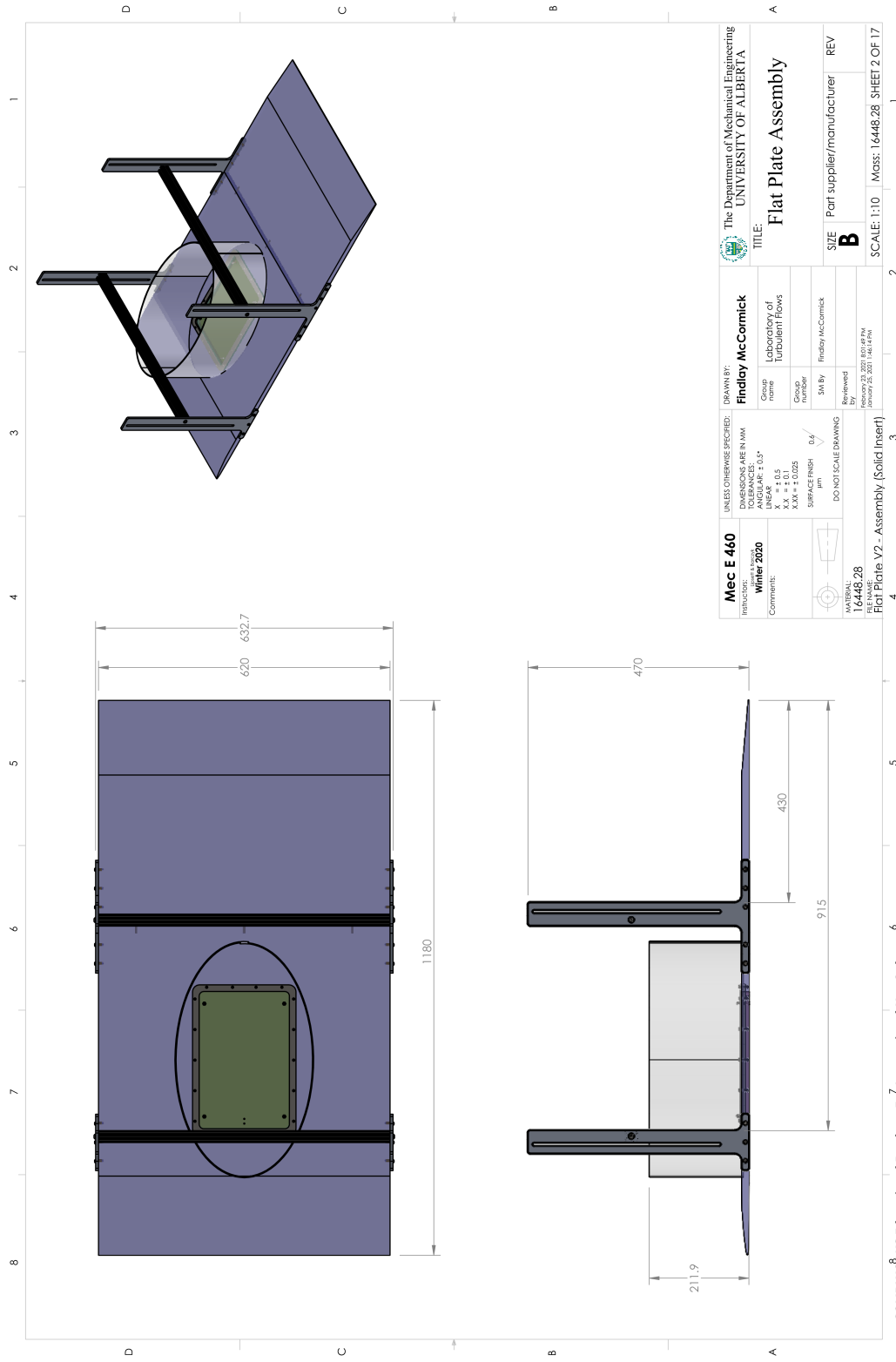
UNLESS OTHERWISE SPECIFIED:  
 DIMENSIONS ARE IN MM  
 ANGULAR ± 0.5°  
 LINEAR ± 0.5  
 X.X ± 0.1  
 X.XX ± 0.025  
 SURFACE FINISH: 0.8  
 DO NOT SCALE DRAWING

DRAWN BY: **Findley McCormick**  
 Group name: Laboratory of Turbulent Flows  
 Course: Mech 460  
 SM By: Findley McCormick  
 Reviewed By: [Blank]  
 Date: January 25, 2021 1:01:14 PM  
 File Name: Flat Plate V2 - Assembly (Solid Insert)

The Department of Mechanical Engineering  
 UNIVERSITY OF ALBERTA  
**Flat Plate Assembly**

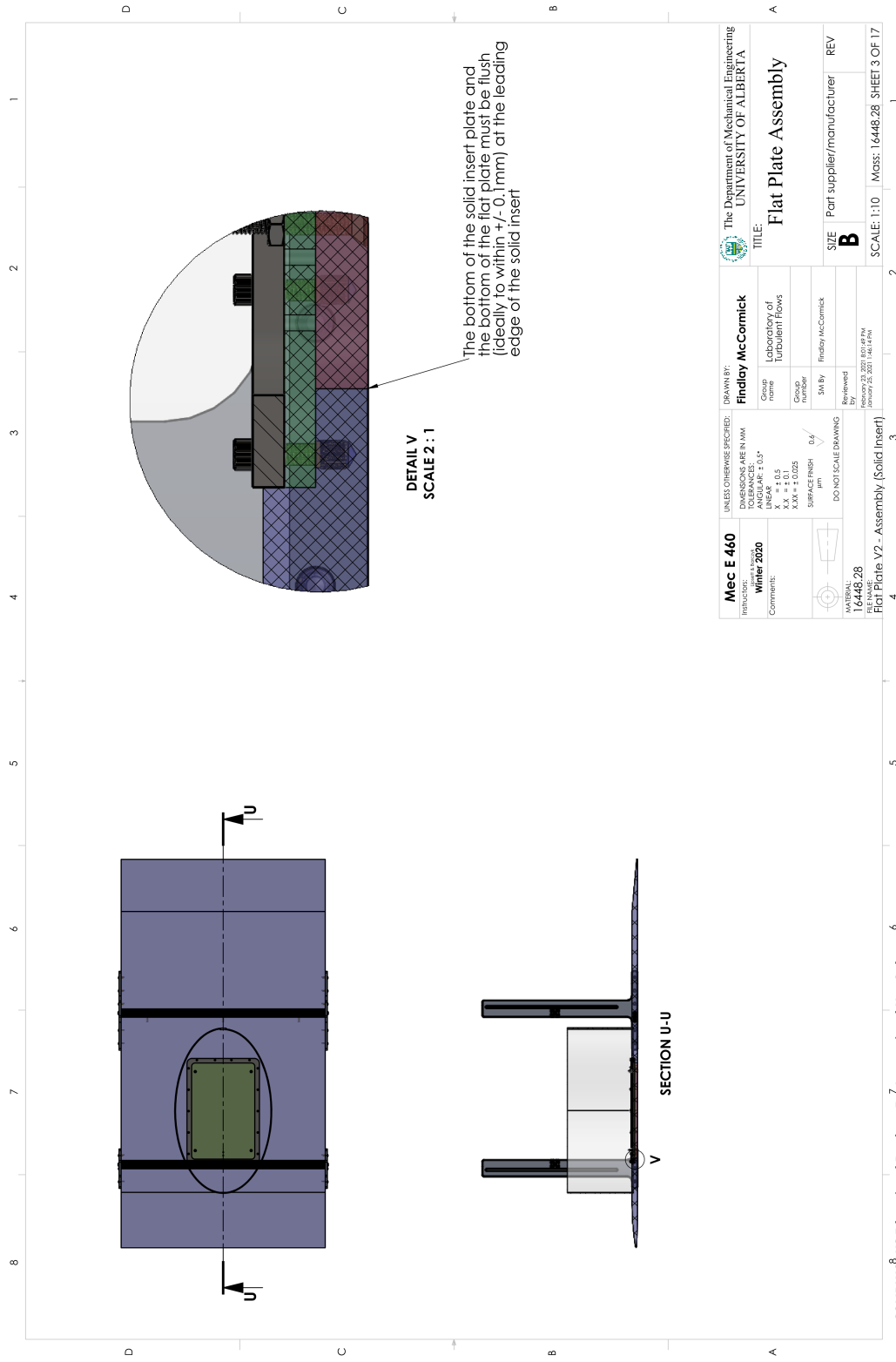
SIZE: Part supplier/manufacturer  
**B**  
 SCALE: 1:10 Mass: 16448.28 SHEET 1 OF 17

SOLIDWORKS Educational Product. For Instructional Use Only.



<b>Mec E 460</b>		DRAWN BY: <b>Findley McCormick</b>		The Department of Mechanical Engineering UNIVERSITY OF ALBERTA	
INTRODUCTION: <b>Winter 2020</b>		Client name: Laboratory of Turbulent Flows		TITLE: <b>Flat Plate Assembly</b>	
Comments:		Group number: Frindley McCormick		SIZE: Part supplier/manufacturer	
SURFACE FINISH: 0.6 μm		SW By: Frindley McCormick		REV: <b>B</b>	
DO NOT SCALE DRAWING		Reviewed By: Frindley McCormick		SCALE: 1:10	
FILE NAME: <b>16448_28</b>		Date: January 28, 2021 10:14 AM		Mass: 16448.28	
Flat Plate V2 - Assembly (Solid Insert)				SHEET 2 OF 17	

SOLIDWORKS Educational Product. For Instructional Use Only.

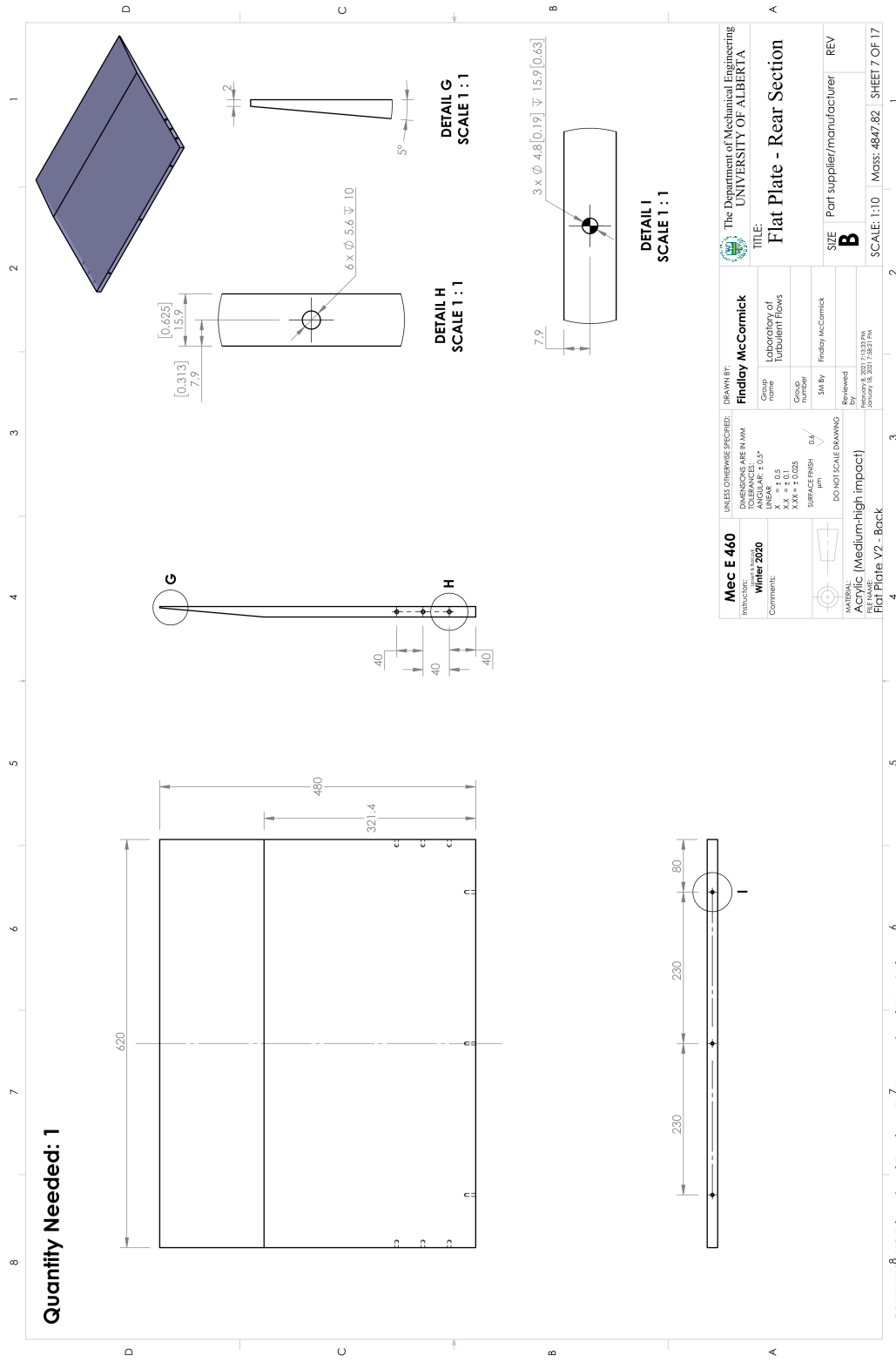


DETAIL V  
SCALE 2 : 1

SECTION U-U

<b>Mec E 460</b> INTRODUCTION: Winter 2020 Comment:		UNLESS OTHERWISE SPECIFIED: DIMENSIONS ARE IN MM DECIMALS ARE TO 0.5° ANGLES ARE TO 5° LINEAR ± 0.5 XX ± 1.0 XXX ± 1.0/25 SURFACE FINISH: 0.6 µm DO NOT SCALE DRAWING		DRAWN BY: <b>Findlay McCormick</b> Class name: Laboratory of Turbulent Flows Group number: SW By: Findlay McCormick Reviewed By: January 28, 2021 10:14 AM		The Department of Mechanical Engineering UNIVERSITY OF ALBERTA TITLE: <b>Flat Plate Assembly</b> SIZE: Part supplier/manufacturer <b>B</b> SCALE: 1:10 Mass: 16448.28 SHEET 3 OF 17	
FILE NAME: <b>16448_28</b> Flat Plate V2 - Assembly (Solid Insert)							

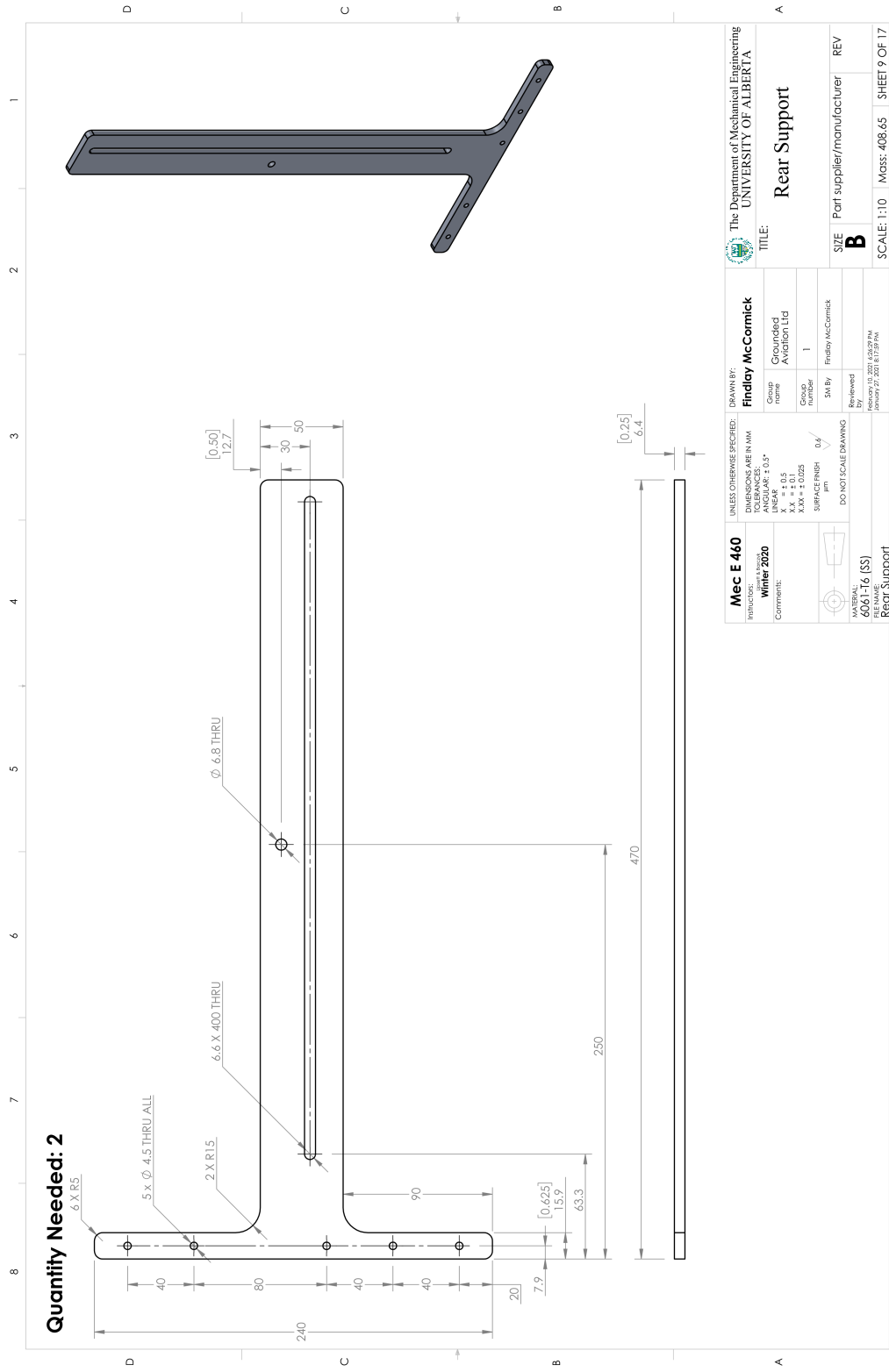




<b>Mec E 460</b>		UNLESS OTHERWISE SPECIFIED:		DRAWN BY:		The Department of Mechanical Engineering UNIVERSITY OF ALBERTA	
INTRODUCTION:		DIMENSIONS ARE IN MM		Findlay McCormick		TITLE:	
Winter 2020		TOLERANCES		Name		Flat Plate - Rear Section	
Comment:		ANGLES: 0.5°		Laboratory of Turbulent Flows		SIZE	
		LINEAR: ± 0.5		Group number		Part supplier/manufacturer	
		XX: ± 1.0		SW By		REV	
		SURFACE FINISH: 0.6 μm		Findlay McCormick		B	
		DO NOT SCALE DRAWING		Reviewed		SCALE: 1:10	
				By		Mass: 4847.82	
				January 18, 2021 7:38:21 PM		SHEET 7 OF 17	
				FILE NAME			
				Flat Plate V2 - Back			

SOLIDWORKS Educational Product. For Instructional Use Only.





**Mec E 460**  
 Manufacturer: Winter 2020  
 Comment: 

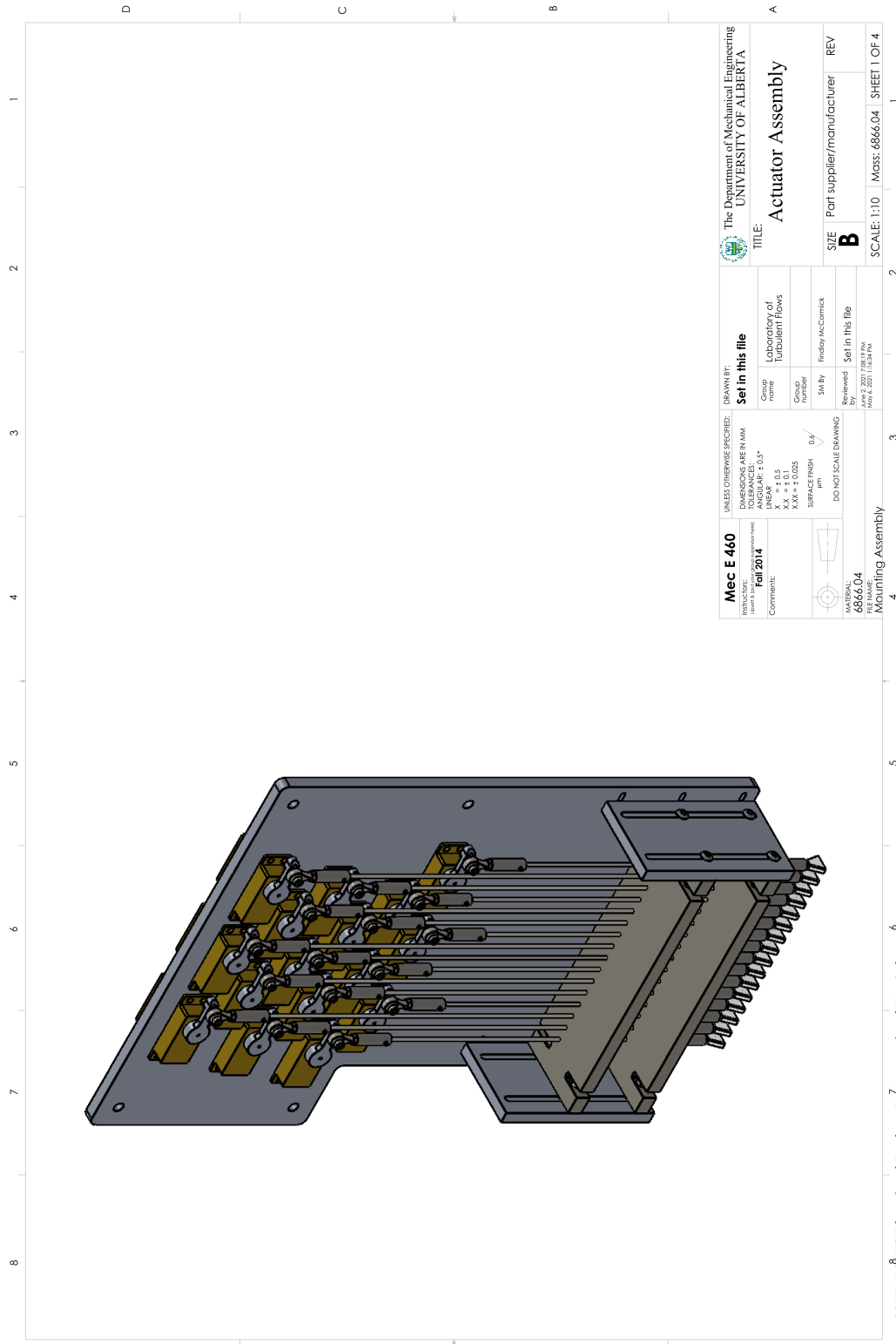
**Findley McCormick**  
 Company name: Grounded Aviation Ltd  
 Group number: 1  
 SW By: Findley McCormick

UNLESS OTHERWISE SPECIFIED:  
 DIMENSIONS ARE IN MM  
 DECIMALS ARE TO 0.15°  
 LINEAR TOLERANCES:  
 XX = ± 0.5  
 XX = ± 0.025  
 SURFACE FINISH: 0.6 µm  
 DO NOT SCALE DRAWING

DATE: 27/01/2021 6:02:39 AM  
 FILE NAME: 406116 (SS)  
 REAR SUPPORT

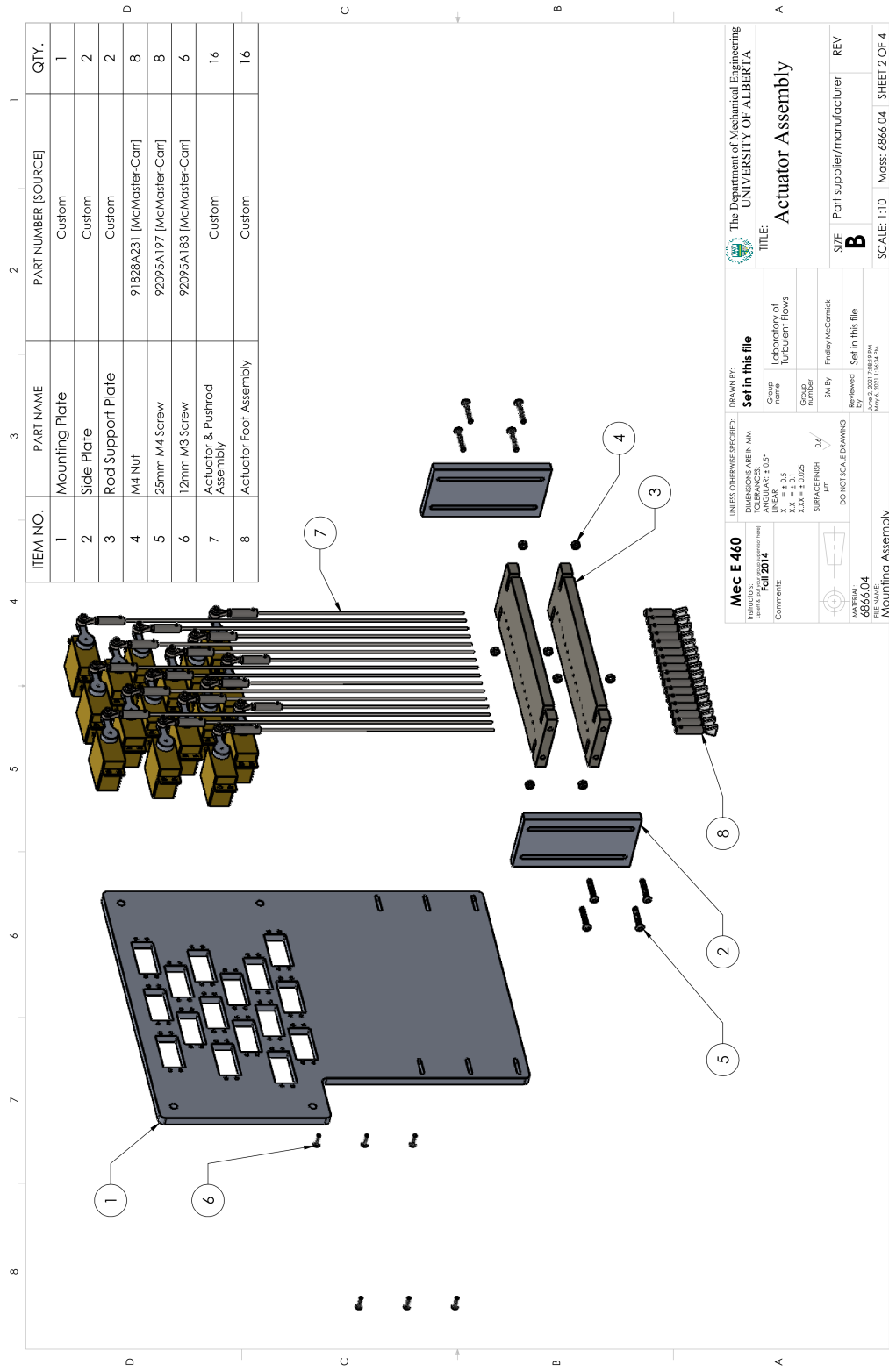
THE UNIVERSITY OF ALBERTA  
 TITLE: Rear Support  
 SIZE: Part supplier/manufacturer  
 REV: B

SCALE: 1:10 Mass: 408.65 SHEET 9 OF 17



<b>Mec E 460</b> MTD/CAD CODE: Mec E 460 Version: 1.0 Date: Fall 2014 Comment:	UNLESS OTHERWISE SPECIFIED: DIMENSIONS ARE IN MM DECIMALS: 0.5 FRACTIONS: 1/16" TOLERANCES: LINEAR: ± 0.1 ANGLES: ± 0.5 SURFACE FINISH: 0.8 µm DO NOT SCALE DRAWING	DRAWN BY: <b>Set in this file</b> Check name: Laboratory of Turbulent Flows Group number: Frutley McComick SW By: Frutley McComick Reviewed: Set in this file Date: 2021-11-08 PM File Name: Mec E 460.dwg	The Department of Mechanical Engineering UNIVERSITY OF ALBERTA	TITLE: <b>Actuator Assembly</b>
				SIZE: Part supplier/manufacturer <b>B</b>
FILE NAME: 6866.04 Mounting Assembly				SCALE: 1:10 Mass: 6866.04 SHEET 1 OF 4

SOLIDWORKS Educational Product. For Instructional Use Only.



ITEM NO.	PART NAME	PART NUMBER [SOURCE]	QTY.
1	Mounting Plate	Custom	1
2	Side Plate	Custom	2
3	Rod Support Plate	Custom	2
4	M4 Nut	91828A231 [McMaster-Carr]	8
5	25mm M4 Screw	92095A197 [McMaster-Carr]	8
6	12mm M3 Screw	92095A183 [McMaster-Carr]	6
7	Actuator & Pushrod Assembly	Custom	16
8	Actuator Foot Assembly	Custom	16

**Mec E 460**  
 INTRODUCTION: **Fall 2014**  
 COMMENTS:

UNLESS OTHERWISE SPECIFIED:  
 DIMENSIONS ARE IN MM  
 DECIMALS ARE IN 0.5°  
 TOLERANCES:  
 LINEAR ± 0.5  
 ANGULAR ± 0.5  
 SURFACE FINISH: 0.8 μm  
 DO NOT SCALE DRAWING

FILE NAME: 6866.04  
 MOUNTING ASSEMBLY

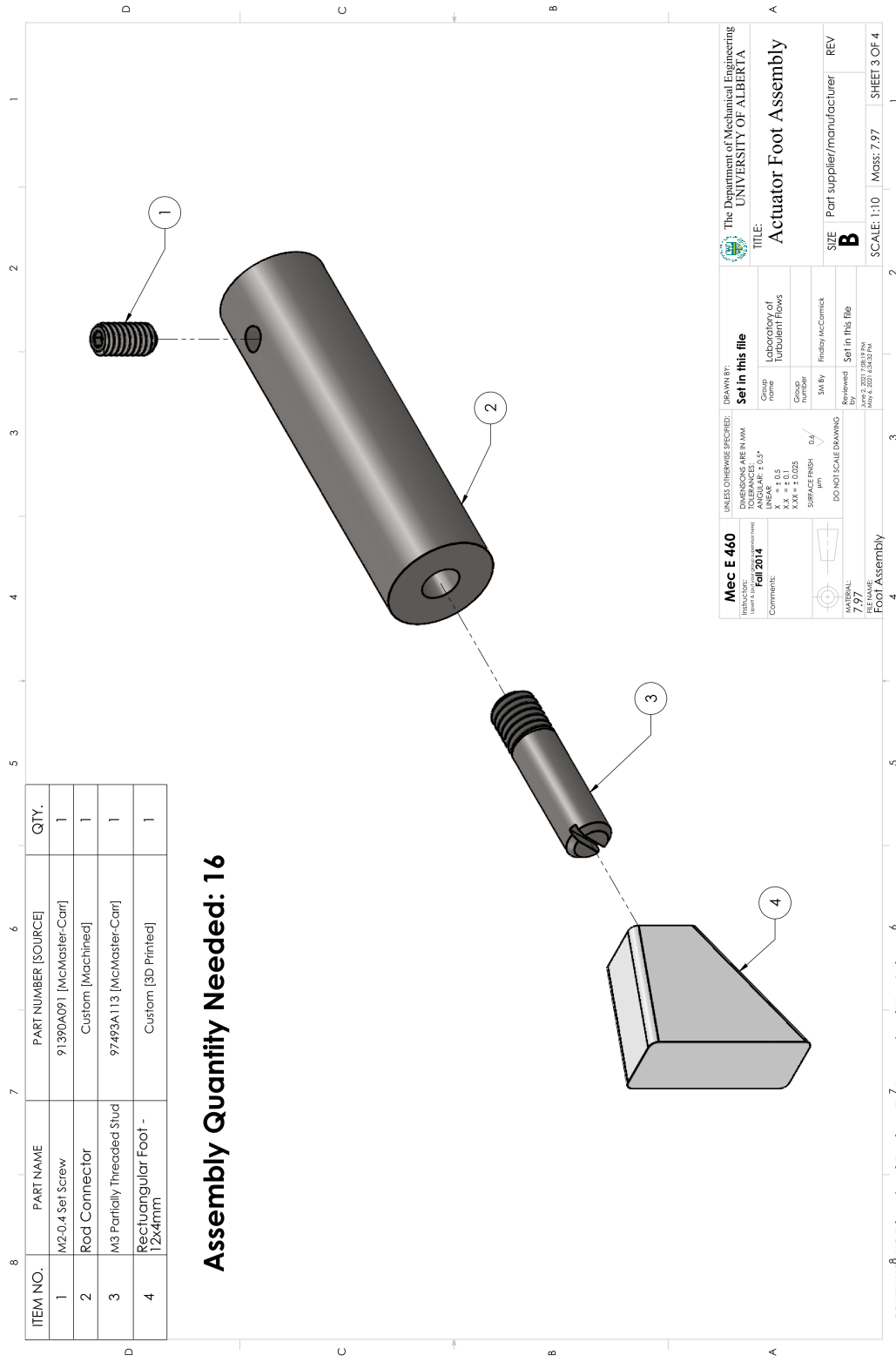
DRAWN BY: **Set in this file**  
 Check name: Laboratory of Turbulent Flows  
 Group number: Frisby McCormick  
 SW By: Frisby McCormick  
 Reviewed: **Set in this file**  
 Date: 2021/10/24 PM

UNIVERSITY OF ALBERTA  
 The Department of Mechanical Engineering  
 TITLE: **Actuator Assembly**

SIZE: Part supplier/manufacturer  
 REV: **B**

SCALE: 1:10 Mass: 6866.04 SHEET 2 OF 4

SOLIDWORKS Educational Product. For Instructional Use Only.



ITEM NO.	PART NAME	PART NUMBER [SOURCE]	QTY.
1	M2-0.4 Set Screw	91390A091 [McMaster-Carr]	1
2	Rod Connector	Custom [Machined]	1
3	M3 Partially Threaded Stud	97493A113 [McMaster-Carr]	1
4	Rectangular Foot - 12x4mm	Custom [3D Printed]	1

**Assembly Quantity Needed: 16**

**Mec E 460**  
 MACHINING LABORATORY  
 Fall 2014  
 Comment: 

UNLESS OTHERWISE SPECIFIED:  
 DIMENSIONS ARE IN MM  
 DECIMALS ARE IN 0.05  
 ANGLES ARE IN 0.5°  
 LINEAR ± 0.3  
 XX ± 0.05  
 XX ± 0.025  
 SURFACE FINISH: 0.6  
 µm  
 DO NOT SCALE DRAWING

DRAWN BY: **Set in this file**  
 Check name: Laboratory of Turbulent Flows  
 Group number: Frisby McComick  
 SW By: Frisby McComick  
 Reviewed: Set in this file  
 Date: 2021-03-27 PM  
 File Name: Foot Assembly

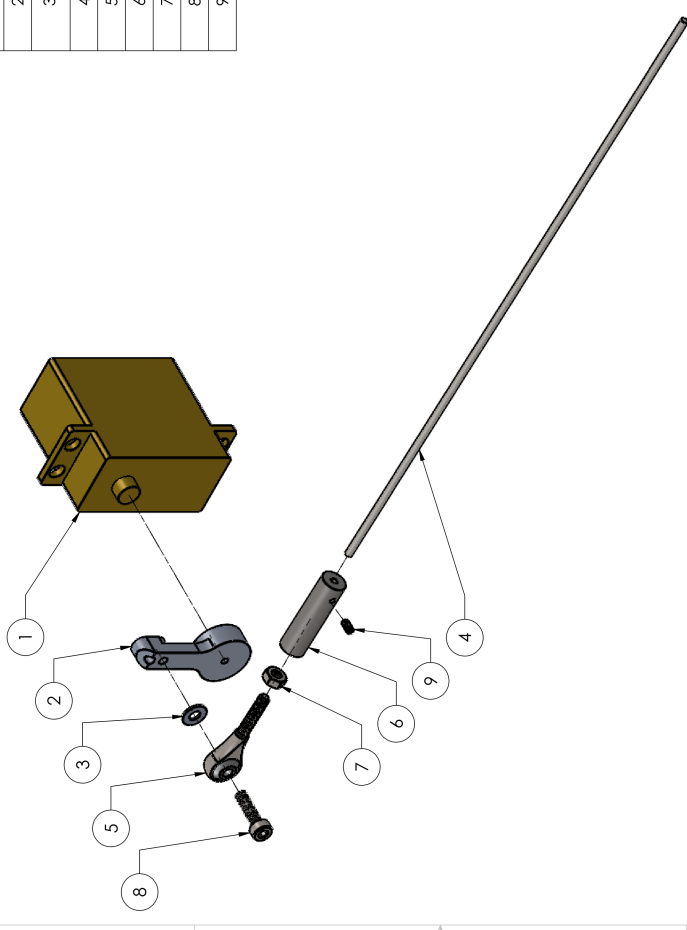
DATE: **7 97**  
 FILE NAME: Foot Assembly

UNIVERSITY OF ALBERTA  
 The Department of Mechanical Engineering  
 TITLE: **Actuator Foot Assembly**  
 SIZE: Part supplier/manufacturer  
 REV: **B**  
 SCALE: 1:10 Mass: 7.97 SHEET 3 OF 4

SOLIDWORKS Educational Product. For Instructional Use Only.

ITEM NO.	PART NAME	PART NUMBER [SOURCE]	QTY.
1	Servo Stand in	SH1290MG [Savox]	1
2	Servo Arm	[Amazon]	1
3	0.5mm Spacer Washer	90718A 120 [McMaster-Carr]	1
4	Flexible Rod [200]	Custom	1
5	M3 Rod End	59935K11 [McMaster-Carr]	1
6	Rod Connector	Custom	1
7	M3 Nut	90592A085 [McMaster-Carr]	1
8	12mm M3 Screw	90751A 113 [McMaster-Carr]	1
9	M2-0.4 Set Screw	91390A091 [McMaster-Carr]	1

### Assembly Quantity Needed: 16



**Mec E 460**  
 Introduction to Mechanical Engineering  
 Fall 2014  
 Comments:

UNLESS OTHERWISE SPECIFIED:  
 DIMENSIONS ARE IN MM  
 DECIMALS: 0.5, 1, 2, 5  
 ANGLES: 0.5°, 1°, 1.5°  
 LINEAR: 0.5, 1, 1.5  
 XX = ± 0.025  
 SURFACE FINISH: 0.8  
 µm  
 DO NOT SCALE DRAWING

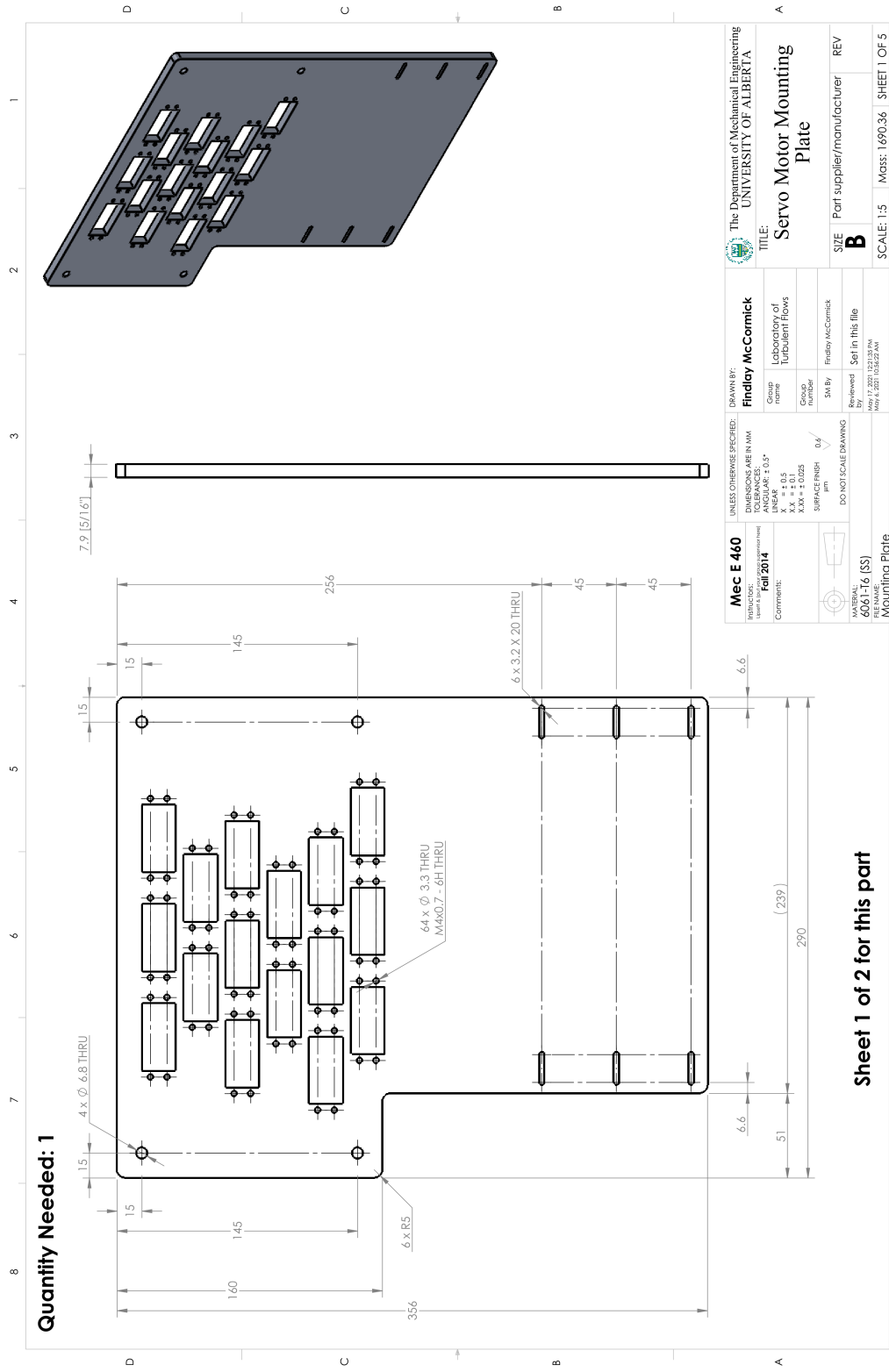
DRAWN BY:  
**Set in this file**  
 Class name: Laboratory of Turbulent Flows  
 Group number: Frutley McComick  
 SW By: Frutley McComick  
 Reviewed: Set in this file  
 Date: 2021-03-08 PM

The Department of Mechanical Engineering  
 UNIVERSITY OF ALBERTA

TITLE:  
**Actuator & Pushrod Assembly**

SIZE: Part supplier/manufacturer  
**B**

SCALE: 1:10 Mass: 282.75 SHEET 4 OF 4

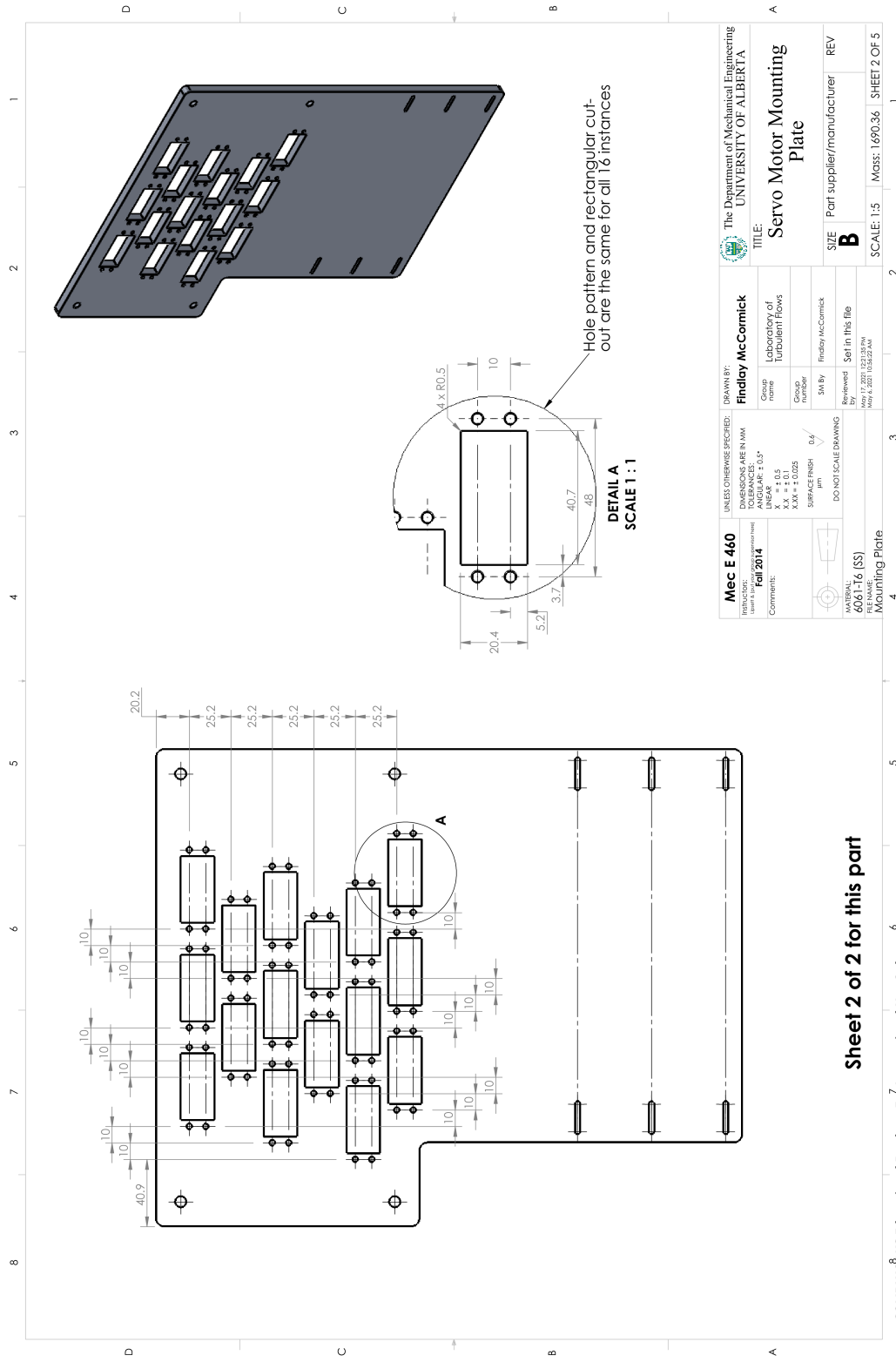


Quantity Needed: 1

Sheet 1 of 2 for this part

<b>Mec E 460</b> <small>MECHANICAL ENGINEERING</small> LABORATORY OF TURBULENT FLOWS Fall 2014 Comments:		DRAWN BY: <b>Findlay McCormick</b> Group Number: SW By: Friday McCormick	The Department of Mechanical Engineering UNIVERSITY OF ALBERTA
UNLESS OTHERWISE SPECIFIED: DIMENSIONS ARE IN MM DECIMALS ARE TO 0.15" TOLERANCES: LINEAR ± 0.15 ANGULAR ± 0.5 SURFACE FINISH: 0.8 µm DO NOT SCALE DRAWING		TITLE: <b>Servo Motor Mounting Plate</b> SIZE: Part supplier/manufacturer REV: <b>B</b>	SCALE: 1:5 Mass: 1690.36 SHEET 1 OF 5
FILE NAME: <b>406116 (SS)</b> Mounting Plate		Reviewed By: Set in this file May 17, 2017 10:22:27 AM	

SOLIDWORKS Educational Product For Instructional Use Only.



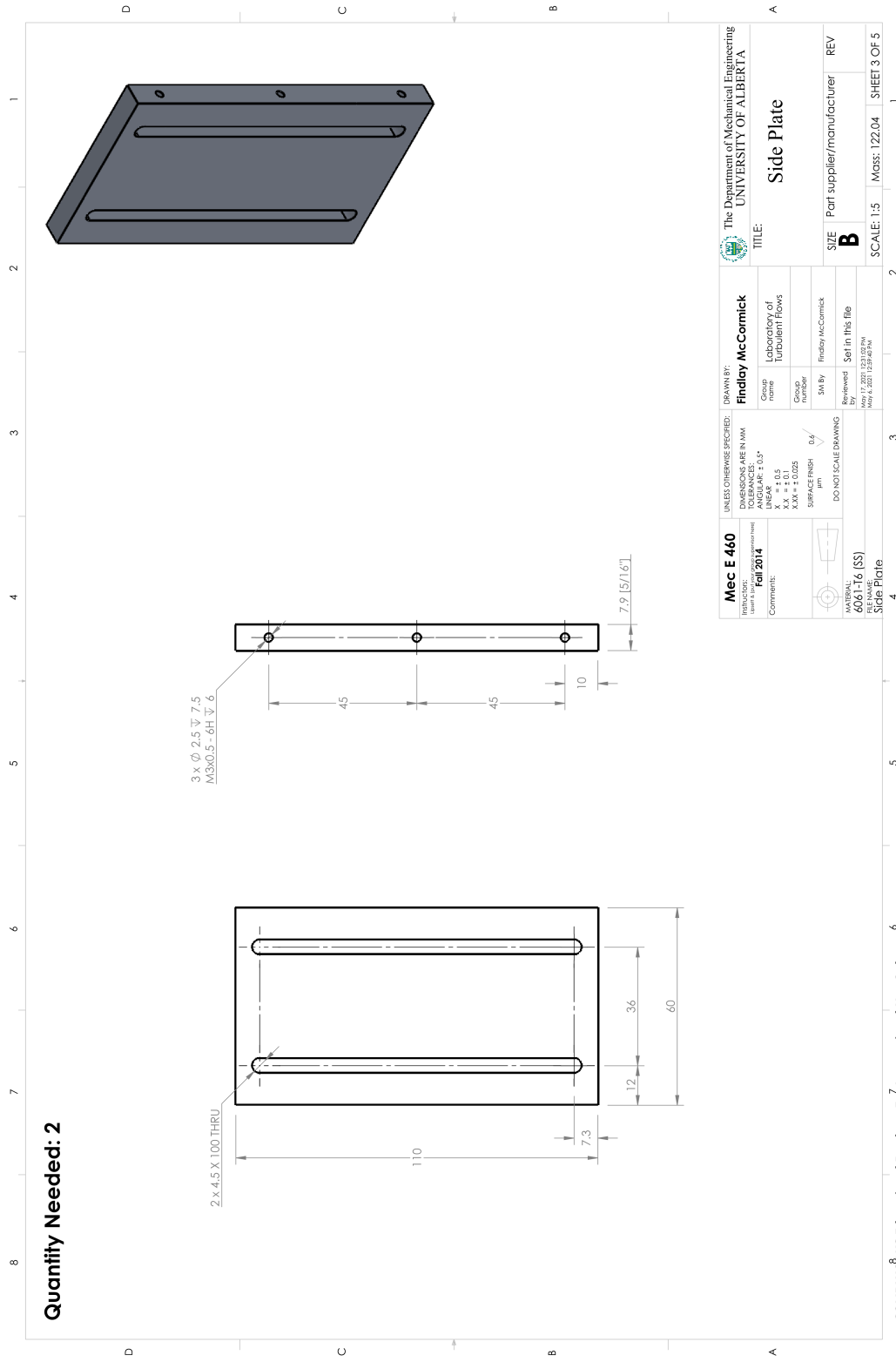
Hole pattern and rectangular cut-out are the same for all 16 instances

**DETAIL A**  
SCALE 1 : 1

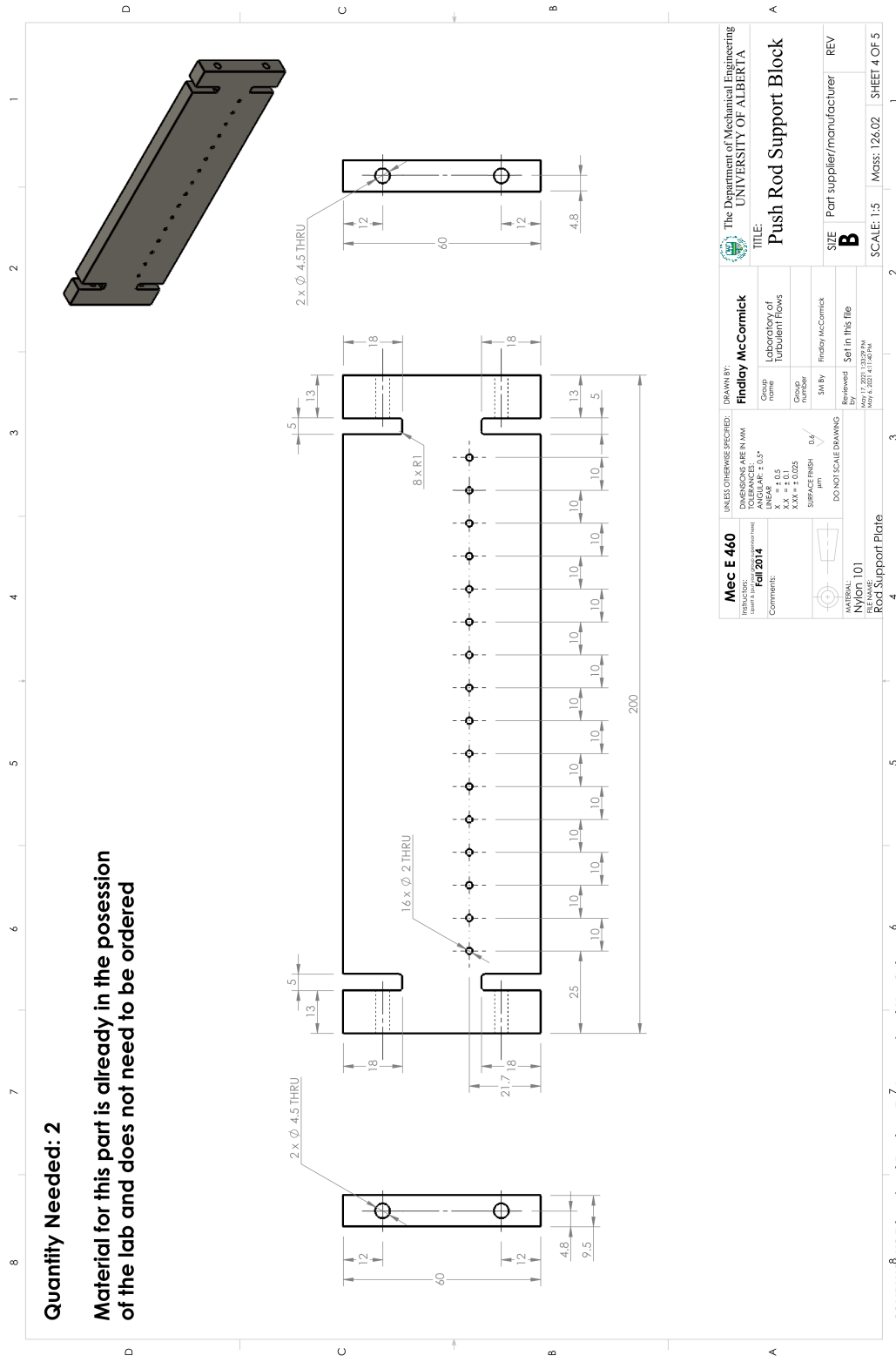
Sheet 2 of 2 for this part

<b>Mec E 460</b> MFG CODE: Fall 2014 Comment:	UNLESS OTHERWISE SPECIFIED: DIMENSIONS ARE IN MM DECIMALS: 0.5 LINEAR: 0.5 XX = ± 0.5 XXX = ± 0.025 SURFACE FINISH: 0.8 µm DO NOT SCALE DRAWING	DRAWN BY: <b>Findley McCormick</b> Class name: Laboratory of Turbulent Flows Group number: SW By: Findley McCormick	The Department of Mechanical Engineering UNIVERSITY OF ALBERTA
	TITLE: <b>Servo Motor Mounting Plate</b> SIZE: Part supplier/manufacturer <b>B</b> SCALE: 1:5 Mass: 1.69036 SHEET 2 OF 5	Reviewed: Set in this file May 19, 2021 10:22:27 AM	REV

SOLIDWORKS Educational Product. For Instructional Use Only.

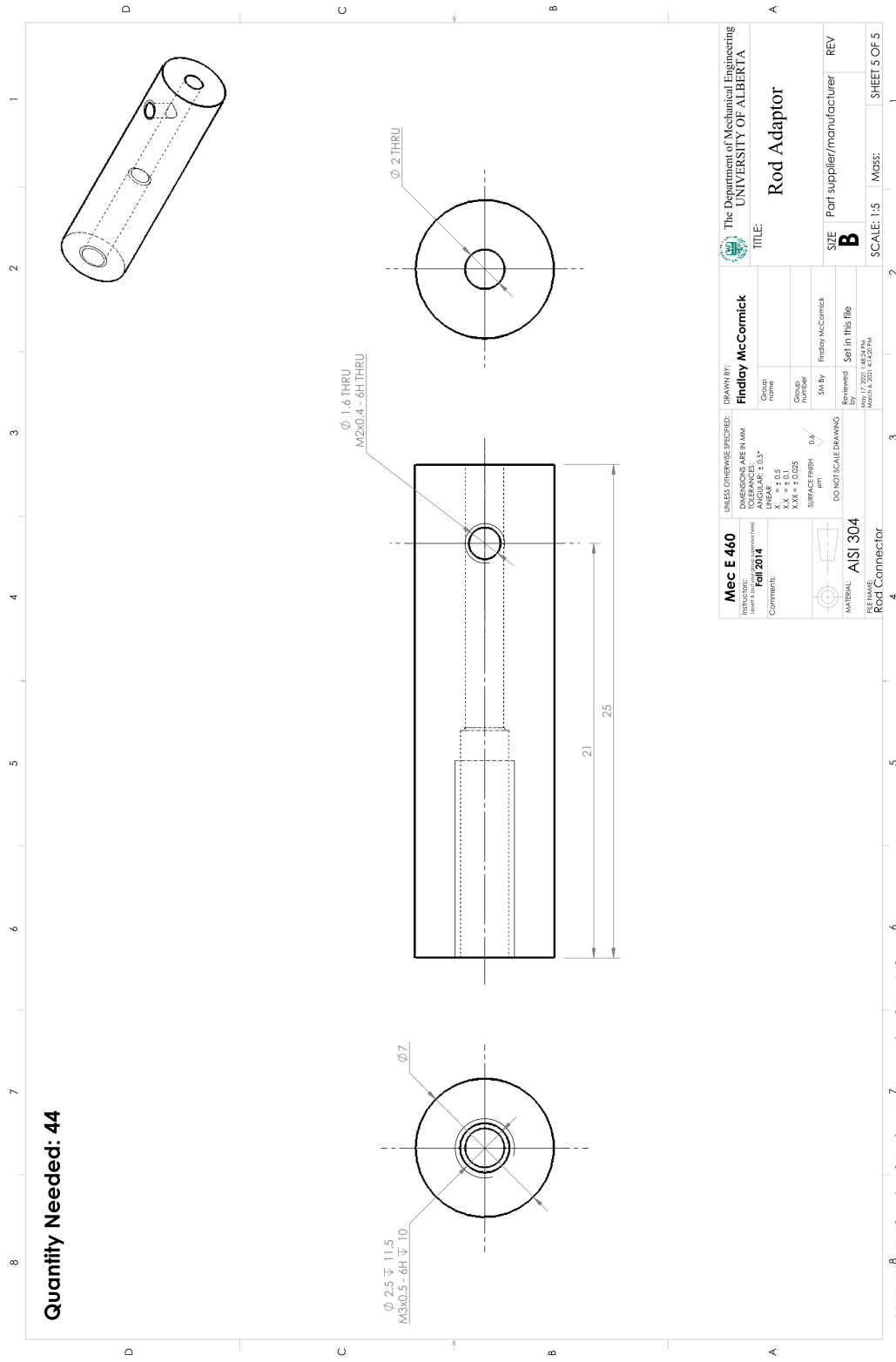


<b>Mec E 460</b> MFG PART NO: 460E16 (SS) REV: 1 FILE NAME: Side Plate		UNLESS OTHERWISE SPECIFIED: DIMENSIONS ARE IN MM DECIMALS ARE TO 0.15" ANGLES ARE 0.5° LINEAR TOLERANCES: XX = ± 0.1 XX = ± 0.025 SURFACE FINISH: 0.8 μm DO NOT SCALE DRAWING		DRAWN BY: <b>Finlay McCormick</b> Check name: Laboratory of Turbulent Flows Group number: Frinlay McCormick SW By: Set in this file Reviewed by: May 11, 2021 12:59:48 PM		The Department of Mechanical Engineering UNIVERSITY OF ALBERTA <b>Side Plate</b> SIZE: Part supplier/manufacturer REV: B SCALE: 1:5 Mass: 122.04 SHEET 3 OF 5	
---	--	---	--	--	--	--	--



**Quantity Needed: 2**

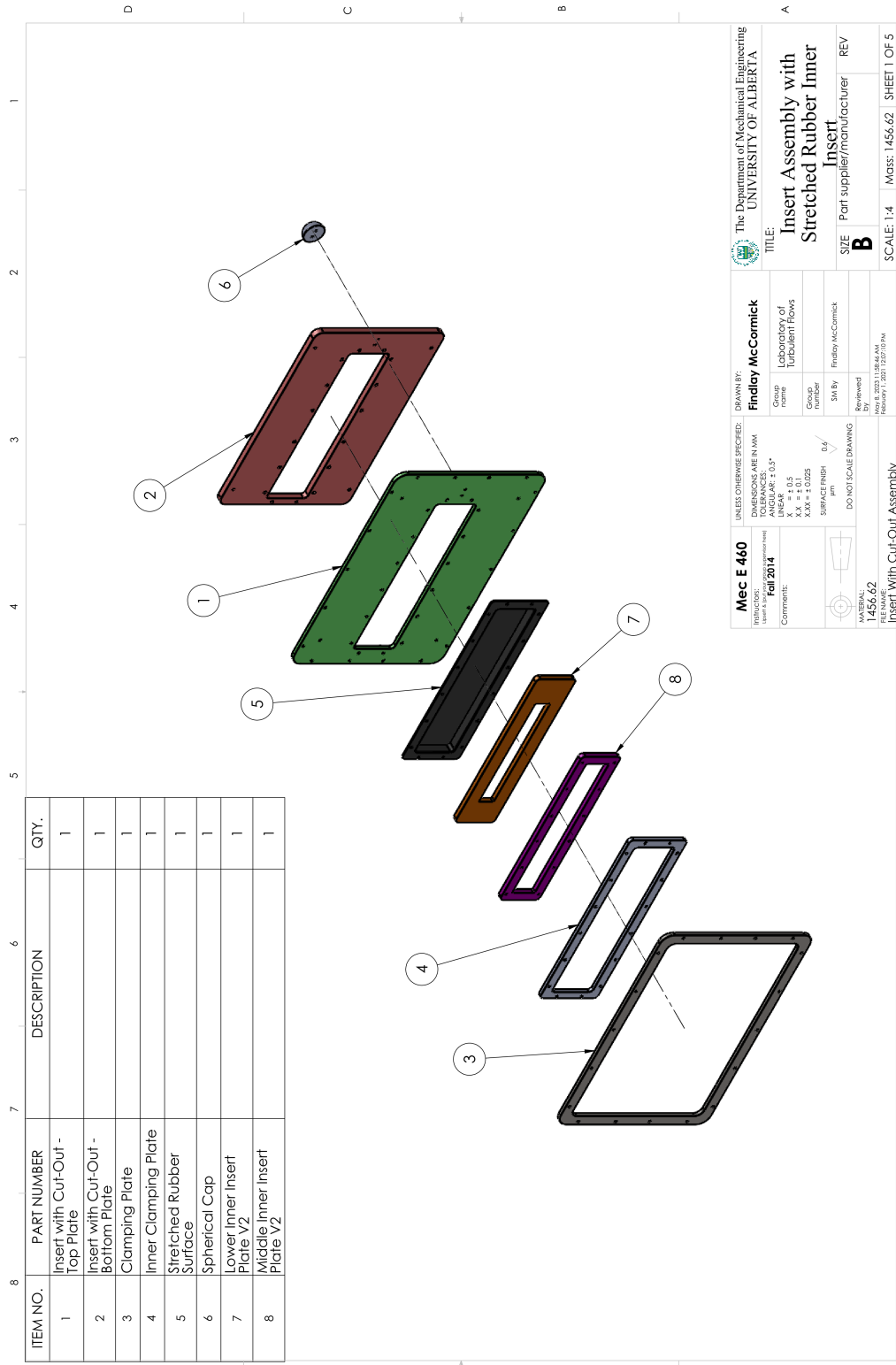
**Material for this part is already in the possession of the lab and does not need to be ordered**



Quantity Needed: 44

<b>Mec E 460</b> MESH CODE: Version: 1.0 Fall 2014 Comment:		UNLESS OTHERWISE SPECIFIED: DIMENSIONS ARE IN MM DECIMALS ARE TO 0.1 ANGLES ARE TO 0.5° LINEAR TOLERANCES: XX = ± 0.5 XX = ± 0.1 XX = ± 0.025 SURFACE FINISH: 0.8 µm DO NOT SCALE DRAWING		DRAWN BY: <b>Findlay McCormick</b> Check Name: Group Number: SW By: Findlay McCormick Reviewed: Set in This File Date: Mon 11/20/14 4:02:34 PM		The Department of Mechanical Engineering UNIVERSITY OF ALBERTA <b>Rod Adaptor</b> TITLE:	
MATERIAL: <b>AlSi 304</b> Rod Connector		SIZE: Part supplier/manufacturer <b>B</b>		SCALE: 1:5 Mass:		SHEET 5 OF 5	

SOLIDWORKS Educational Product For Instructional Use Only.



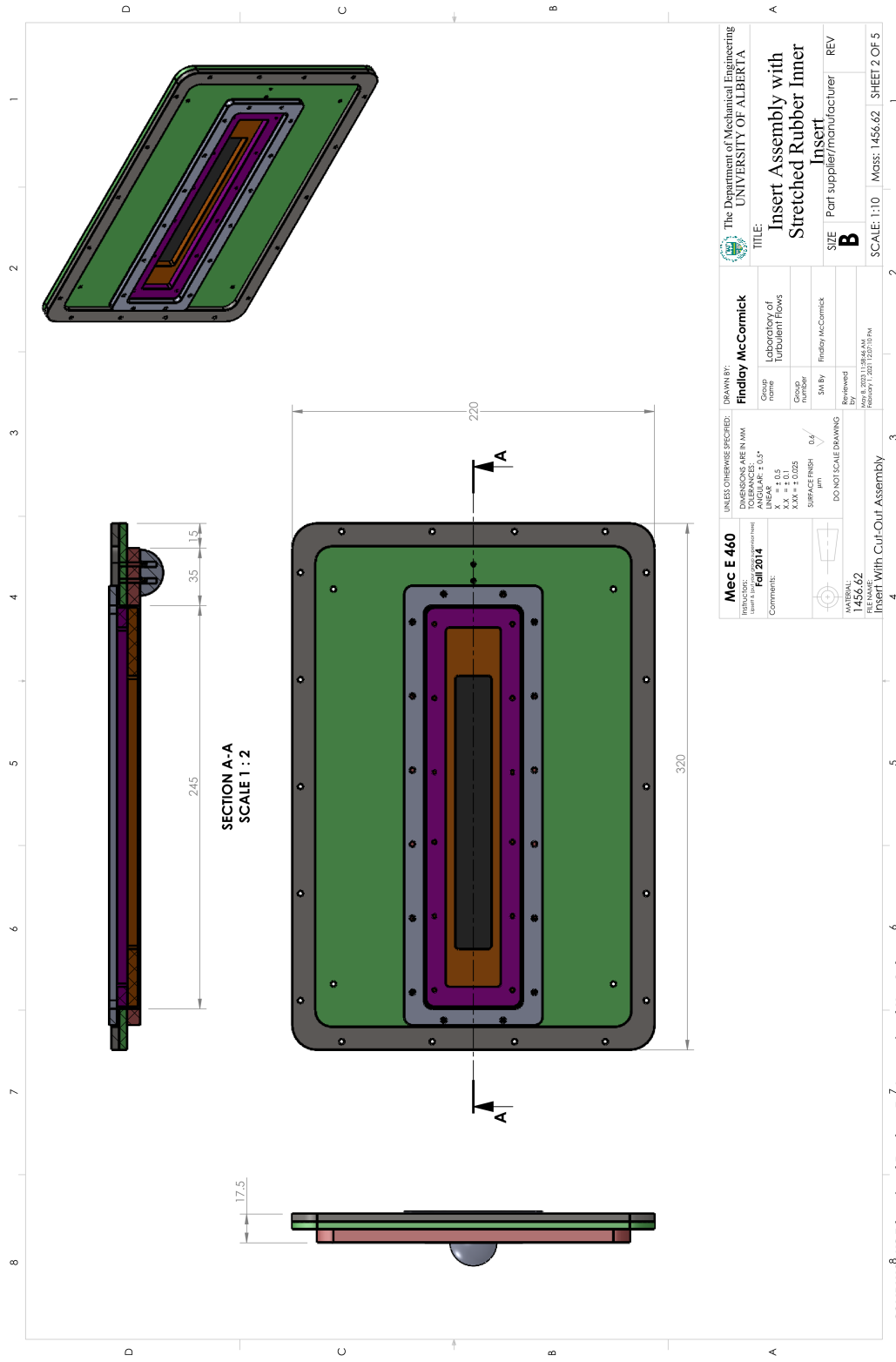
ITEM NO.	PART NUMBER	DESCRIPTION	QTY.
1	Insert with Cut-Out - Top Plate		1
2	Insert with Cut-Out - Bottom Plate		1
3	Clamping Plate		1
4	Inner Clamping Plate		1
5	Stretched Rubber Surface		1
6	Spherical Cap		1
7	Lower Inner Insert Plate V2		1
8	Middle Inner Insert Plate V2		1

**Mec E 460**  
 Version: 1.0  
 Date: Fall 2014  
 Comment:   
 UNLESS OTHERWISE SPECIFIED:  
 DIMENSIONS ARE IN MM  
 DECIMALS ARE TO 0.05  
 TOLERANCES:  
 LINEAR ± 0.15  
 ANGULAR ± 0.5  
 SURFACE FINISH: 0.8 μm  
 DO NOT SCALE DRAWING

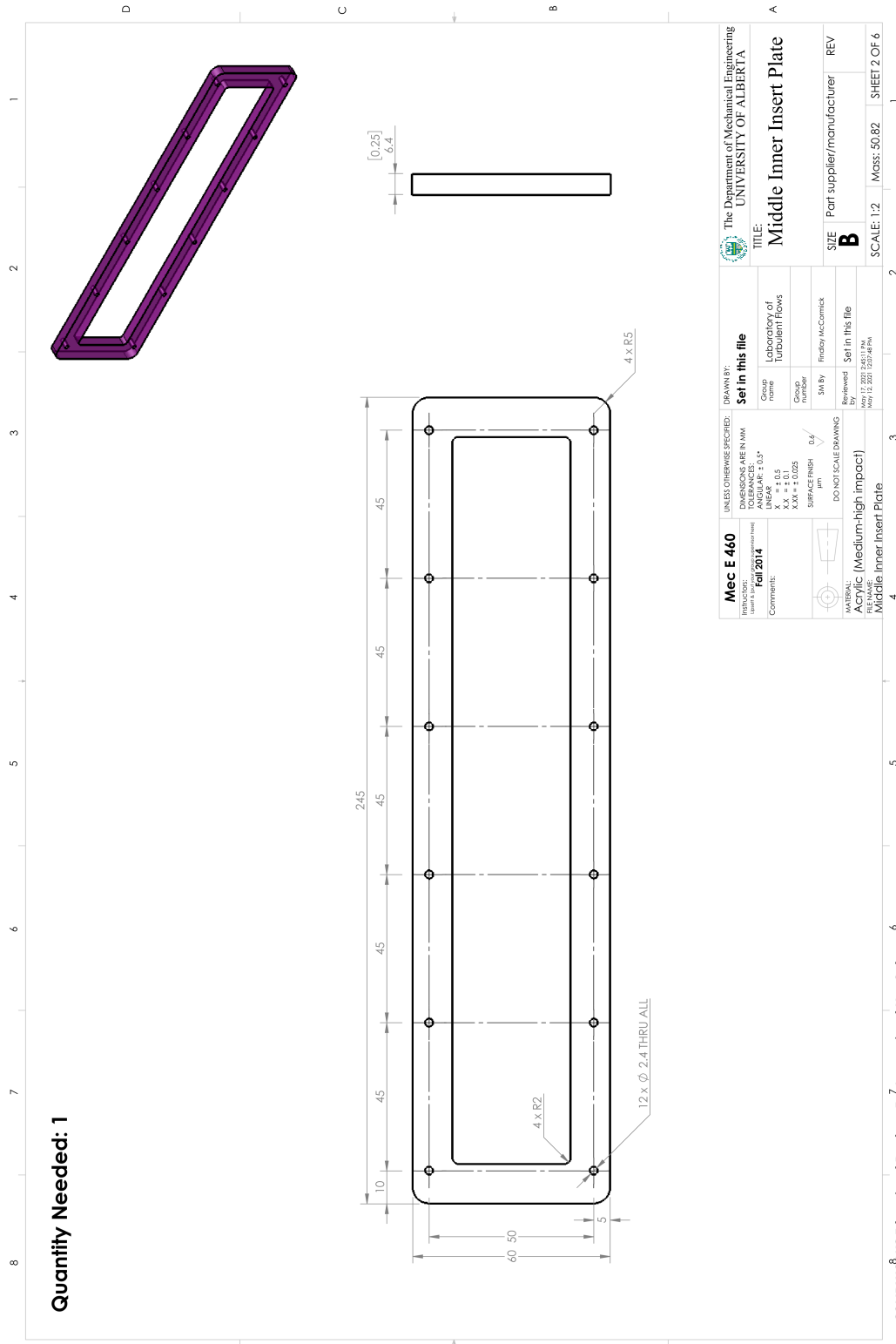
**Findley McCormick**  
 Company Name: Laboratory of Turbulent Flows  
 Group Number:   
 SW By: Findley McCormick  
 Drawn By:   
 Checked By:   
 Approved By:   
 Date: 1456.62  
 File Name: Insert With Cut-Out Assembly

**UNIVERSITY OF ALBERTA**  
 TITLE: **Insert Assembly with Stretched Rubber Inner Insert**  
 SIZE: Part supplier/manufacturer  
 REV: **B**  
 SCALE: 1:4 Mass: 1456.62 SHEET 1 OF 5

SOLIDWORKS Educational Product. For Instructional Use Only.



<b>Mec E 460</b> Meca Code: <b>Fall 2014</b> Comment:		UNLESS OTHERWISE SPECIFIED: DIMENSIONS ARE IN MM SURFACE FINISH: 0.8 TOLERANCES: 0.15° LINEAR: ± 0.3 ANGLES: ± 0.1 SURFACE FINISH: 0.8 DO NOT SCALE DRAWING		DRAWN BY: <b>Findlay McCormick</b> Name: Laboratory of Turbulent Flows Group: Number: SW By: Findlay McCormick Reviewed By: Findlay McCormick Date: 14/05/2014 12:52:01 PM File Name: <b>1456.62</b> Insert With Cut-Out Assembly	
The Department of Mechanical Engineering UNIVERSITY OF ALBERTA		TITLE: <b>Insert Assembly with Stretched Rubber Inner</b>		SIZE: Part supplier/manufacturer <b>B</b> SCALE: 1:10 Mass: 1456.62 SHEET 2 OF 5	

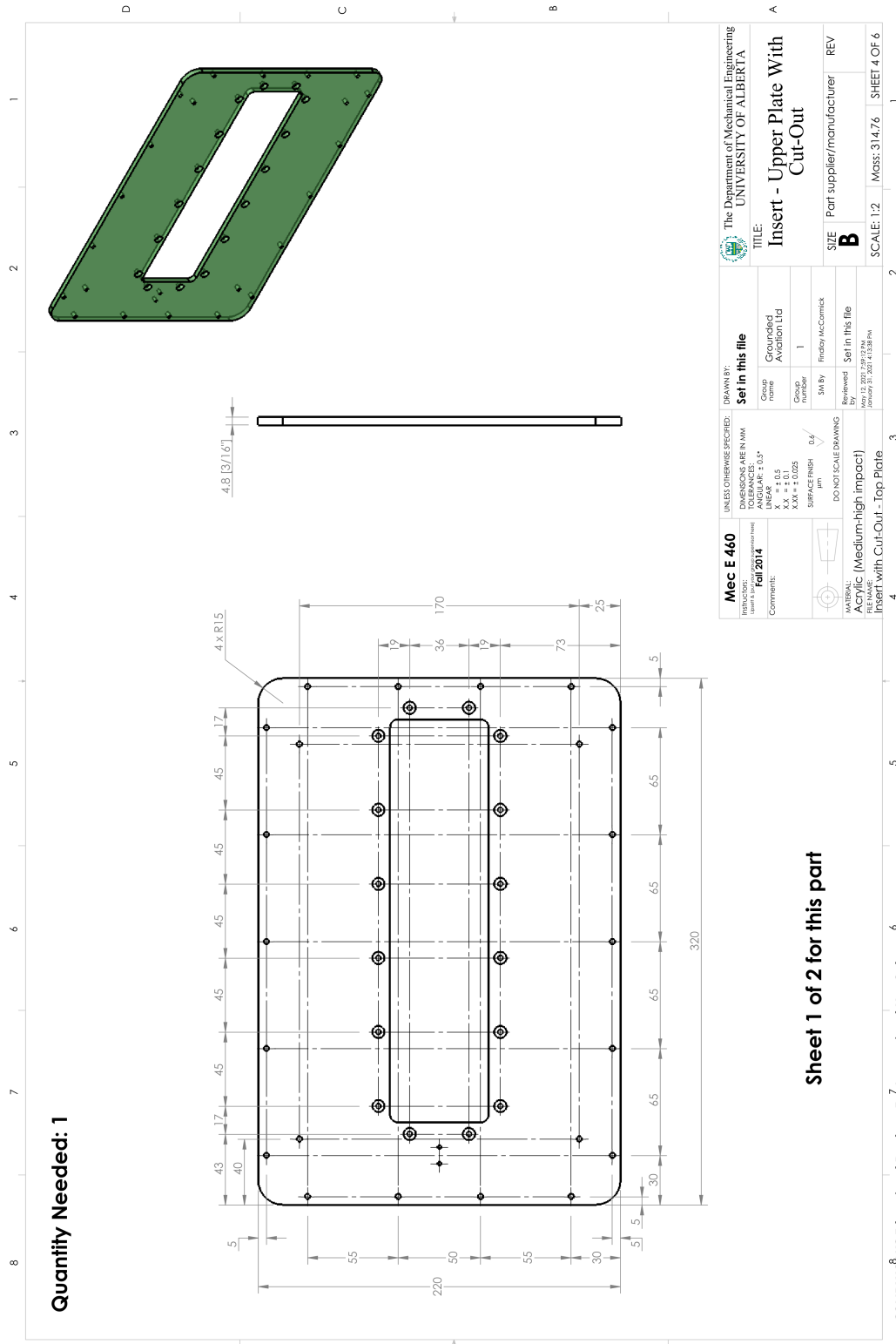


Quantity Needed: 1

<b>Mec E 460</b> MFG CODE: <b>MEC E 460</b> Revision: <b>Fall 2014</b> Comment:		UNLESS OTHERWISE SPECIFIED: DIMENSIONS ARE IN MM DECIMALS ARE TO 0.15" TOLERANCES: LINEAR ± 0.3 ANGULAR ± 0.5 SURFACE FINISH: 0.8 μm DO NOT SCALE DRAWING		DRAWN BY: <b>Set in this file</b> Class name: Laboratory of Turbulent Flows Group number: Friday McComick SW By: Set in this file Reviewed By: Set in this file Date: May 12, 2022 12:50:48 PM		The Department of Mechanical Engineering UNIVERSITY OF ALBERTA	
TITLE: <b>Middle Inner Insert Plate</b>		SIZE: Part supplier/manufacturer <b>B</b>		SCALE: 1:2 Mass: 50.82 SHEET 2 OF 6			

SOLIDWORKS Educational Product For Instructional Use Only.

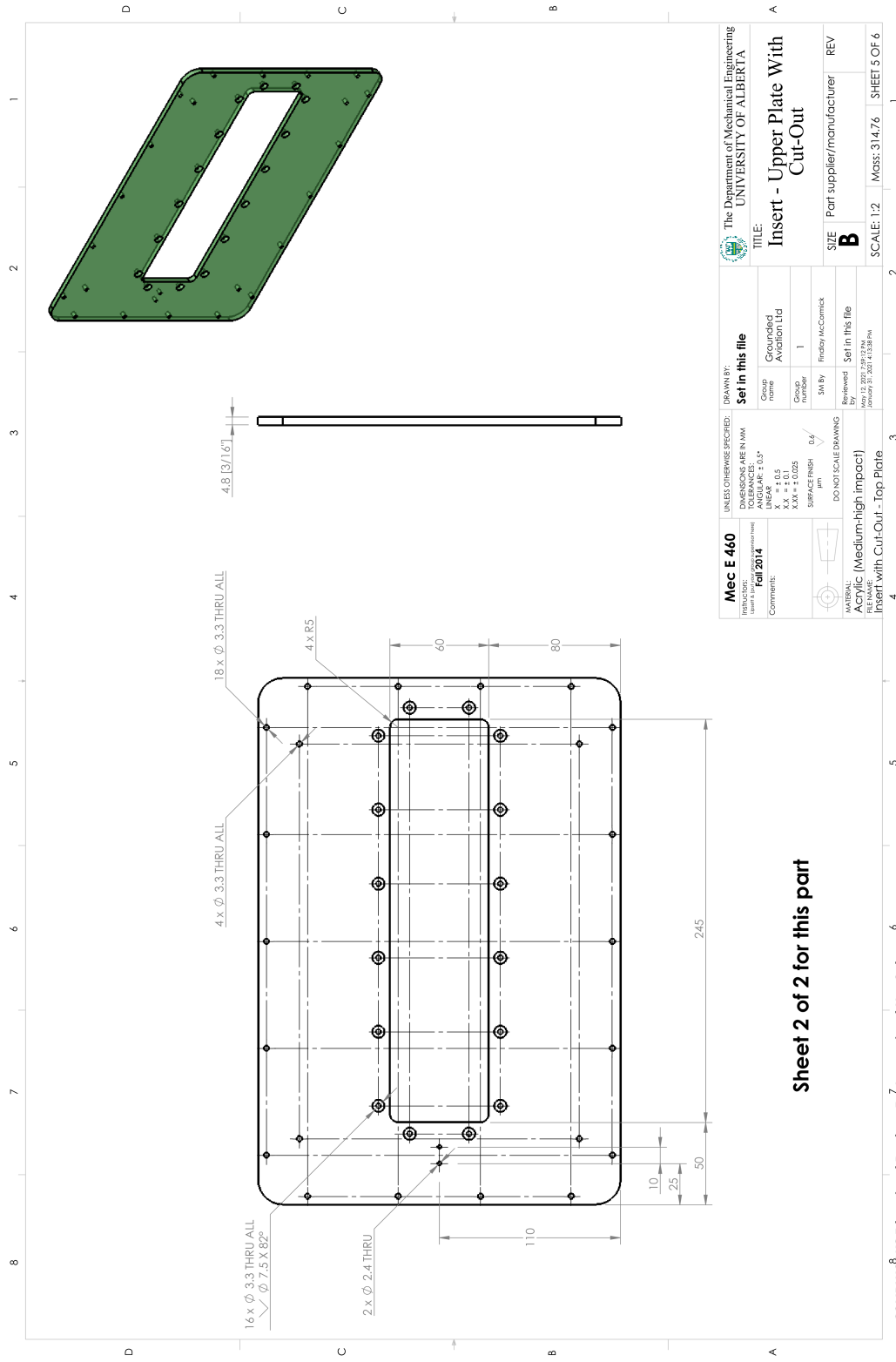




Quantity Needed: 1

Sheet 1 of 2 for this part

SOLIDWORKS Educational Product. For Instructional Use Only.



Sheet 2 of 2 for this part

**Mec E 460**  
 WINDUP CODE:   
 PART NUMBER: **Fall 2014**  
 COMMENTS:   
 DO NOT SCALE DRAWING

UNLESS OTHERWISE SPECIFIED:  
 DIMENSIONS ARE IN MM  
 DECIMALS ARE TO 0.1  
 LINEAR ± 0.15  
 ANGLES ± 0.5°  
 X.X ± 0.1  
 X.XX ± 0.025  
 SURFACE FINISH: 0.6  $\mu$ m

DRAWN BY: **Set in this file**  
 COMPANY NAME: **Grounded Aviation Ltd**  
 GROUP NUMBER: **1**  
 SW BY: **Friday McCormick**

REVIEWED BY: **Set in this file**  
 DATE: **2014.09.23 11:38 AM**

FILE NAME: **Acrylic (Medium-High Impact) Insert with Cut-Out - Top Plate**

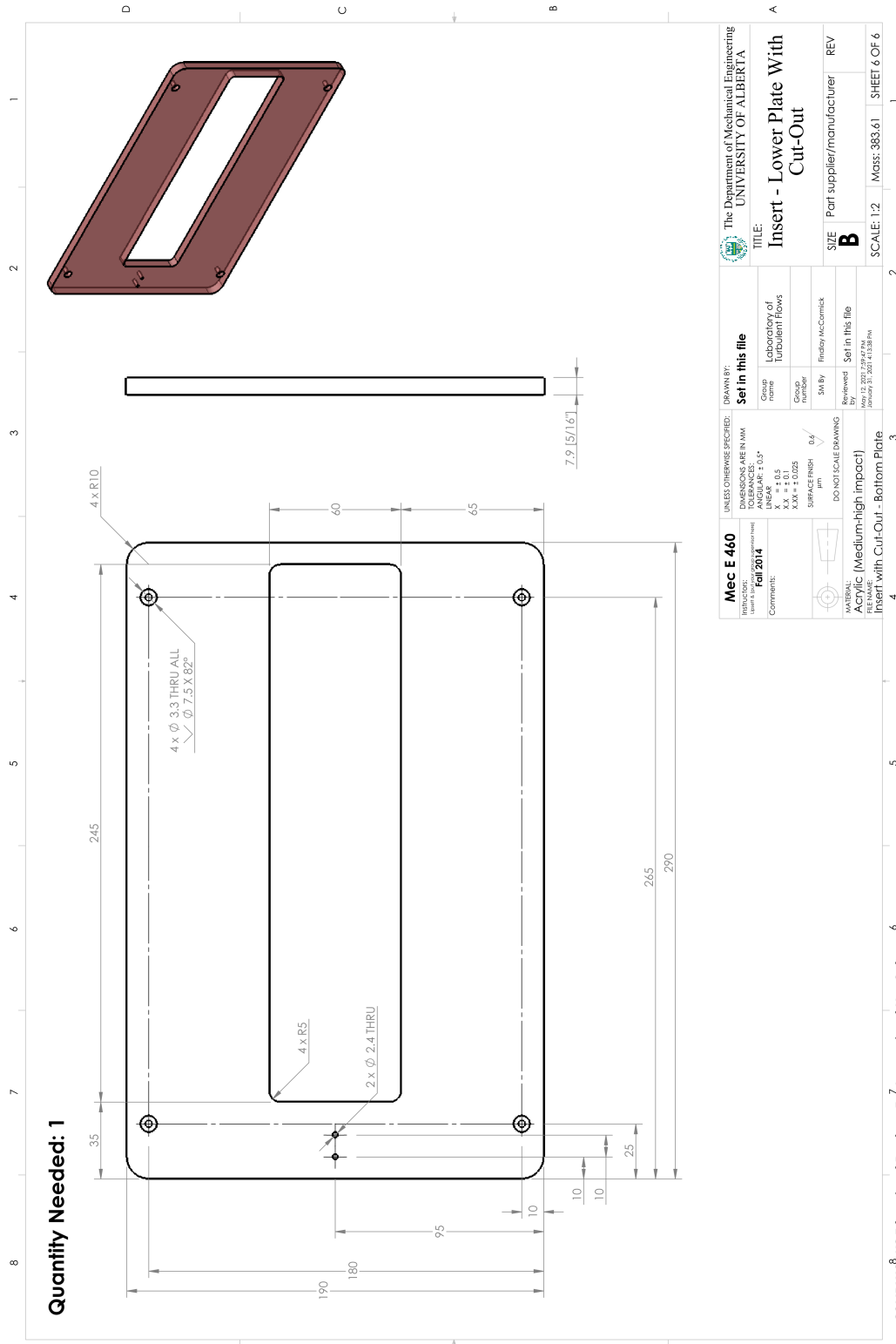
SIZE: **B**  
 Part supplier/manufacturer  
 REV

SCALE: 1:2 Mass: 314.76 SHEET 5 OF 6

The Department of Mechanical Engineering  
 UNIVERSITY OF ALBERTA

TITLE:  
**Insert - Upper Plate With Cut-Out**

SOLIDWORKS Educational Product. For Instructional Use Only.



<b>Mec E 460</b> MFG CODE: <b>Fall 2014</b> Comment:		UNLESS OTHERWISE SPECIFIED: DIMENSIONS ARE IN MM DECIMALS ARE TO 0.15" ANGLES ARE TO 0.5° LINEAR ± 0.3 XX ± 0.3 XXX ± 0.025 SURFACE FINISH: 0.8 μm DO NOT SCALE DRAWING		DRAWN BY: <b>Set in this file</b> Class name: Laboratory of Turbulent Flows Group number: Frisby McComick SW By: Frisby McComick Reviewed: Set in this file Date: 09/20/2017 11:17 AM File Name: MecE460_2017_01_128.rvt	
The Department of Mechanical Engineering UNIVERSITY OF ALBERTA		TITLE: <b>Insert - Lower Plate With Cut-Out</b>		SIZE: Part supplier/manufacturer <b>B</b> SCALE: 1:2 Mass: 383.61 SHEET 6 OF 6	

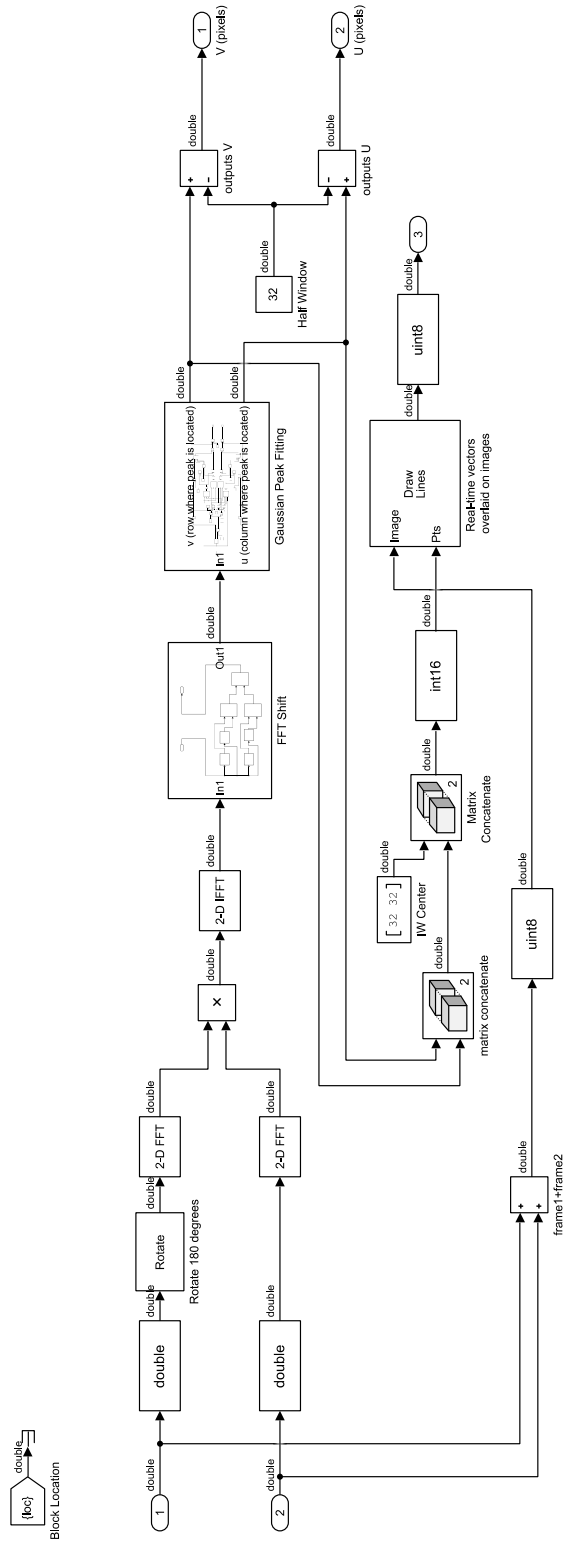
SOLIDWORKS Educational Product. For Instructional Use Only.

## B Simulink Real-time models

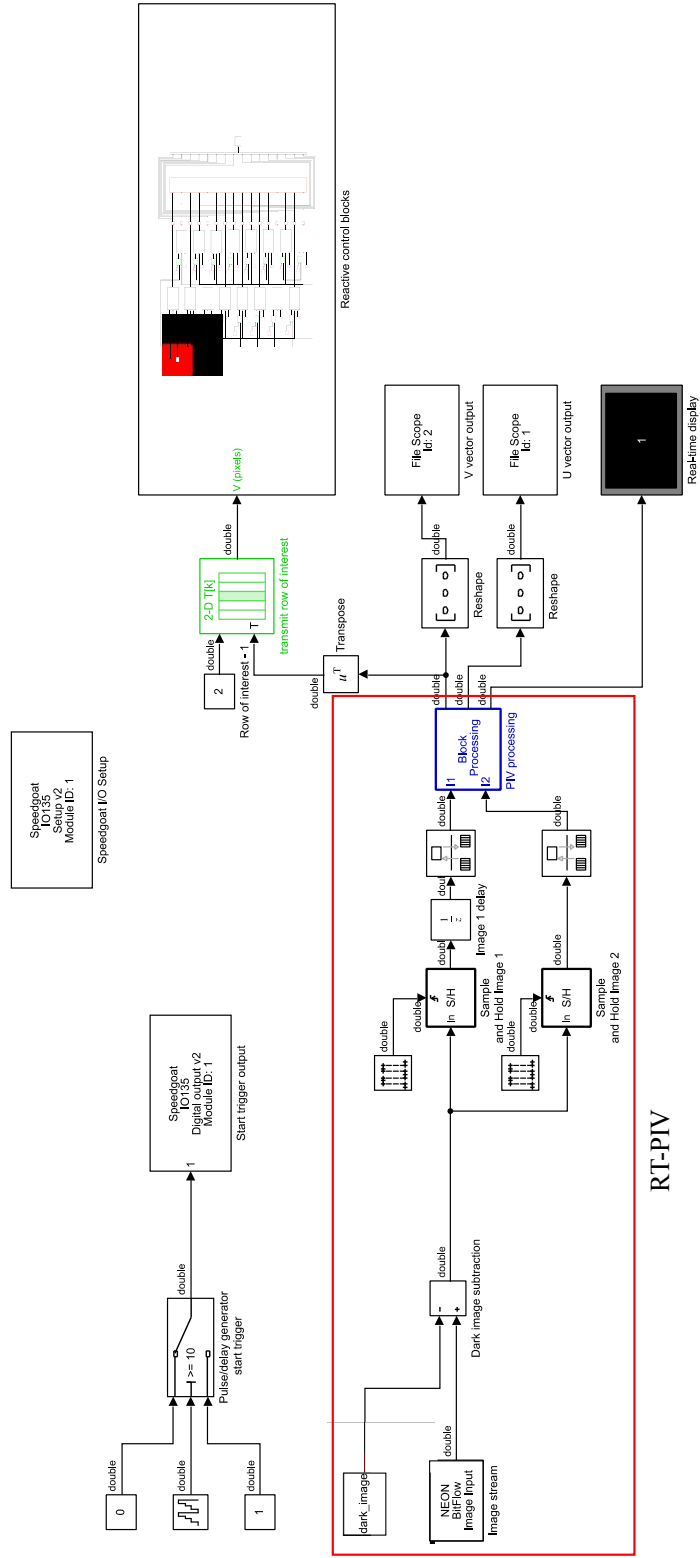
This section contains images of the Simulink Real-time models that were developed for the RT-PIV system, and the implementation of  $v$ - and  $u$ -control.

# Simulink: PIV algorithm

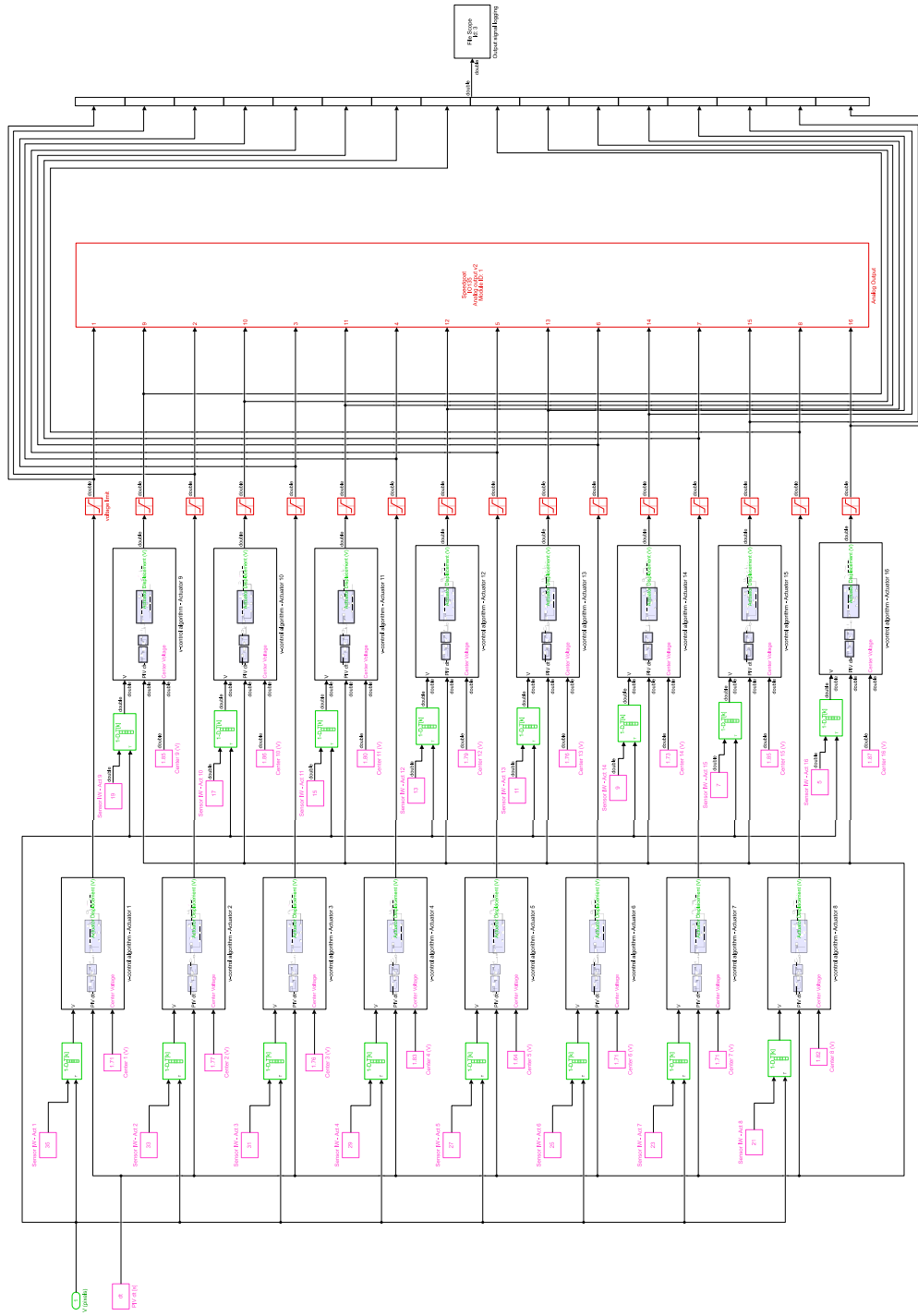
Note: PIV algorithm is contained within a “Block Processing” Simulink block (see next page). The block processing automatically divides input images into interrogation windows and applies the PIV algorithm.



# Simulink: Reactive control model – v-control

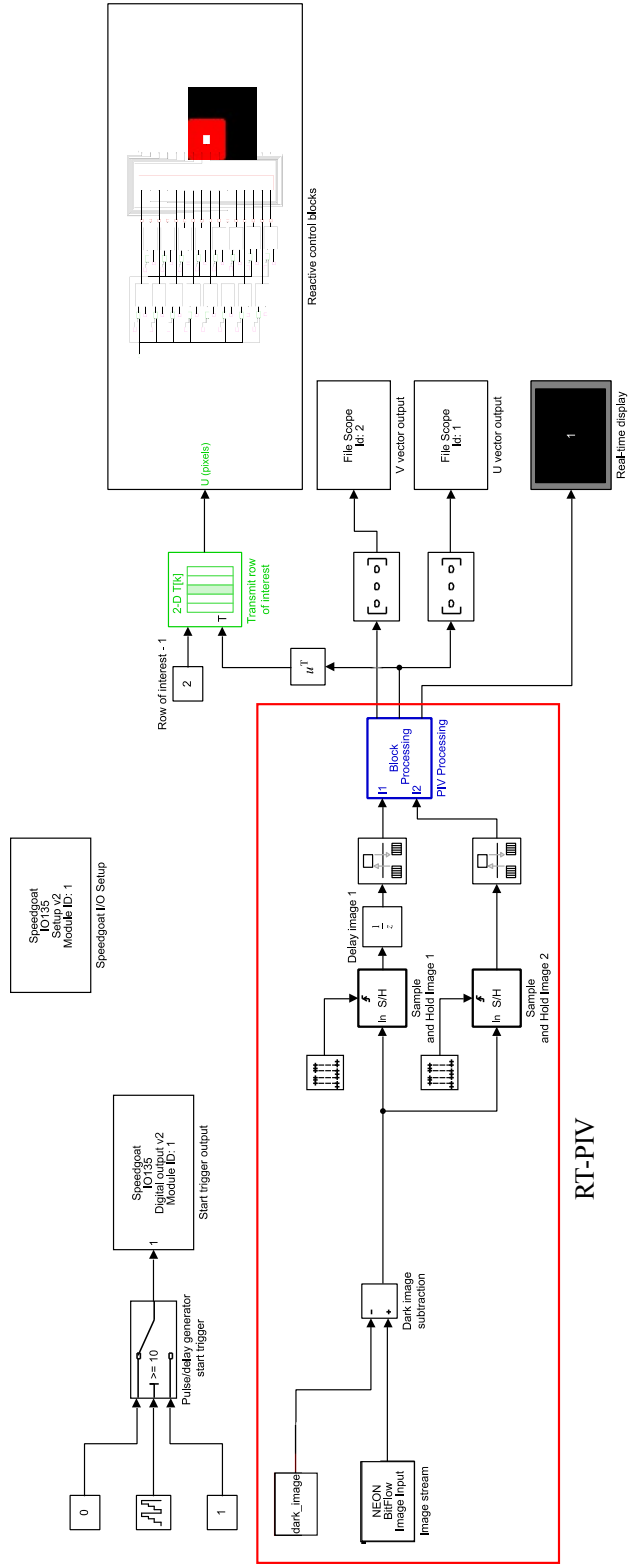


# Simulink: Reactive control blocks for each actuator – $v$ -control

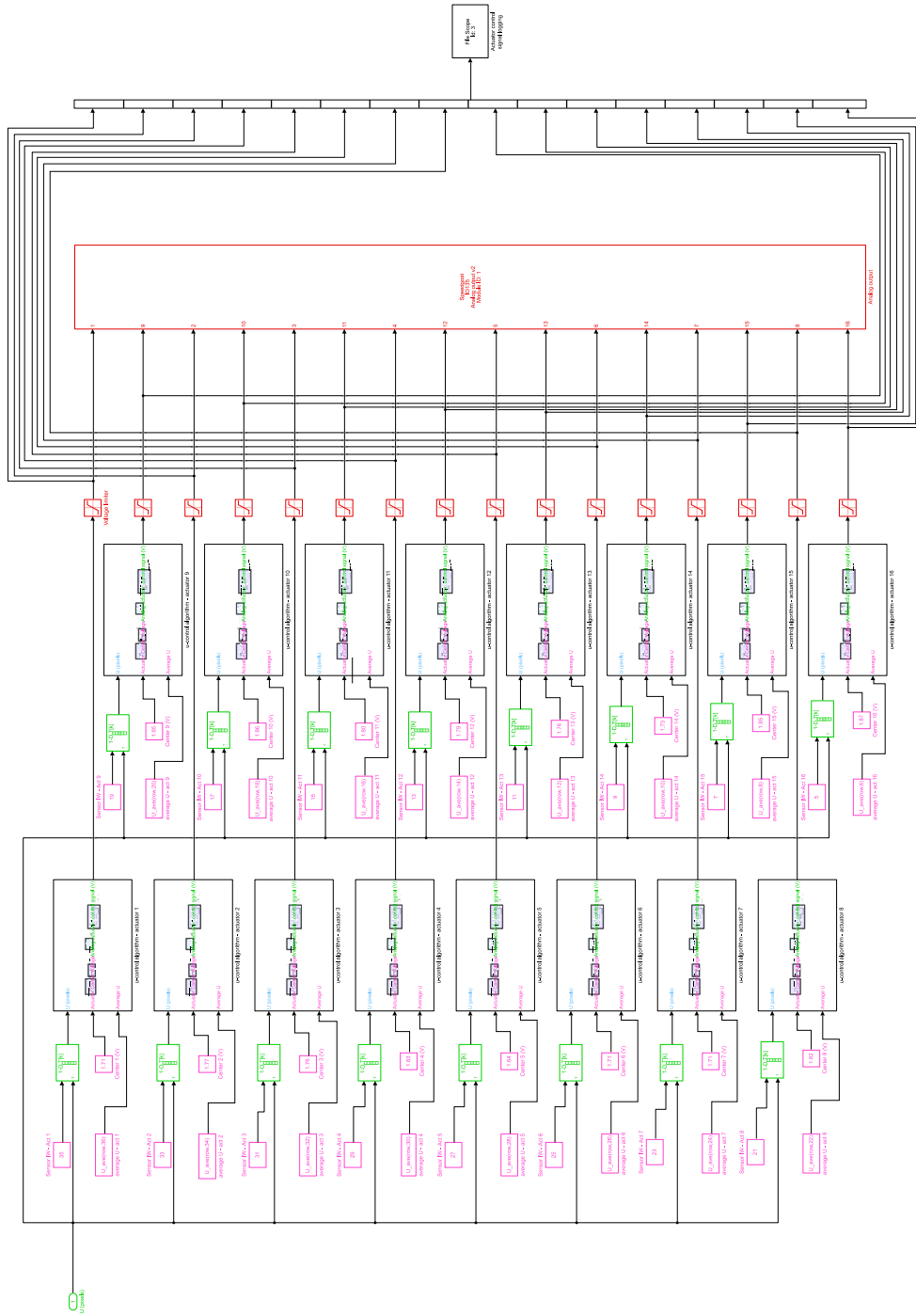




# Simulink: Reactive control model – $u$ -control



# Simulink: Reactive control blocks for each actuator of the active surface – $u$ -control



# Simulink: $u$ -control algorithm

